République Algérienne Démocratique et Populaire

Ministère de l'Enseignement Supérieur et de la Recherche Scientifique

Université Badji Mokhtar
Faculté des Sciences
Département de Physique

Thèse

Présentée en vue de l'obtention du **DOCTORAT**

Domaine : Sciences des Matériaux **Filière :** Physique

Spécialité : Physique de la Matière Condensée et Applications

Laboratoire : Nano-matériaux : Corrosion et Traitement de Surface

Titre

Étude des propriétés physique des matériaux de type pérovskite $A_2B_{1-x}C_xDO_6$.

Réalisé par :

MENDER Sara

Soutenue devant le jury:

Membres	Grade	Établissement	Qualité
BELKHIR Hafid	Prof.	Université Badji Mokhtar	Président
HAKAMY Ahmad	Prof.	Université de Makkah, Arabie Saoudite	Examinateur
Kadri M^{ed} Tahar	Prof.	Université Badji Mokhtar	Examinateur
LEMLIKCHI Safia	MCA.	CDTA-Alger	Examinateur
LABIDI Salima	Prof.	Université Badji Mokhtar	Directrice de thèse
ELLOUZ Mohamed	Prof.	Université de Sfax, Tunisie	Co-directeur de thèse

Année universitaire: 2024-2025

People's Democratic Republic of Algeria

Ministry of Higher Education and Scientific Research

Badji Mokhtar University
Faculty of Sciences
Departement of Physics

Thesis

Submitted for graduation **DOCTORATE**

Field: Material Sciences **Sector:** Physics

Specialty: Condensed Matter Physics and Applications

Laboratory: Nano-materials: Corrosion and Surface Treatment

Title

Study of the physical properties of $Ba_{2-x}Sr_xVRuO_6$ Perovskite-type materials.

Realized by:

MENDER Sara

Defended in front of the jury:

Members	Grade	Institution	Quality
BELKHIR Hafid	Prof.	Badji Mokhtar University	Chair
HAKAMY Ahmad	Prof.	Makkah University, Saudi Arabia	Examiner
Kadri M^{ed} Tahar	Prof.	Badji Mokhtar University	Examiner
LEMLIKCHI Safia	MCA.	CDTA-Alger	Examiner
LABIDI Salima	Prof.	Badji Mokhtar University	Supervisor
ELLOUZ Mohamed	Prof.	University of Sfax, Tunisia	Cosupervisor

Academic Year : 2024-2025

Abstract

We conducted a theoretical study and performed calculations using the Full-Potential Linearized Augmented Plane Wave (FP-LAPW) method based on Density Functional Theory (DFT), as implemented in the WIEN2k code. This work is part of a broader investigation into the structural, electronic, magnetic, elastic, and optical properties of perovskite-type materials ($SrVO_3$, $BaVO_3$, $BaRuO_3$, $SrRuO_3$ Ba_2VRuO_6, Sr_2VRuO_6 and $BaSrVRuO_6$). The exchange-correlation potential was treated using different approximations, namely WC-GGA and TB-mBJ.

We began by examining the magnetic stability of all these compounds. Our results showed that the ferromagnetic (FM) phase is the most stable configuration for all the studied materials. The structural properties, such as lattice parameters, bulk modulus, and its pressure derivative, are in good agreement with available data. The calculation of elastic properties indicates mechanical stability, rigidity, and ductility of these compounds. The three-dimensional representation of Young's modulus reveals a highly anisotropic character.It was also found that the studied materials exhibit half-metallic behavior with interesting energy gaps. Optical properties were studied by determining the complex dielectric function, from which other related parameters were derived.

Keywords: ABX_3, $A_2BB'O_6$, perovskites, half-metallic, DFT, WC-GGA, TB-mBJ, WIEN2k.

Résumé

Nous avons mené une étude théorique et effectué des calculs en utilisant la méthode des ondes planes augmentées linéarisées à potentiel total (FP-LAPW), basée sur la théorie de la fonctionnelle de la densité (DFT), telle qu'implémentée dans le code WIEN2k. Ce travail s'inscrit dans le cadre d'une étude plus large des propriétés structurales, électroniques, magnétiques, élastiques et optiques de matériaux de type pérovskite ($SrVO_3$, $BaVO_3$, $BaRuO_3$, $SrRuO_3$, Ba_2VRuO_6, Sr_2VRuO_6 et $BaSrVRuO_6$). Le potentiel d'échange-corrélation a été traité en utilisant différentes approximations, notamment WC-GGA et TB-mBJ.

Nous avons commencé par examiner la stabilité magnétique de tous ces composés. Nos résultats ont montré que la phase ferromagnétique (FM) est la configuration la plus stable pour tous les matériaux étudiés. Les propriétés structurales, telles que les paramètres de maille, le module de compressibilité et sa dérivée par rapport à la pression, sont en bon accord avec les données disponibles. Le calcul des propriétés élastiques indique une stabilité mécanique, une rigidité et une ductilité de ces composés. La représentation tridimensionnelle du module de Young révèle un caractère fortement anisotrope. Il a également été démontré que les matériaux étudiés présentent un comportement demi-métallique avec des gaps énergétiques intéressants. Les propriétés optiques ont été étudiées à partir de la fonction diélectrique complexe, à partir de laquelle d'autres paramètres ont été dérivés.

Mots-clés : ABX_3, $A_2BB'O_6$, pérovskites, demi-métallique, DFT, WC-GGA, TB-mBJ, WIEN2k.

الملخص

أجرينا دراسة نظرية وقمنا بحسابات باستخدام طريقة الموجات المستوية المعززة بالكامل (FP-LAPW) المستندة إلى نظرية الكثافة الوظيفية(DFT) ، كما هي مُطبقة في كود .WIEN2k يندرج هذا العمل ضمن إطار دراسة أوسع للخصائص البنيوية والإلكترونية والمغناطيسية والميكانيكية والبصرية لمواد من نوع البيروفسكايت، وهي $(SrVO_3, BaVO_3, BaRuO_3,$ $SrRuO_3, Ba_2VRuO_6, Sr_2VRuO_6$ و$BaSrVRuO_6$). تم التعامل مع الجهد التبادلي-الارتباطي باستخدام تقريبات مختلفة، وهي WC-GGA و.TB-mBJ

بدأنا بدراسة الاستقرار المغناطيسي لجميع هذه المركّبات. وقد أظهرت النتائج أن الطور الفيرومغناطيسي (FM) هو الأكثر استقرارًا لكل المواد المدروسة. الخصائص البنيوية، مثل ثوابت الشبكة، معامل الانضغاط ومشتقّه بالنسبة للضغط، كانت متوافقة بشكل جيد مع البيانات المتوفرة. تشير حسابات الخصائص الميكانيكية إلى الاستقرار الميكانيكي، والصلابة، والقابلية للتطريق لهذه المركّبات. كما أظهرت التمثيلات الثلاثية الأبعاد لمعامل يونغ طابعًا عاليًا من التباين الاتجاهي .وقد تبين أيضًا أن المواد المدروسة تُظهر سلوكًا شبه فلزي (half-metallic) مع فجوات طاقية مثيرة للاهتمام. كما تمّت دراسة الخصائص البصرية من خلال تحديد الدالة العازلة المعقدة، والتي تم اشتقاق باقي المعلمات المتعلقة منها.

الكلمات المفتاحية: ABX_3 ، $A_2BB'O_6$، بيروفسكايت، نصف معدن، نظرية دالية الكثافة .

Dedication

With the help of **ALLAH**, this work is now complete.

To the ones who lit my path, paved the way, and eased every hardship,

to those who grew more weary than I did, whose prayers at every prostration are the reason I stand here today, to the two who have long dreamed of this moment, the beat of my heart, my mother **Halima** and my father **Hocine** thank you for everything. I can never repay you in my lifetime. May God preserve you for me always.

To the one who opened doors for me and supported me throughout the journey,

my sister **Wafa**, I am deeply grateful to you.

To my soul **Mohamed** and **Abd El Mouiz,** Thank you for standing by me.

To my aunt and second mother, **Saliha**, With all my love and gratitude for your constant care and support.

To my brothers and sisters ‘‘**Nawel, Mofida, Saliha, Houria, Hannen, Khaled, Abdelhaq, Adel** and **Kais** ’’ who have shared my joys and sorrows and have always believed in me, your presence has been a steadfast pillar in my life.

To my nieces and nephews ‘‘**Abd El Rahmen, Abd El Raouf, Louay, Anas, Arig, Maria, Meriem** and **Layan**’’, you are the light of my life.

To my friends, who are the shining stars in the sky of my life, your presence lights up my days and warms my heart. Thank you for your priceless friendship and unwavering support.

It is thanks to all of you that I was able to realize this dream and reach this important milestone in my life. I am endlessly grateful for your love, your support, and your trust.

Sara MENDER

ACKNOWLEDGMENTS

First and foremost, I thank ALLAH, who granted me the will and patience to complete this work

I would also like to express my profound gratitude to my thesis supervisor, Professor **LABIDI Salima** of Badji Mokhtar University–Annaba, and Cosupervisor Professor **ELLOUZ Mohamed** of The University of Sfax, Tunisia, for their unwavering support and the trust she placed in me. Their constant encouragement, steadfast guidance through the broad realms of scientific research, and the substantial assistance they provided during this study have been essential to my academic development.

I would also like to express my deep gratitude to Professor **BELKHIR Hafid** of Badji Mokhtar University – Annaba for the honor he did me by agreeing to chair my defense committee.

My thanks go to Professor **HAKAMY Ahmad** of Makkah University, Saudi Arabia, for kindly assessing my work as an examiner; I greatly appreciate the honor of her participation on the committee.

I would like to thank Professor **Kadri M^{ed} Tahar** of Badji Mokhtar University – Annaba, for honoring me with her presence on my thesis committee as an examiner.

My gratitude also goes to Dr. **LEMLIKCHI Safia** of CDTA-Alger, for the honor of serving on my thesis committee as an examiner.

I further wish to express my profound appreciation and high regard to **Mr. Abderrahmane Cheriet** and **Imane Koriba** for their help, guidance, and constant encouragement.

Finally, I thank everyone who, directly or indirectly, contributed to bringing this work to completion, and I wish strength and continued success to all who are finishing or beginning their own theses.

Sara MENDER

Table of Contents

Chapter II : Overview of calculation methods

Chapter III : The simple perovskite ABO_3 (A=Sr, Ba and B=V, Ru)

Chapter IV : The double perovskite $Ba_{2-x}Sr_xVRuO_6$

NOMENCLATURE USED

Symbol / Abbreviation	Meaning
t	Tolerance factor.
μ	Octahedral factor.
DFT	Density-Functional Theory.
E_{xc}	Exchange–correlation energy.
R_{MT}	Muffin-Tin sphere radius.
LDA	Local-Density Approximation.
LSDA	Local Spin-Density Approximation.
GGA	Generalized-Gradient Approximation.
mBJ	Modified Becke-Johnson.
APW	Augmented Plane Wave.
FP-LAPW	Full-Potential Linearized Augmented Plane Wave.
SCF	Self-Consistent Field cycle.
BZ	Brillouin zone.
E_F	Fermi energy.
B	Bulk modulus (compressibility).
Up/Dn	Spin Up / Spin Down.
FM	Ferromagnetic.
μ_{tot}	Total magnetic moment.
DOS	Density of States.
TDOS/PDOS	Total Density of States / Partial Density of States
EOS	Equation of State.
BV	Valence band.
BC	Conduction band.

List of Figures

Chapter I : General information on the structures and properties of Perovskites

Chapter II : Overview of calculation methods

Chapter III : The simple perovskite ABO_3 (A=Sr, Ba and B=V, Ru)

Chapter IV : The double perovskite $Ba_{2-x}Sr_xVRuO_6$

List of Tables

Chapitre I : General information on the structures and properties of Perovskites

Chapter III : The simple perovskite ABO_3 (A=Sr, Ba and B=V, Ru)

Chapter IV : The double perovskite $Ba_{2-x}Sr_xVRuO_6$

General introduction

General introduction

This last century has been marked by scientific and technological development, such as HD television, mobile telephony, high-speed internet, and other applications in modern industry such as photovoltaics, renewable energy (solar panels, etc.), nanoscience, nanotechnology, etc. and other fields of sensors and electronics, which have increased the need for heat storage and the capacity to transfer information. It then becomes essential to use electromechanical and electronic devices. For this, it is necessary to know the characterization of materials, which are the basis of any technological development, and which will be the hallmark of any electronic device used in modern and technological industry.

Understanding how materials behave, and why they differ in properties, was only possible with atomistic understanding through quantum mechanics, which first explained atoms and then solids. The combination of physics, chemistry, and the emphasis on the relationship between a material's properties and its microstructure is the field of materials science. The development of this science has made it possible to design materials and has provided a knowledge base for multiple applications.

Currently, it is possible to describe materials by theoretical models that can explain experimental observations, and especially to perform modeling or "virtual experiments" that can predict the behavior of materials where real experience is lacking, or is very expensive and sometimes difficult to achieve.

The methods for calculating the different properties developed over the last decades are numerous, and in particular, ab-initio methods have become today a basic tool for calculating the structural, electronic, magnetic and elastic properties of complex systems. They are also a tool of choice for predicting new materials.

Among the ab-initio methods, the linearized augmented plane wave (FP LAPW) method is one of the best known and most accurate currently for calculating the electronic structure of solids within the framework of density functional theory (DFT). The equations underlying this theory were established by Pierre Hohenberg [1], Walter Kohn and Lu Sham [2] in the 1960s. These equations are at the origin of most of the electronic structure calculation codes used to study crystalline materials. Their resolution gives access to the total energy of the crystal, the density of states, as well as the magnetic moment of the different atoms. It has remained by far

the most used and the most efficient for several years. Its advantage lies in the fact that it can process a large number of atoms [2,3].

In recent years, perovskite materials have gained enormous interest and become one of the most motivating topics in the field of research, particularly attracting the interest of chemists and solid-state physicists due to their interesting properties such as superconductivity [4,5], ferroelectricity, semiconductivity, ionic conduction characteristics, piezoelectricity, thermoelectricity, ferromagnetism [6-8], semimetallic transport and colossal magnetoresistance [9,10].These properties are sensitive to temperature, pressure and phase changes.

Perovskites find wide application in modern electronics due to their interesting properties, these properties lend themselves to many technological applications including optical waveguides, high-temperature oxygen sensors, dynamic random access memories, frequency doublers [11,12].

Transition metal oxides, and particularly oxide-based perovskites, are materials whose strongly correlated electrons in the 3d layers give rise to a very rich phase diagram, and whose properties such as colossal magnetoresistance, ferroelectricity, magnetism and superconductivity are sensitive to the structural distortion and chemical composition of the crystals.

Among these complex oxides, we are particularly interested in perovskite materials based on the atom Strontium $SrXO_3$ and Barium $BaXO_3$, where the X sites are occupied by transition metals, is a family of materials widely studied by researchers for their high chemical stability and good electrical resistance, high temperature properties , The ideal double perovskite also shows cubic symmetry for a tolerance factor ($t \approx 1$) with a space group (Fm-3m), and the lattice parameter is twice that of the simple cubic aristo-type ABX_3, which is studied by Lavat and Baran [13,14]. What interests us in this work are the compounds of the double perovskite family with the formula X_2VRuO_6 (X=Ba,Sr), the presence of Vanadium V and Ruthenium Ru atoms in position B' and B should give rise to much more opportunity and richness of electronic and optical properties.

This study focuses on the study of structural, electronic, elastic, optical and magnetic properties of the compounds $SrRuO_3$, $SrVO_3$, $BaRuO_3$, $BaVO_3$, Sr_2VRuO_6, Ba_2VRuO_6 and

$BaSrVRuO_6$. Using density functional theory based on the FP-LAPW method implemented in the Wien2k code [3-15].

This manuscript is structured around three main chapters, ordered as follows:

- The first chapter will deal with generalities on the perovskite structure, and their derived structures, as well as the stability conditions, classification of perovskites, and physicochemical properties and technological applications of the latter.
- The second chapter presents all the theoretical concepts necessary for understanding the calculation method used, namely density functional theory (DFT).
- The third chapter is devoted to the presentation of the results of the simple perovskite ABO3 (A=Sr, Ba and B=V, Ru) and their interpretations by comparing them with previous theoretical and experimental studies.
- The fourth chapter presenting the results for the double perovskite $Ba_{2-x}Sr_xVRuO_6$ (x=0, 1 and 2) and their interpretations through comparison with earlier theoretical and experimental research.

Finally, we end with a general conclusion that brings together all the main results of this work.

References

[1] P. Hohenberg and W. Kohn, Physical review, 136(3B), p. B864, 1964.

[2] W. Kohn and L. Sham, Physical review, 140(4A), p. A1133, 1965.

[3] P. Blaha, K. Schwarz, G.K.H. Madsen, D. Kvasnicka, J. Luitz, Wien2k, T.U. Wien, Editor.Vienna, (2001).

[4] T. He et al., Nature, 411(6833),pp. 54-56, 2001.

[5] K. Nelson, Z. Mao, Y. Maeno, and Y. Liu, Science, 306(5699), pp. 1151-1154, 2004.

[6] H. Fu and R. E. Cohen, Nature, 403(6767), pp. 281-283, 2000.

[7] E. Bousquet et al., In APS March Meeting Abstracts (pp. U38-009), pp. 732-736, 2008.

[8] Y. Yamasaki et al., Physical review letters, 101(9), p. 097204, 2008.

[9] C. Koonce, M. L. Cohen, J. Schooley, W. Hosler, and E. Pfeiffer, Physical Review, 163(2), p. 380, 1967.

[10] C. Solís, M. Rossell, G. Garcia, A. Figueras, G. Van Tendeloo, and J. Santiso, Solid State Ionics, 179(35-36), pp. 1996-1999, 2008.

[11] V. Henrich and P. Cox, "The Surface Science of Metal Oxides Cambridge Univ," 1994.

[12] E. Mete, R. Shaltaf, and Ş. Ellialtıoğlu, Physical Review B, 68(3), p. 035119, 2003.

[13] V. M. Goldschmidt, Geochemistry,ed. 2. Oxford Univ. Press, Oxford (1958).

[14] Lavat, A. E. Baran, E. J. Vibrat.32(2).167-174. (2003).

[15] J.P. Perdew and A. Zunger, Phys. Rev. B 23, 5048, (1981)

Chapter I :

General information on the structures and properties of Perovskites

I–1 Intrudction

Perovskites are a diverse group of materials distinguished by their unique crystal structure, characterized by the general formula ABX_3. In this structure, 'A' and 'B' are cations of different sizes (where the A atom is most often an alkaline, alkaline earth or rare earth, the B atom is a 3d, 4d or 5d transition metal), while 'X' is an anion that bonds to both (This anion can be oxide, fluoride and in other cases, chloride, bromide, iodide, sulfide or hydride). Typically, the structure consists of a framework of corner-sharing BX_6 octahedra, with the 'A' cations occupying the cavities between these octahedra.

The versatility of perovskite materials stems from their ability to incorporate a wide range of different elements in the 'A' and 'B' sites, as well as various anions in the 'X' site. This compositional flexibility results in a broad array of material properties that can be tailored for specific applications. Perovskites can exhibit a wide range of physical properties, including superconductivity, ferroelectricity, high ionic conductivity, and exceptional optoelectronic properties. These characteristics make them suitable for various applications, such as photodetectors, lasers, solar cells and light-emitting diodes.

In this chapter, we will begin with an overview of perovskites, discussing their history and classification, including single and double perovskites, and those based on oxides or halides. We will then describe their corresponding structures. Finally, we will provide a general description of the magnetic properties of perovskite oxides.

I-2 Ideal structure of the perovskite

The unit cell of an ideal perovskite is cubic in the symmetry group $Pm\bar{3}m$ (#221), with a cell parameter of the order of 3.9 Å (7.37 Bohr) in which :

- The A cations occupy the vertices of the cubes and are surrounded by 12 anions in a cubo-octahedral coordination.
- The B cations occupy the centers of the cubes and are surrounded by 6 anions in a octahedral coordination.
- The X anions occupy the center of each face of the cubes and are surrounded by 2 B cations and 4 A cations **[1]** .

We can also obtain the same lattice by a repetition of the cubic structure where the cations A occupy the center of the cube, the cations B the vertices and the anions X the middle of the edges of the cube (figure II.1). In the rest of this manuscript, X will correspond to oxygen.

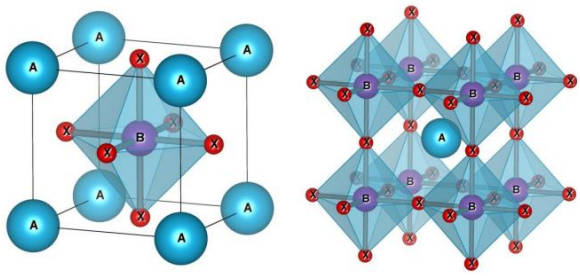

Figure I-1: Two different ways of representing the cubic ABX_3 perovskite structure a) atom B at the origin (BX_6 octahedrons represented), b) atom A at the origin of the cell.

I–3 The different types of perovskite structure

We can distinguish two types of perovskites depending on the occupation of sites A and B:

- **Simple perovskites**: These have sites A and B occupied by a single type of cation, such as $NaTaO_3$, $SrZrO_3$, $CaTiO_3$ and $BaTiO_3$ [2,3]
- **Complex perovskites**: In these, one of the sites (A or B) is occupied by two distinct cations with different valences. Their formula can be

schematized as $A(B'_xB''_{y)})O_3$ (e.g., $PbMg_{1/3}Nb_{2/3}O_3$) or $(A'_xA''_y)BO_3$ (e.g., $Na_{1/2}Bi_{1/2}TiO_3$), where x + y = 1**[4].**

- **Superstructures**: Both sites A and B are simultaneously occupied by different types of cations (e.g., (PbLa)(ZrTi)O_3, $La_{0.8}Sr_{0.2}Ga_{0.8}Mg_{0.15}Co_{0.05}O_{2.8}$) **[5]** .
- **Double perovskites**: Named because the unit cell volume is twice that of a simple perovskite (e.g., Sr_2FeMoO_6, $NdBaCo_2O_6$).

Double perovskites have two subfamilies: one with compounds ordered on-site A as $AA'B_2O_6$ and the other on-site B as $A_2BB'O_6$. In the latter, two transition metals B and B' are surrounded by oxide anions, forming octahedra BO_6 and $B'O_6$, which are connected at the corners (Figure I.2). Depending on how these octahedra are arranged in the crystal, we observe three situations: random arrangement, alternating layers of $BO_6/B'O_6/BO_6$, and a three-dimensional pattern where each BO_6 octahedron only neighbors $B'O_6$ octahedra and vice versa **[6]**.

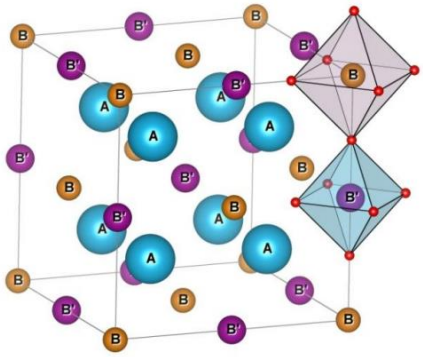

Figure I-2: lattice of the double perovskite ordered on site B ($A_2BB'O_6$). A cations are located in the center of each cell.

I-4 Stability of the perovskite structure

Many factors control the stability of the perovskite structure; among them, the choice of atoms positioned on the sites of cations A and B is primordial and

essential in the stability of these compounds, particularly the relationship linking the lengths of the ionic radii of cations A and B and the anion X by the iconicity of the bonds, as well as the difference in electronegativity between the cations and anions, which plays a decisive role in determining the properties of these materials.

I-4-1 Tolerance factor

In 1927, V. Goldschmidt introduced the tolerance factor **[7]** , denoted as "t" or the Goldschmidt factor, as a dimensional criterion. This factor helps gauge the stability of the perovskite structure based on the ionic radii of its constituent atoms. Imagine these ions as rigid spheres. In an ideal perovskite structure, we can relate the length of a mesh edge to the ionic radii of the atoms B and X. Specifically, we focus on an isosceles right triangle marked with thick lines in Figure I.4. Here, the length of one side equals the sum of the radii of atoms B and X (r_B+r_X), while the length of the hypotenuse equals the sum of the radii of atoms A and X (r_A+r_X). The tolerance factor t mathematically expresses this relationship **[8].**

$$t = \frac{r_A+r_O}{\sqrt{2}(r_B+r_O)} \qquad \text{(I-1)}$$

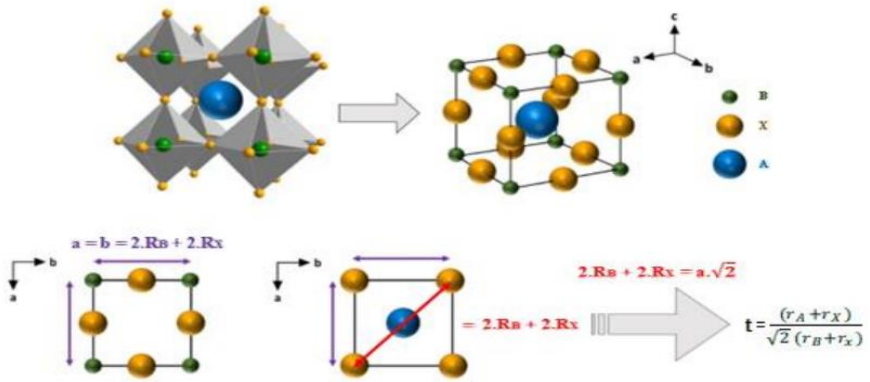

Figure I-3: Representations of the cubic unit ABX_3 explaining the trigonometric relationship of the ionic radii and leading to the Goldschmidt tolerance factor.

According to this criterion, when the tolerance factor "t" is very close to 1, we observe a cubic structure. The stability limits of the perovskite phase, whether more or less distorted, are defined by "t" values ranging between 0.75 and 1.06. Therefore, any deviation of "t" from its ideal value indicates a distortion of the cubic structure. Various structures can be distinguished based on the value of the tolerance factor, as grouped in the table below:

Table I-1: The evolution of crystal structures as a function of the tolerance factor **[9,10]**

T < 0.75 Ilmenite	
0.75 < t < 1.06 Perovskite	**0.75 < t < 0.95** Orthorhombic distortion
	0.96 < t < 0.99 Rhombohedral distortion
	0.99 < t < 1.06 Cubic distortion
T > 1.06 Hexagonal	

I-4-2 The octahedral factor

Another factor, known as the octahedral factor (μ), can be defined as the ratio of the ionic radii of B and X. This factor helps assess the stability of the BX_6 octahedron. For the octahedron to maintain its stability, the octahedral factor must fall within the range of 0.414 to 0.738 **[11].** Mathematically, this factor is expressed as **[12].**

$$\mu = \frac{r_B}{r_X} \qquad \text{(I-2)}$$

I-4-3 VA/VB ratio

Furthermore, to assess the stability of this ideal structure, we can consider the ratio of the volume of the polyhedron containing cation A (V_A) to that of cation B (V_B), which ideally equals 5 **[13].** This V_A/V_B ratio serves as a useful metric for characterizing the degree of distortion in the perovskite structure. A smaller ratio indicates a greater structural distortion. For instance, consider the case of $SrTiO_3$,

whose structure closely approximates the ideal structure, with lattice parameter (a_p) = 3.905 Å, t= 1.002, and V_A/V_B = 4.9998 **[14].**

I-4-4 Iconicity of anion-cation bonds

The difference in average electronegativity between the different ions in an ABO3 perovskite material influences the stability of its structure. This difference is defined by the following relationship:

$$\bar{\chi} = \frac{\chi_{A-O} + \chi_{B-O}}{2} \qquad \text{(I-3)}$$

where χ_{A-O} and χ_{B-O} are the differences in electronegativity between the cations at sites A and B and the associated oxygens, respectively.

The ideal perovskite structure has a pronounced ionic character. Covalent lead-based perovskites are less stable than more ionic perovskites like $BaTiO_3$ **[15,16].**

I-4-5 Electro neutrality

Naturally, the overall ionic structure must be electrically neutral. The sum of the oxidation numbers of the (cations and anion) must be zero. If the charges on the ions are written as Q_A, Q_B and Q_X, then:

$$Q_A, + Q_B = 3Q_X \qquad \text{(I-4)}$$

For simple ABO_3 oxide systems, classifications can be established based on the cationic valences, as follows:

$$[1 + 5] = A^{I}B^{V}O_3$$

$$[2 + 4] = A^{II}B^{IV}O_3$$

$$[3 + 3] = A^{III}B^{III}O_3$$

I-4-6 Coordination as a function of ionic radius

The ABX_3 perovskite structure has the potential to accommodate an extensive number of elements at the A and B sites, with A^{m+} representing a cation from the alkaline earth metal or transition metal groups, while B^{n+} denotes a cation from the transition metal or rare earth categories. To form a more stable perovskite structure, the (A^{m+}, B^{n+}) pair must satisfy a number of conditions; the cation (A^{m+}) is placed in the octahedral cube cavity with an ionic radius that must be greater than 0.9 Å, for a coordination of 12. The cation (B^{n+}) of smaller size than (A^{m+}) is placed at the top of a cube with an ionic radius greater than 0.51 Å to be able to keep the coordination 6. **[17]**

I-5 Class of Perovskites

I-5-1 Orthorhombic Perovskite

The $GdFeO_3$ structure is a prime example of distorted orthorhombic perovskites. Its space group is Pbnm, with lattice parameters: a = 5.346 Å, b = 5.616 Å, and c = 7.666 Å. In this structure, the FeO_6 octahedra are distorted and tilted **[18].** and the GdO_{12} polyhedron is also significantly distorted. This structure is depicted in Figure I.1. Notable compounds that crystallize in this structure include $NaUO_3$, $LaYbO_3$,$NaMgF_3$, and many lanthanide compounds such as $LnFeO_3$,$LnCrO_3$, $LnMnO_3$, $LnRhO_3$, and $LnGaO_3$ **.[19]**

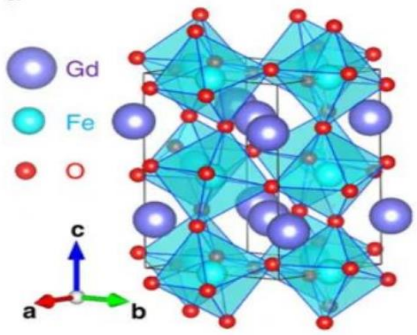

Figure I-4: Unit cell of an orthorhombic perovskite.**[20]**

Table I-2: Atomic positions of an orthorhombic perovskite **[20].**

Site	Cation A	Cation B	Anion O(1)	Anion O(2)
Local	4c	4b	4c	8d
Coordinates	(0, 1/4, z)	(0, 0, 1/2)	(0, 1/4, z)	(1/4, y, 1/4)

I-5-2 Rhombohedral Perovskite

Rhombohedral perovskites represent another possible distortion of the perovskite structure. This structure is characterized by three parameters of equal length (a = b = c) and three equal angles (α, β, γ) that differ from 90°. Examples of rhombohedral perovskites include $LaNiO_3$, $PrAlO_3$, $LaCoO_3$, and $LaAlO_3$.

$LaCoO_3$, for instance, has a rhombohedral structure at room temperature with lattice parameter a = 5.3416 Å and angle α = 60.99° **[21].** It undergoes two notable phase transitions at high temperatures **[22]**. The space group for this structure is c3R (number 167), and each unit cell contains two formula units (Z=2) of ABO_3. This structure is illustrated in Figure I-6.

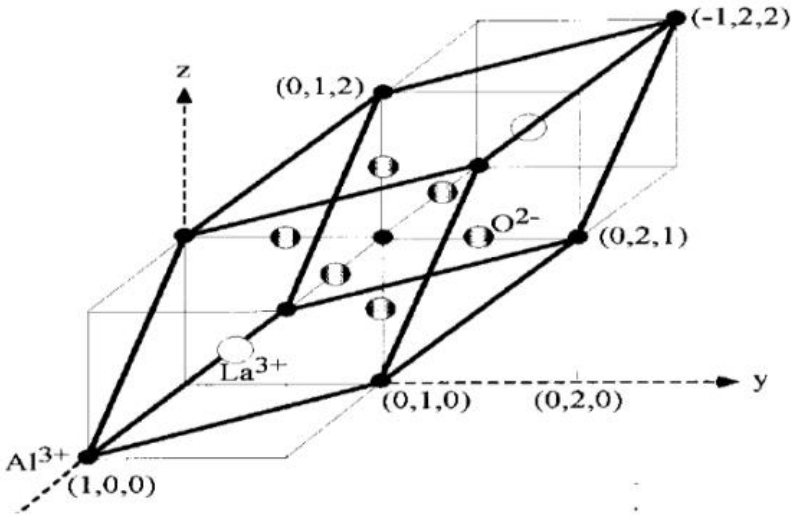

Figure I-5: Unit cell of a rhombohedral perovskite of $LaAlO_3$ (R-c-167) **[23]**

Table I.3: Atomic positions of a rhombohedral perovskite (R3c-167) **[21].**

Site	Cation A	Cation B	Anion O
Local	2c	2b	6e
Coordinates	(1/4, 1/4, 1/4)	(0, 0, O)	(x, y, 3/4)

I-5-3 Tetragonal Perovskite

The ferroelectric form of $BaTiO_3$ at room temperature serves as a well-known example of a tetragonal perovskite. The lattice parameters for this structure are a = 3.994 Å and c = 4.038 Å, with angles $\alpha = \beta = \gamma = 90°$ **[24].**

In this configuration, Ba ions occupy the eight vertices of the cube, Ti ions are positioned 0.201 Å above the center of the octahedron body along the C4 axis, and O ions are located at the center of the cube, forming an octahedron (TiO_6) **[24].**

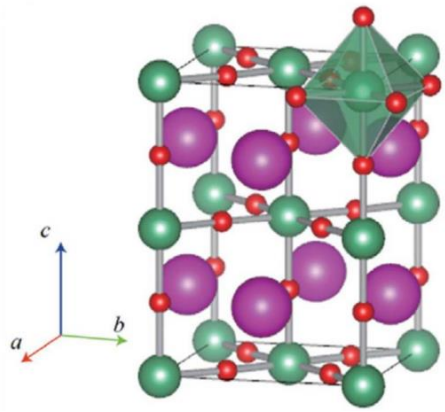

Figure I-6: Unit cell of a tetragonal perovskite (I4/mcm-140) **[20].**

Table I-4: Atomic positions of the tetragonal perovskite $BaTiO_3$ (P4mm-51) **[25].**

Site /atom	Ba	Ti	O	O
Coordinates	(0, 0, 0.01)	(1/2, 1/2, 0.527)	(1/2, 1/2, -0.023)	(1/2, 0, 1/2)

I-5-4 Hexagonal Perovskite

Hexagonal perovskites, although sometimes referred to as perovskites, are actually better considered as intermediate structures due to their significant lattice distortions and departure from the typical perovskite symmetry. These materials exhibit a hexagonal deformed structure with the space group P/63cm, characterized by lattice parameters ($a=b\neq c$ and angles $\alpha = \beta = 90°$, $\gamma = 120°$).

A well-known example of a hexagonal perovskite is $YMnO_3$, which belongs to the space group P63/mmc and has lattice parameters a=3.518 Å and c=11.29 Å **[26]**.

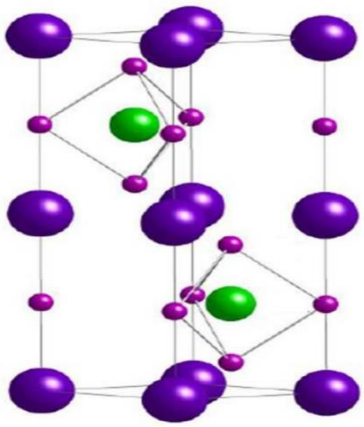

Figure I-7: Unit cell of a hexagonal perovskite (P63/mmc)

Table I-5: Atomic positions in the hexagonal perovskite (P63/mmc) **[26]**.

Site	Local	Coordinates
Cation A(1)	2a	(0, 0, 0)
Cation A(2)	2a	(0, 0, 1/2)
Cation B(1)	2c	(1/3, 2/3, 1/4)
Cation B(2)	2c	(2/3, 1/3, 3/4)
Anion O(1)	2b	(0, 0, 1/4)
Anion O(2)	2b	(0, 0, 3/4)
Anion O(3)	4f	(1/3, 2/3, z)
Anion O(4)	4f	(2/3, 1/3, z)

I-5-5 Monoclinic and Triclinic Perovskite

Monoclinic (e.g., $BiMnO_3$, $BiScO_3$) or triclinic (e.g., $CsPbI_3$,$AgCuF_3$, $BiCrO_3$,$PbSnO_3$) unit cells have been observed in several cases. However, these unit cells are often pseudo cells of a real multiple cell structure. For example, $GdFeO_3$-type phases have frequently been classified based on a pseudo-monoclinic lattice with a ~ b ~ a′ and $\beta \sim 90^{o}$ **[27].**

I-5-6 Polymorphism

Many perovskite-type materials exhibit several polymorphic modifications, which are significant due to their impact on physical properties and applications. For instance, the compound $BaTiO_3$ undergoes multiple temperature-sensitive crystallographic changes, transitioning successively through rhombohedral, orthorhombic, tetragonal, cubic, and hexagonal phases **[28].**

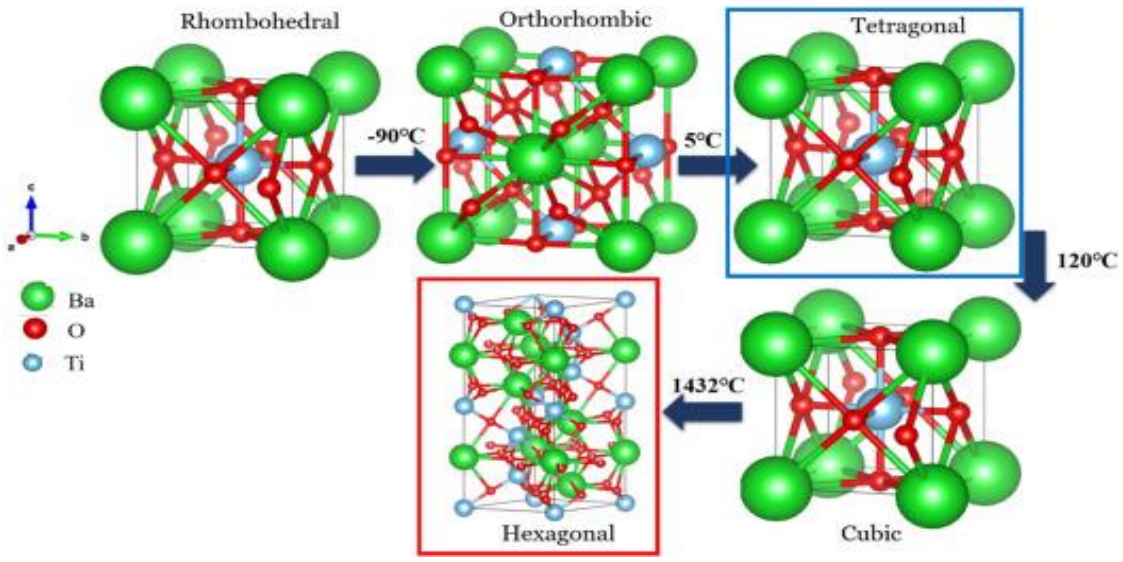

Figure I-8 : Crystallographic Changes of the Oxide $BaTiO_3$

These phase changes in BaTiO3 are reversible, and all polymorphic forms have a pseudo-cubic unit cell with $a' \sim 4$ Å. It is important to note that the rhombohedral, orthorhombic, and tetragonal forms are all ferroelectric at lower temperatures.

I-5-7 Anti-Perovskites

A structure identical to the perovskite structure is also observed in certain materials and alloys with compositions A_3BX, where A and B are typically metal atoms and X is an anion or a representative element (C, N, B, O, etc.). These phases are metallic, with A occupying the position of the anion in the ideal cubic perovskite structure Pm-3m (Nº. 221) **[29]**, while the X atoms occupy the octahedral positions XA_6 and the B atoms occupy the cube corners. This situation arises when the A and B cations are relatively close in size and the A cation is sufficiently small.

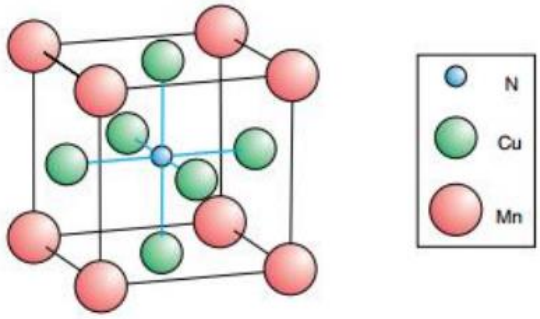

Figure I-9: Crystal structure of the anti-perovskite $CuNMn_3$ **[30]**.

The family of anti-perovskite materials also presents different possibilities for chemical combinations, similar to perovskites. These materials exhibit a range of intriguing physicochemical properties, ranging from large-gap insulators as seen in oxygen-based anti-perovskites A_3BO, to semiconductors as in nitrogen-based anti-perovskites A_3BN (with A: Mg, Ca, Sr, Ba and B from column V: P, As, Sb, Bi), to metals as in the case of A_3BN with A a rare earth or alkaline earth metal and B from columns III and IV, to superconductors as in $MgCNi_3$ **[31]**.

Anti-perovskite materials are highly important from a technological standpoint due to their high stability and hardness, making them useful in high-temperature environments, for cutting tools, and in hard coating applications**.**

I-5-8 Hybrid Perovskites

In 1978 **[32]**., the German crystallographer Dieter Weber from the University of Stuttgart conceived the idea of incorporating an organic molecule into the perovskite structure and synthesized for the first time the halogenated organic/inorganic hybrid perovskite $CH_3NH_3PbI_3$ (Figure I.10).

The surprising dynamic disorder of the methylammonium molecule $CH_3NH_3^+$ (denoted as MA) in MAPbI became the subject of study in subsequent works, but this material remained a scientific curiosity for many years. It was not until 2009

that the group of T. Miyasaka from Yokohama University **[33]**. brought this perovskite back into the spotlight by incorporating it into light-sensitive pigment solar cells.

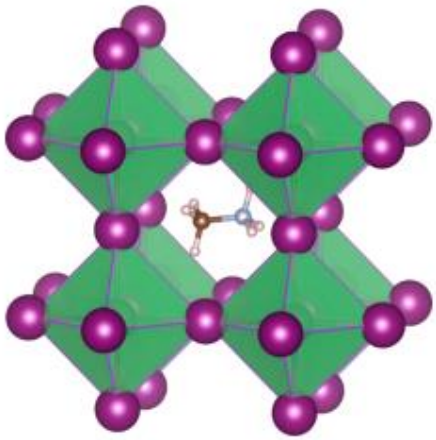

Figure I-10: Crystal structure of the hybrid perovskite $CH_3NH_3PbI_3$ **[32]**.

These materials are based on the "classic" three-dimensional (3D) cubic symmetry perovskite, where X is a halogen atom (Cl^-, Br^-, or I^-), B represents a divalent ionic metal such as Pb^{2+}, Sn^{2+}, or Ge^{2+}. The A cation can represent organic molecules such as methylammonium ($CH_3NH_3I^+$ = MA) **[34]**, formamidinium ($CH[NH_2]_2^+$ = FA) **[35]**, ethylammonium ($[CH_3CH_2NH_3]^+$ = EA) **[36]**, or guanidinium ($[C(NH_2)_3]^+$ = GA) **[37]**.

I-5-9 Layered Perovskites

Another well-known family of perovskite-structured compounds is that of layered compounds. These are three-dimensional (3D) perovskites that are typically organized in an infinite two-dimensional sequence along the $\vec{a}$ and $\vec{b}$ axes **[38]**. They possess different properties depending on their composition and crystallographic organization, making them useful for their dielectric, ionic conduction, or magnetic properties. This class of perovskite materials has

potential for a broad spectrum of technological applications. The most commonly encountered families of layered perovskites are presented in the remainder of this section.

I-5-10-a: Ruddlesden-Popper Layered Perovskite Structures

The general formulation $A'_2(A_{n-1}B_nX_{3n+1})$ describes the relationship between different layered perovskite structures. The formula for these compounds can thus be written as $AX_{-n}ABX_3$. In this case, "n" corresponds to the number of layers of octahedra BX_6 connected by their vertices. These compounds were named based on the work of Ruddlesden and Popper in 1958 **[39]**., focusing on the materials $Sr_3Ti_2O_7$ and $Sr_4Ti_3O_{10}$. See Figure I-11.

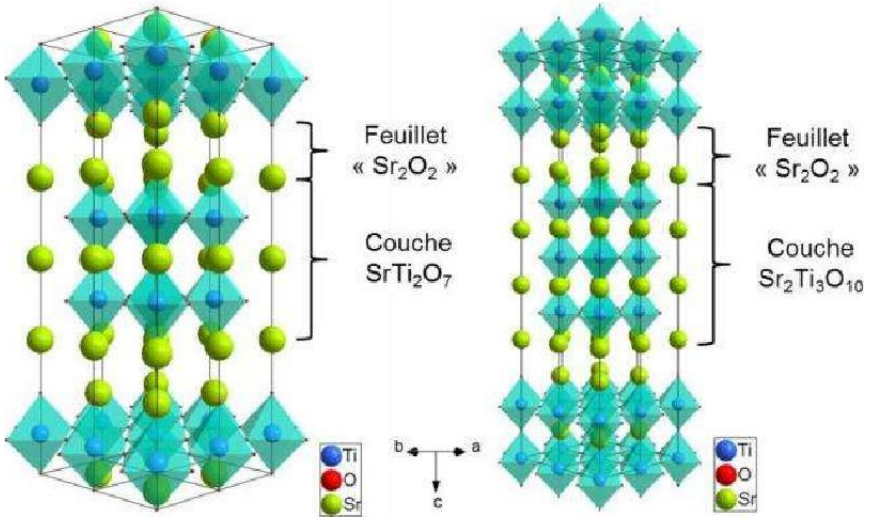

Figure I-11: Representation of the structures of $Sr_3Ti_2O_7$ and $Sr_4Ti_3O_{10}$ as described by Ruddlesden Popper**[39]**.

I-5-10-b: Dion-Jacobson Layered Perovskite Structures

These compounds were first named by Uma and Gopalakrishnan **[40].** They derive from the Ruddlesden-Popper compounds, featuring 2D perovskite layers with the formula $A_{n-1}B_nX_{3n+1}$, but they have only one interlayer of A cations. This single layer allows for higher ionic conductivity compared to the Ruddlesden-

Popper type compounds. Generally, Dion-Jacobson compounds crystallize in a centered quadratic cell, except in cases of tilts of the BX_6 octahedra or displacement of the A' cations. This structure is shown in Figure I-12 for two different compounds: $NaCa_2Ta_3O_{10}$ and $CsCa_2Ta_3O_{10}$ **[41].**

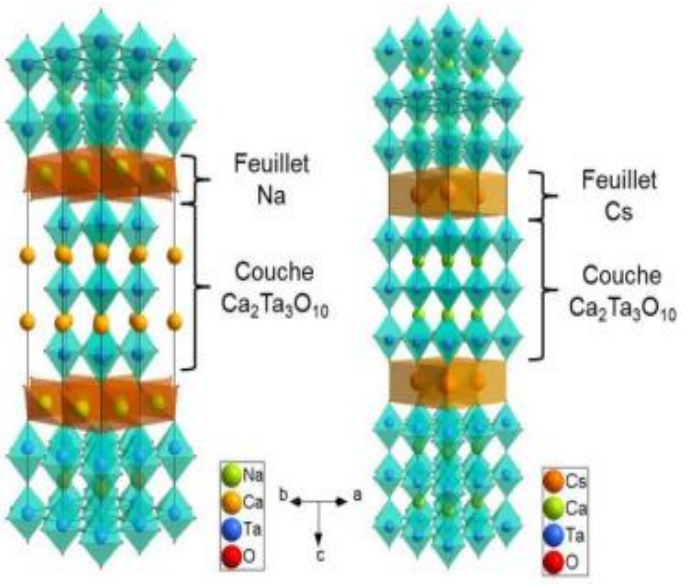

Figure I-12: Structure of Dion-Jacobson compounds $NaCa_2Ta_3O_{10}$ and $CsCa_2Ta_3O_{10}$ **[41]**

The shift between two layers, observed in the case of sodium but not cesium, is related to the size of the interlayer cation.

All Dion-Jacobson compounds are characterized by an order of the A and A' cations. The monovalent A' ion occupies the interlayer region, while the divalent or trivalent A cation occupies the cuboctahedral site of the perovskite layers. The coordination of the A' cations depends on their size.

I-5-10-c: Aurivillius Layered Perovskite Structures

Unlike the two previous structures where the interlayer cation varies between compositions, here it is exclusively the Bi^{3+} cation. The general formula $(Bi_2O_2)^{2+}(A_{n-1}B_nX_{3n+1})^{2-}$ describes the structure as a regular stacking of $(Bi_2O_2)^{2+}$

layers of the NaCl type and perovskite structure layers $(A_{n-1}B_nX_{3n+1})^{2-}$ The integer "n" represents the number of perovskite layers sandwiched between the $(Bi_2O_2)^{2+}$layers.

This type of structure, initially described by Aurivillius **[42]**, is that of $Bi_4Ti_3O_{12}$. The space group determined at that time was Fmmm. Figure I-13. Subsequently, other symmetries have been proposed, either monoclinic or orthorhombic. The most well-known examples are Bi_2WO_6 (n=1), Bi_3TiNbO_9 (n=2), and $Bi_4Ti_3O_{12}$ (n=3). Structurally, most of these compounds have a monoclinic (or orthorhombic) structure at low temperature, associated with a distortion in the perovskite layers, generally leading to ferroelectricity.

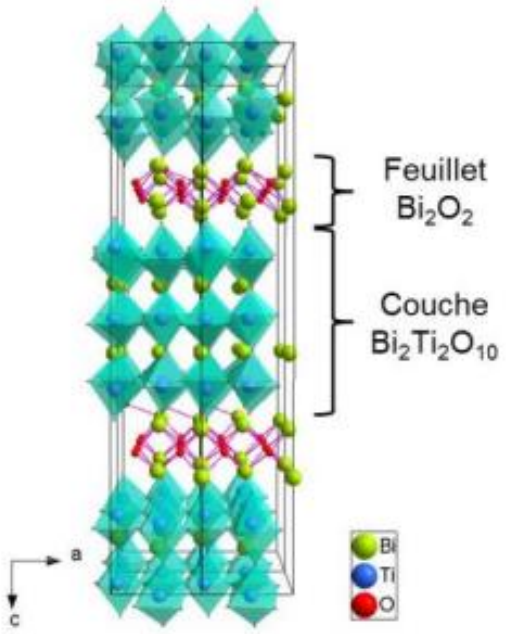

Figure I-13: Structure of the Aurivillius phase $Bi_4Ti_3O_{12}$ **[42]**

I-6- Physicochemical Properties and Technological Applications

Perovskite materials play a very important role in industrial technology due to the variety of their physicochemical properties and the different possibilities for

chemical combinations. They range from large-gap insulators to superconductors, and include ferroelectrics **[43].** They also exhibit a wide range of structural instabilities and other interesting physical properties, such as ionic conduction **[44]**, insulator-to-metal and metal-to-insulator transitions, structural changes under pressure and temperature, and vibrational, dielectric, and optical properties **[45]**.

In recent years, perovskites have found widespread applications in technology and industry. These materials are employed in a variety of applications, including memory devices, capacitors, microwave components, manometers, and ultrafast electronics **[46]**. These materials demonstrate relatively high-temperature superconductivity, exhibit piezoelectric properties by converting mechanical pressure or heat into electricity, serve as catalysts to accelerate chemical reactions, and show significant changes in electrical resistance when exposed to a magnetic field, a phenomenon known as magnetoresistance **[47,48]**.

Perovskites with transition metal ions occupying the B site exhibit a wide range of fascinating electronic and magnetic properties. his diversity is attributed not only to their chemical flexibility but also to the intricate roles played by transition metal ions in specific coordination with oxygen or halides. Magnetism and electronic correlations are typically associated with unfilled 3d electron orbitals, whereas pronounced dielectric properties are linked to filled 3d electron orbitals. These highly promising materials are progressively finding applications in transparent ceramics, environmentally friendly dyes, photovoltaic cells, and fuel cells **[49,50]**.

I-7 Information storage

The interest in using magnetism as an information medium arose when we were trying to minimize the energy required for storage. Indeed, the principle is based on ferromagnetic properties that allow the orientation of an applied external field to be stored in memory. This type of information storage does not require an electric current and therefore allows information to be stored in hard drives without requiring a battery or cell. Technology currently allows more and more data to be stored in a reduced space thanks to the miniaturization of devices and the increasingly high precision of the means of reading this information.

I-8 The general concept of spintronics

The basic concept of spintronics is to put magnetized materials in the path of electrons and use spin's effect on electron mobility in these materials. Initially proposed by Mott **[51]** in 1936, this influence was later shown experimentally and theoretically described in the late 1960s **[52].** The discovery of GMR **[53]** led to the first practical use of this influence. Today, spintronics is expanding in many ways, including tunnel magnetoresistance, spin transfer phenomena, molecular spintronics, spintronics with multiferroics, and many other phenomena that also take advantage of electron spin. A shift in spin electron energy bands parallel and antiparallel to the magnetization is a characteristic of ferromagnetic metals like iron or nickel (Figure (I-14)). The shift produces distinct populations for the two spin directions, which we will refer to as spin ↑ for the majority and spin ↓ for the minority spins. These bands are populated up to the Fermi level E_F.

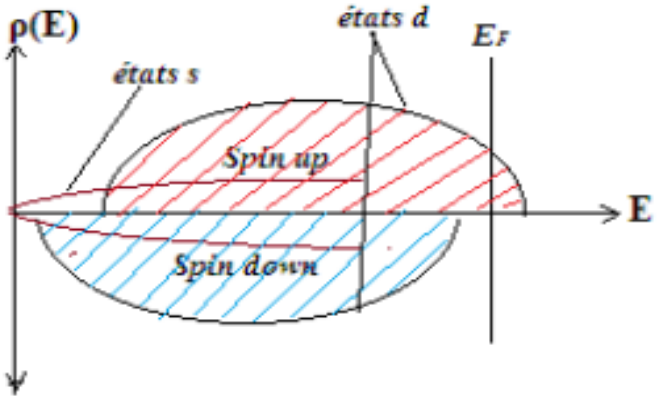

Figure I-14 . Standard density of states observed in a ferromagnetic metal.

I-8-1 Giant Magnetoresistance (GMR)

The influence of spin on electrical conduction in ferromagnetic metals was explored to account for specific anomalies observed in their resistivity near the Curie temperature. The states around the Fermi level - responsible for electrical conduction - induce a different conductivity if the spin is taken into account; we can therefore define two currents, one spin up and the other spin down. This conductivity is at the origin of giant magnetoresistance which exploits the influence of the quantum properties of the electron spin on the mobility of electrons in a ferromagnetic metal. The simplest system highlighting giant magnetoresistance consists of a multilayer or a bilayer (spin valves) of iron/chromium where the two iron layers are separated by a very thin non-magnetic layer (of the order of a nanometer), as shown in figure (I.15) below :

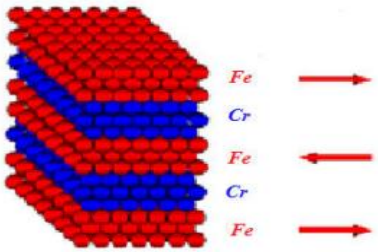

Figure I-15 : Alternating ultrathin layers of Iron and Chromium (arrows indicate the orientation of magnetism) **[53].**

If the direction of magnetization is the same in both magnetic layers, electrons with parallel spin can propagate easily. Electrons with antiparallel spin, on the other hand, collide. The total resistance, however, remains low. If the directions of magnetization in the two magnetic layers are opposite, the electrons will all be antiparallel in one of the two layers, undergoing many collisions. The total resistance will be increased.

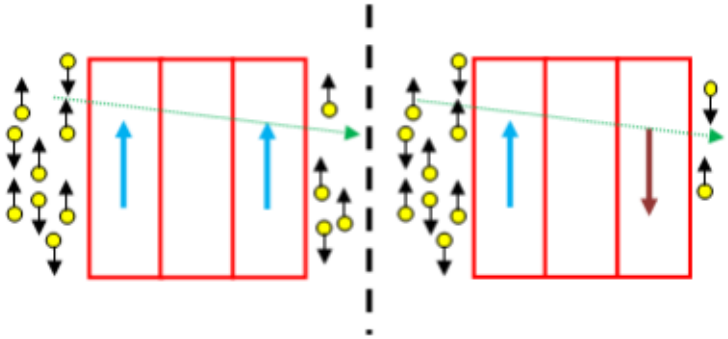

Figure I-16 : Parallel configuration (a) and antiparallel configuration (b).

If a magnetic field is applied, the configuration changes from an antiparallel state to a parallel state. This change is accompanied by a sharp drop in electrical resistance: this is the giant magnetoresistance effect, as shown in Figure (**I.16**). The magnetoresistance ratio, and Given by **[54]:**

$$MR = \frac{R_{AP} - R_p}{R_p} \qquad \text{(I-5)}$$

R_{Ap} is the resistivity measured in the antiparallel configuration and, R_p is the resistivity measured in the parallel state. The phenomenon of giant magnetoresistance is widely used in GMR read heads of modern hard disks. Another application is non-volatile magnetic memories (or MRAM). This technology is very promising to replace a number of hard disks in the form of SSD (Solid State Drive).

I-8-2 Giant magnetoresistance and electronic structure

A strong asymmetry of electronic structure between the majority and minority spin electrons increases the GMR of a multilayer. The asymmetry, In a ferromagnetic metal is due to the intrinsic electronic structure of the metal but, to the presence of defects and

impurities. The strongest asymmetries are obtained when the metal is doped with impurities whose electron diffusion cross section is very distinct for the two spin directions. For example, by doping nickel with cobalt or iron, we measure a resistivity more than 10 times higher for the minority spin electrons; this gives a value close to +1 for the asymmetry coefficient β, which is determined from the resistivities ρ↑ and ρ↓ by the following relation **[54]:**

$$\beta = \frac{\rho_{\downarrow} - \rho_{\uparrow}}{\rho_{\uparrow} + \rho_{\downarrow}} \qquad \text{(I-6)}$$

On the contrary, negative β values (i.e. ρ ↑ > ρ ↓) are obtained by doping nickel with chromium or vanadium. The shift of the energy states of the electrons, in the FM metal, in the two directions and the way of connection with the electronic states of the impurity little translated by a strong asymmetry in spin, here lies the explanation of this difference in the two cases.

I-8-3 Tunnel magnetoresistance (TMR)

We are now interested in the properties of tunnel magnetic junctions (TMJs), consisting of two ferromagnetic electrodes separated by an ultrathin insulator (the first tunnel magnetic junctions were studied in 1975 **[55]).** Their operating principle is illustrated in figure (**I-17**). If the magnetic moments of the two ferromagnets are parallel, there are many states available in the right electrode for the many electrons with spin ↓ present at the Fermi level in the left electrode.

If, however, the magnetization of the right electrode is reversed, and that of the left unchanged, there are very few places available for the transfer of electrons by tunneling through the junction, and its conductance is lower than in the previous case.

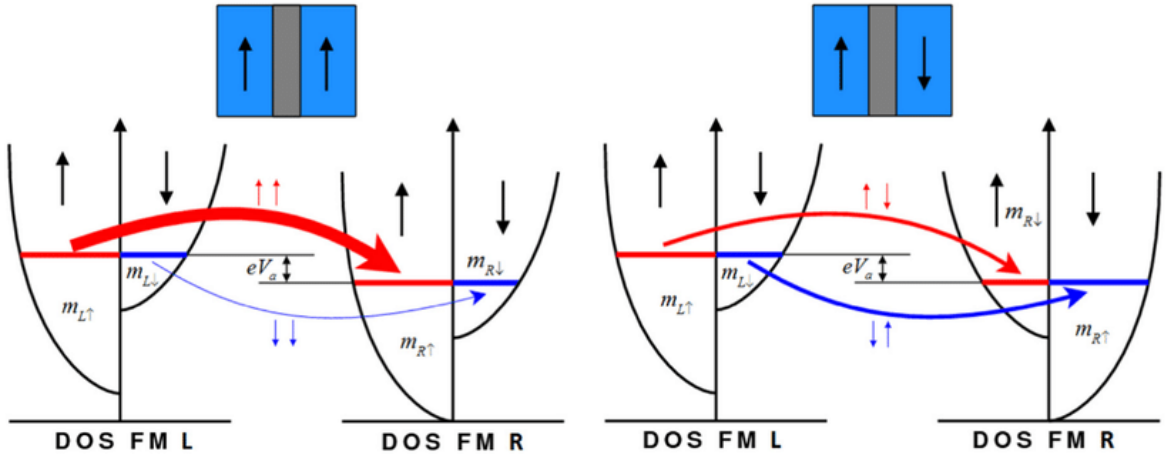

Figure I-17 : Principle of magnetic tunnel junctions **[55,56].**

The overall resistance of the magnetic tunnel junction in the parallel state is given by:

$$TMR = \frac{R_{\uparrow\downarrow} - R_{\uparrow\uparrow}}{R_{\uparrow\uparrow}} \qquad \text{(I-7)}$$

Where $R_{\uparrow\downarrow}$ is the resistivity measured in the antiparallel configuration and $R_{\uparrow\uparrow}$ is the resistivity measured in the parallel state.

I-9 Photovoltaic cells

For several years, several researches have agreed on the need to diversify energy sources and particularly renewable energies. In this context, photovoltaic cells are presented in the direct transformation of light energy into electrical energy, this transformation is due to the photovoltaic effect of the material used. Energy storage involves the interplay of three physical phenomena: the absorption of

light by the material, the transfer of light energy to electrons, and the collection of charge carriers at the electrodes. Upon illumination of the solar cell, photons with energies exceeding the semiconductor band gap are absorbed, resulting in the generation of electron-hole pairs. Within the solar cell, a device consisting of two n-type and p-type semiconductors allows the separation of the photo-generated charges as shown in Figure 10. At the contact, the electrons and holes recombine by diffusion, creating a zone devoid of mobile charges called the space charge zone: in this space charge zone, an electric field appears due to the presence of charged and immobile dopants. An electron-hole pair photo-generated in the space charge zone is immediately dissociated by the electric field: the holes accelerated towards the p-zone and the electrons towards the n-zone. Finally, the light energy of the solar rays is transformed into electricity through the production and transport in a semiconductor material of positive and negative electric charges under the effect of light.

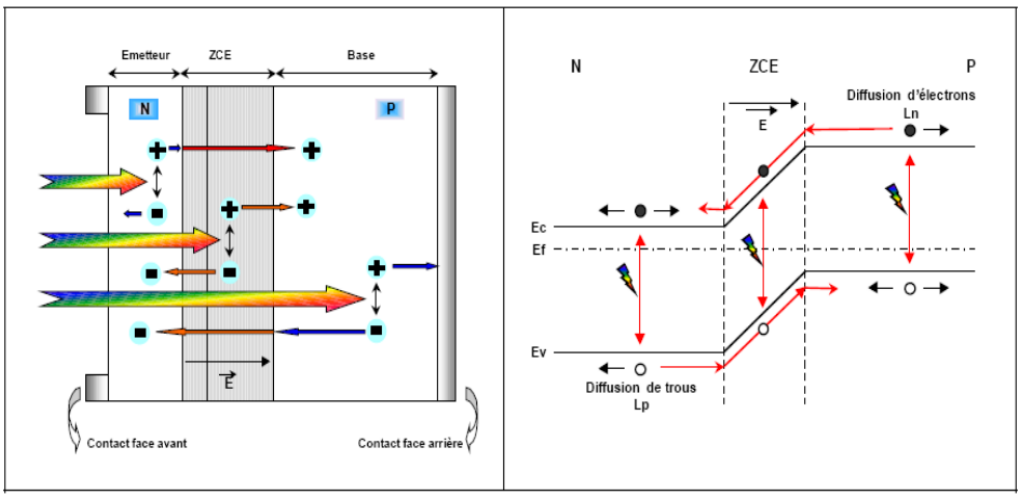

Figure I-18. Operating principle of a photovoltaic cell composed of a p-n junction

I-10 Conclusion

This first chapter provides a state-of-the-art overview of perovskite materials. We have presented general information about their crystal structures, classifications, and practical properties. These interesting physical properties have garnered enormous interest and have become one of the most motivating subjects in scientific research due to the simplicity of their crystal structure. They are easy to produce using simple and cost-effective techniques. "As a result, these materials can integrate the properties of both organic and inorganic components, combining the flexibility of the organic fraction with the thermal stability and mechanical rigidity of the inorganic fraction within a single material.

Given the interesting properties discussed in this chapter, the following chapter will explore various numerical modeling methods based on first-principles quantum simulations, "ab-initio" techniques, and the density functional theory (DFT) formalism employing the linearized augmented plane wave (LAPW) method.

References

[1] GLAZER, A. M. Perovskites modern and ancient. By Roger H. Mitchell. Thunder Bay, Ontario: Almaz Press, 2002. Price USD 70.00. ISBN 0-9689411-0-9. *Acta Crystallographica Section B: Structural Science*, 2002, vol. 58, no 6, p. 1075-1075.

[2] Tsur, Yoed, Timothy D. Dunbar, and Clive A. Randall. "Crystal and defect chemistry of rare earth cations in BaTiO3." Journal of Electroceramics 7.1 : 25-34, (2001).

[3] Ball, C. J., et al. "Structures in the system CaTiO3/SrTiO3." Journal of Solid State Chemistry 139.2 : 238-247, (1998).

[4] J. Lelievre, "Nouveaux matériaux sans plomb à base de bismuth: vers des composés de type (A, A')(B) O_3 et (A, A')(B, B') O_3," Thèse de doctorat. Université de Limoges. 2017.

[5] YASHIMA, Masatomo, et al. Conduction path and disorder in the fast oxide-ion conductor (La0. 8Sr0. 2)(Ga0. 8Mg0. 15Co0. 05) O2. 8. *Chemical physics letters*, 2003, vol. 380, no 3-4, p. 391-396.

[6] SOUIDI, Amel. *Etude des propriétés spintroniques du double Perovskite type ABCO6*. Tesis Doctoral. Université de Mostaganem-Abdelhamid Ibn Badis.

[7] GOLDSCHMIDT, V. M. Krystallbau und chemische Zusammensetzung. *Berichte der deutschen chemischen Gesellschaft (A and B Series)*, 1927, vol. 60, no 5, p. 1263-1296.

[8] Fedorovskiy, A. E., Drigo, N. A., & Nazeeruddin, M. K. Small Methods, 2020, vol. 4, no 5, p. 1900426

[9] PHILIPP, J. B., et al. Structural and doping effects in the half-metallic double perovskite A 2 CrWO 6 (A= Sr, Ba, and Ca). *Physical Review B*, 2003, vol. 68, no 14, p. 144431.

[10] HASNAT, K., et al. Ftir and Raman Spectroscopic Study of a Complex Perovskite: Ca 0.91-X Ce 0.09 Rb 0.04 Cs x [(Zr 0.50 Ti 0.45) Al 0.05] O 3, X= 0.2 to 0.4, Dedicated for Radioactive Waste Confinement. *Advances in Materials Science*, 2020, vol. 20, no 2, p. 81-94.

[11] Wang, Z. L., and Z. C. Kang. "Perovskite and Related Structure Systems." Functional and Smart Materials. Springer, Boston, MA, 93-149, (1998)

[12] Talapatra, A., Uberuaga, B. P., Stanek, C. R., & Pilania, G. *Chemistry of Materials*, 2021, vol. 33, no 3, p. 845-858.

[13] Li, C.; Soh, K. C. K.; Wu, P. Formability of ABO3 perovskites. J. Alloy Compd, 372, 40–48, (2004).

[14] HUTTON, J.; NELMES, R. J.; SCHEEL, H. J. Extinction corrections for a highly perfect crystal (SrTiO3). *Acta Crystallographica Section A: Crystal Physics, Diffraction, Theoretical and General Crystallography*, 1981, vol. 37, no 6, p. 916-920.

[15] SHROUT, Thomas R.; HALLIYAL, Arvind. Preparation of lead-based ferroelectric relaxors for capacitors. 1987.

[16] MULLER, Olaf; ROY, Rustum. The major ternary structural families. *(No Title)*, 1974.

[17] J. B. Goodenough and J. Longo, Landolt-Börnstein Tabellen Neue Serie III/4a, Springer Verlag, Berlin (1970).

[18] GELLER, S.; WOOD, E. A. Crystallographic studies of perovskite-like compounds. I. Rare earth orthoferrites and YFeO3, YCrO3, YAlO3. *Acta Crystallographica*, 1956, vol. 9, no 7, p. 563-568.

[19] O. Muller, "The major ternary structural families," Crystal chemistry of non-metallic materials. In The Major Ternary Structural Families (Vol. 4, p. 143). Springer-Verlag New York.1974.

[20] KUSUSE, Yoshiro, et al. Structural phase transitions in EuNbO3 perovskite. *Journal of Solid State Chemistry*, 2016, vol. 239, p. 192-199.

[21] THORNTON, G.; TOFIELD, B. C.; HEWAT, A. W. A neutron diffraction study of LaCoO3 in the temperature range 4.2< T< 1248 K. *Journal of Solid State Chemistry*, 1986, vol. 61, no 3, p. 301-307.

[22] RACCAH, P. M.; GOODENOUGH, J. B. First-Order Localized-Electron⇆ Collective-Electron Transition in LaCo O 3. *Physical Review*, 1967, vol. 155, no 3, p. 932.

[23] TASPINAR, Ercan; TAS, A. Cuneyt. Low-temperature chemical synthesis of lanthanum monoaluminate. *Journal of the American Ceramic Society*, 1997, vol. 80, no 1, p. 133-141.

[24] ŁUKASZEWICZ, Kazimierz; KARUT-KALICIŃSKA, Jarosława. X-ray investigations of the crystal structure and phase transitions of YMnO3. *Ferroelectrics*, 1974, vol. 7, no 1, p. 81-82.

[25] MENG, Xiangying; WEN, Xiaohong; QIN, Gaowu. DFT study on elastic and piezoelectric properties of tetragonal BaTiO3. *Computational Materials Science*, 2010, vol. 49, no 4, p. S372-S377.

[26] FILIPPETTI, Alessio; HILL, Nicola A. First principles study of structural, electronic and magnetic interplay in ferroelectromagnetic yttrium manganite. *Journal of magnetism and magnetic materials*, 2001, vol. 236, no 1-2, p. 176-189.

[27] KAMEL, Rida. Synthèse, caractérisation et propriétés catalytiques des oxydesLa1-xMxCrO3 (M= Sr et Ce). *Diss. Thèsedoctorat, UniversitéMentouriCanstantine*, 2008.

[28] EZEALIGO, Blessing N.; EZEMA, Fabian. Piezoelectric and dielectric properties of phase-re-engineered barium titanate prepared by self-propagating high-temperature synthesis. En *Surface Modification and Functionalization of Ceramic Composites*. Elsevier, 2023. p. 447-460.

[29] Benmalem, Y., et al. "Thermoelectric, electronic and structural properties of CuNMn3 cubic antiperovskite." Journal of Computational Electronics 17.3 : 881-887, (2018).

[30] Chi, E. O., W. S. Kim, and N. H. Hur. "Nearly zero temperature coefficient of resistivity in antiperovskite compound CuNMn3." Solid State Communications 120.7-8 : 307-310, (2001).

[31] Diener, Pascale. Longueur de pénétration magnétique dans des supraconducteurs exotiques. Diss. Université Joseph-Fourier-Grenoble I, (2008).

[32] Weber, Dieter. "CH3NH3PbX3, ein Pb (II)-system mit kubischer perowskitstruktur/ CH3NH3PbX3, a Pb (II)-system with cubic perovskite structure." Zeitschrift für naturforschung B 33.12 : 1443-1445, (1978).

[33] Kojima, Akihiro, et al. "Organometal halide perovskites as visible-light sensitizers for photovoltaic cells." Journal of the American Chemical Society 131.17: 6050-6051, (2009).

[34] Liu, Lijia, et al. "Tracking the formation of methylammonium lead triiodide perovskite." Applied physics letters 107.6: 061904, (2015).

[35] Guo, Lei, Gang Tang, and Jiawang Hong. "Mechanical properties of formamidinium halide perovskites FABX3 (FA= CH (NH2) 2; B= Pb, Sn; X= Br, I) by first-principles calculations." Chinese Physics Letters 36.5: 056201, (2019).

[36] Bicak, Niyazi. "A new ionic liquid: 2-hydroxy ethylammonium formate." Journal of Molecular Liquids 116.1: 15-18, (2005).

[37] Mason, Philip E., et al. "The structure of aqueous guanidinium chloride solutions." Journal of the American Chemical Society 126.37: 11462-11470, (2004).

[38] Goto, T., et al. "Elastic soft mode in perovskite-type layer-structure materials." Physical Review B 22.7: 3452, (1980).

[39] Ruddlesden, S. N., and P. Popper. "The compound Sr3Ti2O7 and its structure." Acta Crystallographica 11.1: 54-55, (1958).

[40] Uma, S., and J. Gopalakrishnan. "Polymerization of aniline in layered perovskites." Materials Science and Engineering: B 34.2-3: 175-179, (1995).

[41] Mao, Lingling, et al. "Hybrid Dion–Jacobson 2D lead iodide perovskites." Journal of the American Chemical Society 140.10: 3775-3783, (2018).

[42] Aurivillius, Bengt. "Mixed Bismuth Oxides with Layer Lattices I. The Structure Type of CaNb2Bi2O9." Arkiv kemi 1: 463-480, (1949).

[43] Burns, Gerald, and Bruce A. Scott. "Lattice Modes in Ferroelectric Perovskites: PbTiO3." Physical Review B 7.7: 3088, (1973).

[44] Mizusaki, Junichiro, Kimiyasu Arai, and Kazuo Fueki. "Ionic conduction of the perovskite type halides." Solid State Ionics 11.3: 203-211, (1983).

[45] Lin, Qianqian, et al. "Electro-optics of perovskite solar cells." Nature Photonics 9.2: 106-112, (2015).

[46] Piticescu, R. M., et al. "Hydrothermal synthesis of perovskite based materials for microelectronic applications." Journal of optoelectronics and advanced materials 8.2: 543, (2006).

[47] Uchino, Kenji. "Glory of piezoelectric perovskites." Science and technology of advanced materials 16.4: 046001, (2015).

[48] Moritomo, Y., et al. "Giant magnetoresistance of manganese oxides with a layered perovskite structure." Nature 380.6570: 141-144, (1996).

[49] Bhalla, A. S., Ruyan Guo, and Rustum Roy. "The perovskite structure—a review of its role in ceramic science and technology." Materials research innovations 4.1: 3-26, (2000).

[50] Wang, Rui, et al. "A review of perovskites solar cell stability." Advanced Functional Materials 29.47: 1808843, (2019).

[51] N.F. Mott, Proc. Roy. Soc. A, 153 (1936) 699.

[52] B. Loegel et F. Gautier, J. Phys. Chem. Sol. 32 (1971) 2723.

[53] H.Zabel, Journal of Physics: Condensed Matter 11.48 (1999): 9303.

[54] A. Fert, J. A. Katine, R. A. Buhran, D. C. Ralph, Appl. Phys. Lett., Vol. 77, (2000), 3809-3811.

[55] M. N. Baibich, J. M. Broto, A. Fert, F. Nguyen Van Dau, and F. Petroff, Phys. Rev. Lett. 61 (1988), 2472- 2475.

[56] M. Julliere, Phys. Lett., Vol. 54A, n°3, (1975), 225-226.

Chapter II:

Overview of calculation methods

II-1 Introduction:

Density functional theory (DFT) is the most widely used theory in physics of condensed matter and it is used very widely in quantum chemistry thanks to its efficiency and generality. DFT is capable of treating both molecular and extended systems, enabling the study of electronic properties based solely on the electron density, in principle with exact accuracy. Moreover, determining the electron density does not require knowledge of the many-body wave function, significantly simplifying the computational process.

The origins of DFT can be traced back to the model developed by Lewellyn Thomas and Enrico Fermi in the late 1920s **[1,2]**. However, we would have to wait until the mid-1960s and the contributions from Pierre Hohenberg, Walker Kohn and Li Sham to establish the formalism theory on which the current method is based **[3].** So its principle is based on a reformulation of an N-body problem into a single-body problem, this is electron density **[4].** The DFT approach is founded on the foundations of quantum mechanics and does not involve only a limited number of input data. For a given system with several bodies, it allows to solve the Schrödinger equation without the introduction of parameters adjusted by experience **[5].**

The following chapter aims to present a concise summary of the fundamental concepts of DFT, its common implementations, approximations, obstacles encountered, and a brief overview of how Wien2K programs work.

II-2 Bloch's theorem

The problem of electrons in a solid is fundamentally a multi-electron problem, because the Hamiltonian includes not only the one-electron potential which describes the interaction between electrons and ions, but also for the interactions

between electron-electron. A potential with the lattice's periodicity is used to describe these interactions in the independent electron approximation:

$$U\left(\vec{r}+\vec{R}\right)=U\left(\vec{r}\right) \qquad \text{(II -1)}$$

The wave function is then expressed as the product of a periodic function of the same periodicity as the network $U_{\vec{k}}(\vec{r})$ and a plane wave $e^{i\vec{k}\cdot\vec{r}}$ (takes in consideration the translation of the lattice):

$$\Psi_{\vec{k}}\left(\vec{r}+\vec{R}\right)=e^{i\vec{k}\cdot\vec{r}}\Psi_{\vec{k}}\left(\vec{r}\right) \qquad \text{(II -2)}$$

This condition of invariance by translational symmetry therefore leads to the definition of a new quantum number specific to Bloch orbitals, the wave vector $\vec{k}$. This vector is defined in reciprocal space.

In the case of periodic systems, the description of the system and its study are limited to the region of space defined by the unit cell, Which is at the level of the first Brillouin zone in reciprocal space.

II-3 Schrödinger's equation

Obtaining predictions for observables from ab-initio calculations involves determining the wave function of the system studied. The concepts of quantum chemistry come from quantum physics applied to molecular systems. The goal is to describe a system composed of M nuclei and N electrons by a function of their coordinates: the wave function:

$$\Psi=\Psi\left(X_1,X_2,...X_N;R_1,R_2,...R_M\right) \qquad \text{(II -3)}$$

Each nuclear coordinate R_A or electronic X_i is, for each particle, the set of its position coordinates in space R^3 to which a so-called spin coordinate is added, in order to fully describe each particle. At the molecular level, physics no longer

responds to the laws of Newtonian mechanics, and we must use the rules of quantum physics.

The observable physical quantities are obtained using operators which are applied to the wave function. The latter, by definition, fully describes a system of particles in a given state. For this system, it is the solution to the Schrödinger equation:

$$H\Psi = E\Psi \qquad \text{(II -4)}$$

The wave function by itself has no physical meaning, but it entirely defines the system in a given state. We can deduce from this all the intrinsic quantities of the studied system. The Hamiltonian operator H has an eigenvalue equation known as the Schrödinger equation. The following is given for a molecular system with M nuclei and N electrons:

$$H = -\sum_{i=1}^{N} \frac{\hbar^2}{2m} \nabla_i^2 - \sum_{A=1}^{M} \frac{\hbar^2}{2M_A} \nabla_A^2 - \sum_{A,i} \frac{Z_A e^2}{r_{Ai}} + \sum_{i,j \neq i} \frac{e^2}{r_{ij}} + \sum_{A,B \neq A} \frac{Z_A Z_B e^2}{R_{A,B}} \qquad \text{(II -5)}$$

Where The first two terms of the equation correspond respectively to the kinetic energy of electrons and nuclei. The last three are the set of Coulomb interactions for each pair of particles: electron-nucleus, nucleus-nucleus and electron-electron. The Hamiltonian is therefore a sum of operators of different types:

$$H = T_e + T_n + V_{en} + V_{ee} + V_{nn} \qquad \text{(II -6)}$$

The challenge is to find the solution of equation (I-4), not only in the simplest case of the hydrogen atom, but also in the case of more complex problems with several ions and electrons forming a solid.

II-4 The Born-Oppenheimer approximation (adiabatic)

Generally, quantum calculations are based on the possibility of treating electrons and ions of a real system separately. Given the significant mass difference between these two entities (ions, electrons), this represents the adiabatic approximation of Born and Oppenheimer [6]. In other words, electrons may pass

through a solid far more quickly than nuclei since they are far lighter than ions. Thus, the electronic configuration can be regarded as fully relaxed in its ground state for each ion position throughout their movements.

As an initial approximation, the total wave function of the system can be expressed as the sum of two components: one describing the electrons and the other the ions, with the latter depending parametrically on the ionic positions:

$$\Psi(\vec{r},\vec{R}) = \varphi(\vec{R})\,\Psi(\vec{r}) \qquad \text{(II -7)}$$

Where $\vec{R} = \{\vec{R}_I\}$ is the set of all nuclear coordinates, and $\vec{r} = \{\vec{r}_i\}$ is the same quantity for all electrons in the system

The solution of the Schrödinger equation can therefore be limited to the electronic problem

II-5 The Hartree-Fock approximation

However, the Born-Oppenheimer approximation alone is inadequate for solving the Schrödinger equation due to the complexity of electron-electron interactions. For this reason, it is often combined with Hartree's approximation **[7],** wherein the electrons are treated as independent and identical. The Hamiltonian is expressed as a sum of Fock operators **[8],** each representing a single-electron term. That said, electrons are still influenced by other electrons in the form of an effective potential. This view is very widespread in the various methods of quantum chemistry.

$$H_e = \sum_i H_i \qquad \text{(II -8)}$$

$$H_e = \sum_i T_i + V_{A,i}(r) + \sum_i V_{eff}(r) \qquad \text{(II -9)}$$

To each electron corresponds an orbital and the total wave function is written as a product of one-particle wave functions , which are orthogonal to each other:

$$\Psi(r_1, r_2, r_3, ...r_N) = \Psi_1(r_1) \cdot \Psi_2(r_2) \cdot \Psi_3(r_3) \cdots \Psi_N(r_N) \quad \text{(II -10)}$$

A functional of the wave function is used to define the system's total energy:

$$E = \sum_{i=1}^{N} \varepsilon_i \quad \text{(II -11)}$$

The wave function (I-10) is incompatible with the Pauli principle which requires that the sign of Ψ must change if one permutes two of its arguments. This problem is addressed by the description of the wave function as a Slater determinant constructed from the N spin-orbitals (the spin-orbitals there come from the $N/_2$ spatial orbitals combined with two spin functions α and β).

$$\psi(x_1, x_2, x_3, ..., x_N) = \frac{1}{\sqrt{N!}} \begin{vmatrix} \Psi_1(x_1) & \cdot & \cdot & \Psi_N(x_1) \\ \cdot & \cdot & \cdot & \cdot \\ \cdot & \cdot & \cdot & \cdot \\ \Psi_1(x_N) & \cdot & \cdot & \Psi_N(x_N) \end{vmatrix} \quad \text{(II -12)}$$

By the variational method, the choice of the best spin-orbitals corresponds to the minimum of the electronic energy (E_e). This optimal electronic wave function, achieved for the lowest energy, will always be above the exact energy. The energy minimization procedure is a self-consistent procedure with orthonormality constraints for the orbitals.

$$E[\Psi] = \frac{\int \Psi^* H \Psi}{\int \Psi^* \Psi} d\tau \quad \text{(II -13)}$$

The variational calculus shows that each wave function $\Psi_i(r)$ must, in order to minimize the average energy $\langle E \rangle$, itself be a solution of a second order differential equation which has the form of a one-particle Schrödinger equation.

$$\left[-\frac{1}{2}\nabla^2 + V(r) + V_d(r) \right] \Psi_i(r) = \varepsilon_i \Psi_i(r) \quad \text{(II -14)}$$

V_d is the potential of direct interaction.

In this model we treat the electronic cloud seen by an electron as a regular distribution of negative charges with the charge density ρ(r) defined by

$$\rho(r) = \sum_i |\Psi(r)|^2 \qquad \text{(II -15)}$$

The exchange term is defined by:

$$V_{exch}\Psi_i(r) = -\sum_{j\neq i}\int \frac{\Psi_j^*(r')\Psi(r')}{|r-r'|}\Psi_j(r)dr' \qquad \text{(II -16)}$$

We thus obtain the Hartree-Fock equations

$$\left[-\frac{1}{2}\nabla^2 + V(r) + V_d(r)\right]\Psi_i(r) - \sum_{j\neq i}\int \frac{\Psi_i^*(r')\Psi(r')}{|r-r'|}\Psi_i(r)dr'\Psi_j(r) = \varepsilon_i\Psi_i(r) \qquad \text{(II -17)}$$

The system's total energy is specified as a functional of the wave function in the Hartree-Fock approach. This approach considers electronic interaction but disregards the relationship between one electron's movement and that of other electrons. The Hartree-Fock approximation yields approaches that are appropriate for tiny systems and only consider a portion of the correlation energy. The functional technique of density (DFT: Density Functional Theory) is far more appropriate for bigger molecules or solids.

II-6 The density functional theory

II-6-1 Hohenberg and Kohn's theorem

The foundation of the density functional theory is the Hohenberg and Kohn **[9]** (1965) theorem, which states that the eigenvalue of an observable in the ground state is a unique functional of the density::

$$E = E[\rho] \qquad \text{(II -18)}$$

Thus the external potential is determined with a constant near if one knows the density of the ground state, and the whole Hamiltonian of the system is known if the kinetic energy and the inter-particle interaction are specified.

The variational character of the functional is given by:

$$E[\rho]=\langle\psi[\rho]|\hat{T}+\hat{V}+\hat{W}|\psi[\rho]\rangle \qquad \text{(II -19)}$$

where V is the external potential.

The energy of the ground state is :

$$E_0 = E[\rho_0] \qquad \text{(II -20)}$$

ρ_0 : the density of the ground state.

$$E_0\langle E[\rho]\Rightarrow E_0 = min\,E[\rho] \qquad \text{(II -21)}$$

II-6-2 The notion of the density functional

We can write:

$$E[\rho]=\langle\psi[\rho]|\hat{T}+\hat{W}|\psi[\rho]\rangle+\langle\psi[\rho]|\hat{V}|\psi[\rho]\rangle \qquad \text{(II -22)}$$

The kinetic energy and the inter-particle interaction, denoted by $\hat{T}$ and $\hat{w}$, respectively, are independent of the external potential.

The charge density r(r) has a special universal function that is independent of the external potential, according to Hohenberg and Kohn. Examples of this function include:

$$E[\rho]=F_{HK}[\rho]+\int d^3r\,V(\vec{r})\,\rho(\vec{r}) \qquad \text{(II -23)}$$

F_{HK} is called Hohenberg and Kohn functional . It is the same for (atom, molecule and solid).

II -6-3 the equations of Khon and Sham

The different interactions present in the functional will only be available if the Kohn - Sham functional **[10]** is known. In most cases, the expression of F is presented as :

$$F[\rho]=T[\rho]+V_{e-e}[\rho] \qquad \text{(II -24)}$$

T : The kinetic energy.

V_{e-e} : The interaction between electron-electron

If we have a set of non-interacting electrons in a complex potential with the same density ρ then :

$$E[\rho(r)]=T^{non-int}[\rho(r)]+J[\rho(r)]+E_{XC}[\rho(r)]+\int V_{EXT}\rho(r)d^3r \qquad \text{(II -25)}$$

J : The classical coulomb interaction energy has the following expression :

$$J[\rho(r)]=1/2\iint\frac{\rho(r)\rho(r')}{|r-r'|}d^3rd^3r' \qquad \text{(II -26)}$$

$T^{non-\text{int}}$: The energy of the non-interacting system and it is given by :

$$T^{non-int}=\frac{1}{2}\sum_i|\nabla\psi_i|^2 \qquad \text{(II -27)}$$

$\int V_{EXT}\rho(r)d^3r$ is the potential energy of interaction with the external field.

E_{xc} is the energy of exchange and correlation.

Thus, the potential for exchange and correlation is given by :

$$V_{XC}(r)=\frac{\partial E_{XC}[\rho(r)]}{\partial\rho(r)} \qquad \text{(II -28)}$$

The term exchange and correlation results from the electron-electron interaction.

This interaction of an electrostatic nature (Colombian), reflects the repulsion between electrons. So to solve this problem, it is assumed that the electrons have distinct spatial configurations, which decreases their interaction energies.

So, knowledge of the term of exchange and correlation is necessary for the resolution of the electronic system. Unfortunately, $E_{xc}(\rho)$is not known exactly, this is why we call for the approximation of the local density.

II-6-4 the local density approximation (LDA)

It is the most efficient method for the determination of the term of exchange and correlation. The approximation of the local density (LDA, Local Density Approximation) **[11]** gives some approximation of this energy which is supposed to be related only to the local density and to the energy of exchange and correlation, which relates to each particle meets immersed in an electronic gas. In another way, the exchange and correlation energy of a homogeneous electron gas is equal to the exchange and correlation energy of a non-homogeneous electron gas having the same density $\rho(r)$ at point r .

The total exchange and correlation energy $E_{xc}(\rho)$ for all the volume is expressed as :

$$E_{xc}^{LDA} = \int d^3 r\, \rho(r) \varepsilon_{xc}[\rho(r)] \qquad \text{(II-29)}$$

with :

$$\varepsilon_{xc}(r) = \varepsilon_{xc}^{hom}[\rho(r)] \qquad \text{(II -30)}$$

$\varepsilon_{xc}^{hom}[\rho(r)]$ is the homogeneous density of a homogeneous electron gas

II-6-5 The generalized gradient approximation (GGA)

The presence of this approximation **[12,13]** is intended to correct, but sometimes they were far from those decided by experience, for this it was necessary to add a term to the energy of exchange and correlation in order to correct the results. Effectively, an expression similar to expression (I-29) is used only $\varepsilon_{xc}(\rho)$ is replaced by $\varepsilon_{xc}(\rho, |\nabla\rho|)$.

Then, the exchange and correlation energy E_{xc} in the generalized gradient approximation (GGA) is given by :

$$E_{xc}^{GGA}[\rho] = \int f[\rho(r), \nabla\rho(r)]\, d^3 r \qquad \text{(II -31)}$$

II-6-6 The (DFT + U) approximation

The basic idea of DFT+U is to describe the strongly correlated electronic states of a system (usually the localized d or f orbitals) using an additional term inspired by the Hubbard model, such as a corrective term. In DFT+U the energy functional of a system can be written as follows:

$$\mathrm{E_{DFT+U}} = \mathrm{E_{DFT}} - \mathrm{E_{dc}} + \mathrm{E_{Hub}} = \mathrm{E_{DFT}} - \frac{\mathrm{U}}{2}\mathrm{N_d}(\mathrm{N_d} - 1) + \frac{\mathrm{U}}{2}\sum_{i \neq j} n_i\, n_j \quad \text{(II -32)}$$

The second term is called the double counting term. Because we explicitly add the third term (Hubbard term in mean field theory), we must remove the contribution of these orbitals included in the E_{DFT} functional, so as not to count their contributions twice. $N_d = \Sigma_i\, n_i$, ni is the set of occupations of the localized orbitals. There are two ways to formulate the term double counting: The first method is the approximation of the fully localized limit (FLL), also called the atomic limit, E_{dc}^{FLL} is written **[14]** :

$$E_{dc}^{FLL} = \frac{1}{2}Un(n-1) - \frac{1}{2}J\ \sum_{\sigma} n^{\sigma}(n^{\sigma} - 1) \quad \text{(II -33)}$$

U Represents the energy provided to move an electron from one atom to another. The parameter J represents the exchange term of Hund's rules.

The second method is the approximation of mean fields (Around Mean Field (AMF)) **[15]** :

$$E_{dc}^{AMF} = \frac{1}{2}Un^{\uparrow}n^{\downarrow} - \frac{1}{2}\left(\left(n^{\uparrow}\right)^2 + \left(n^{\downarrow}\right)^2\right)\frac{2l}{2l+1}(U - J) \quad \text{(II -34)}$$

Where l is the quantum number associated with total angular momentum.

II-6-7 The modified Becke-Johnson potential (mBJ)

In order to improve the values of the gap energies, underestimated by the previous approximations (LDA and GGA), Tran and Blaha **[16]** proposed in 2009 a new version of exchange potential noted (mBJ) which modifies and improves the potential of Becke and Johnson (BJ) **[17]** published in 2006, which was implemented in the Wien2k code.

The mBJ potential proposed by Tran and Blaha has the following form:

$$V_{x,\sigma}^{mBJ}(\vec{r}) = cV_{x,\sigma}^{BR}(\vec{r}) + (3C-2)\frac{1}{\pi}\sqrt{\frac{5}{12}}\sqrt{\frac{2t_\sigma(\vec{r})}{\rho_\sigma(\vec{r})}} \quad \text{(II -35)}$$

The parameter is given by the following relation:

$$c = \alpha + \beta\left(\frac{1}{V_{cell}}\int\frac{|\nabla\rho(\acute{r})|}{\rho(\acute{r})}\,d^3\acute{r}\right)^{\frac{1}{2}} \quad \text{(II -36)}$$

With V_{cell}: is the volume of the unit cell, α and β are two independent parameters whose values are obtained by a dependent adjustment to the experimental results:

$$\alpha = -0.012 \quad and \quad \beta = 1.023\ Bohr^{\frac{1}{2}} \quad \text{(II -37)}$$

$V_{x,c}^{BR}(\vec{r})$ is the semi-local Becke-Roussel (BR) potential **[18]**, which was proposed to model the Coulomb potential created by the exchange holes, it is defined as follows:

$$V_{x,c}^{BR}(\vec{r}) = -\frac{1}{b_\sigma(\vec{r})}\left(1 - e^{-x_\sigma(\vec{r})} - \frac{1}{2}x_\sigma(\vec{r})e^{-x_\sigma(\vec{r})}\right) \quad \text{(II -38)}$$

The function $x_\sigma(\vec{r})$, can be calculated from the following non-linear equation:

$$\frac{x_\sigma(\vec{r})e^{-\frac{2x_\sigma(\vec{r})}{3}}}{x_\sigma(\vec{r})-2} = \frac{12}{3}\pi^{\frac{2}{3}}\frac{\rho_\sigma^{\frac{5}{3}}(\vec{r})}{(\nabla^2\rho_\sigma(\vec{r})-4t_\sigma(\vec{r})-\frac{|\nabla\rho(\vec{r})|^2}{\rho(\vec{r})}} \quad \text{(II -39)}$$

$t_\sigma(r) = \frac{1}{2}\sum_{i=1}^{N\sigma}\nabla\emptyset_{i,\sigma}^*(r)\,\nabla\emptyset_{i,\sigma}(r)$ Represents the density of kinetic energy.

The term $b_\sigma(\vec{r})$ is calculated by the following relation :

$$b_\sigma(\vec{r}) = \left(\frac{x_\sigma^3(\vec{r})e^{-x_\sigma(\vec{r})}}{8\pi\rho_\sigma(\vec{r})}\right)^{\frac{1}{3}} \quad \text{(II -40)}$$

II - 7 The Calculation Procedure in Density Functional Theory

The resolution of the equations of KS is then done in an iterative manner using a self-consistent cycle of iterations illustrated by the flowchart of figure (I-1). we starts by injecting the density of initial charge ρ_{in} to diagonalize the

secular equation: $(H-\varepsilon_i S)C_i = 0$ the matrix of recovery). The overall charge density, which can be found by adding together all of the occupied orbitals, is then used to construct the new charge density ρ_{out} using the eigenvectors of the secular equation.

We combine the two charge densities, ρ_{in} and ρ_{out}, as follows if the computations disagree:

$$\rho_{in}^{i+1} = (1-\alpha)\rho_{in}^{i} + \alpha\,\rho_{out}^{i} \qquad \text{(II -41)}$$

i represents the i^{eme} iteration and α a mixing parameter. Thus the iterative procedure can be continued until convergence is achieved.

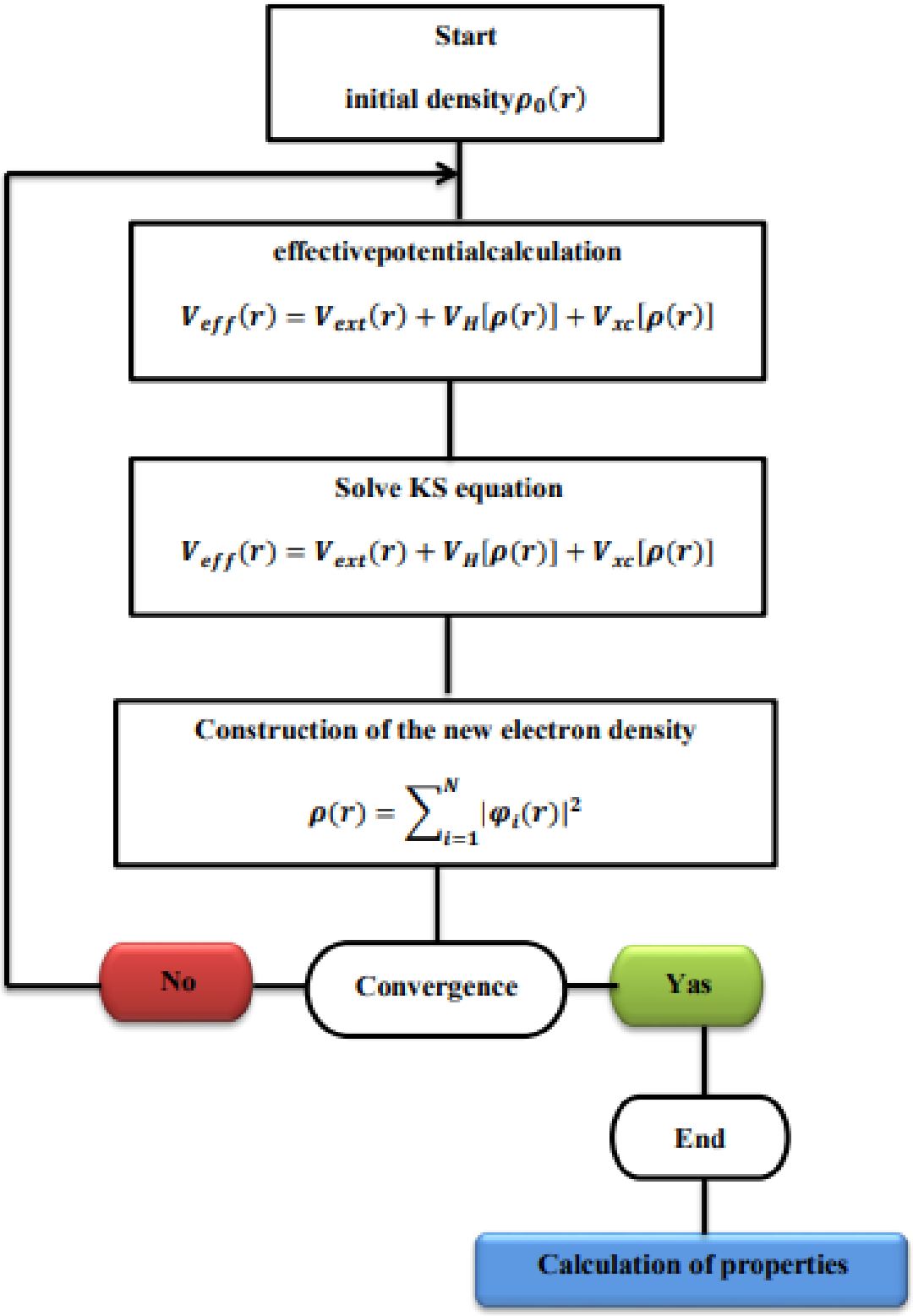

Figure II-1: diagram of self-consistent calculations of the density functional

II -8 The full-potential linearized augmented Plane Wave (FP-LAPW) Method

II -8-1 Introduction

One of the most difficult problems is the quantitative study in condensed matter physics, such as the determination of band structures, cohesive energy, charge density, ...ect . However, several methods have been formulated in order to calculate all the properties of the fundamental state, and precisely the structure of bands of certain materials (metal, semi-metal, semiconductor and insulator), either according to crystallinity and order (crystal or amorphous). However, these models fall under the classification of methods, which is subdivided into three groups :

- Empirical methods.
- Semi empirical methods.
- The methods of the first principle (ab- initio).
  - the method of pseudos potetiels (OPW)
  - the linear Muffin-Tin orbital method (LMTO)
  - the KKR method
  - the linear atomic orbital method (LCAO)
  - the linearized augmented plane wave method (LAPW) which will the object of our study

II-8-2 The augmented plane wave (APW) method

In 1937, Slater **[22]** developed the augmented plane wave (APW) technique **[19–21].** it is based on a principle where the potential is represented in a form called " muffin-tin " , this potential is spherically symmetrical .

The following factors need to be taken into mind while using this method: The potential and the wave function are smooth between atoms (interstitial area), but they differ significantly near the atomic nucleus and are comparable to those of an isolated atom. In this case, the crystal is considered as

a set of spherical atomic regions separated by empty spaces and therefore different bases are used **[23]** , a radial function, solution of the radial Schrödinger equation inside the sphere and plane waves in the interstitial region (see figure) :

$$\varphi(r) = \begin{cases} \frac{1}{\Omega^{1/2}} \sum_G C_G \, e^{i(G+K)r} & r \in I \\ \sum_{lm} A_{lm} U_l(r) Y_{lm}(r) & r \in S \end{cases} \qquad \text{(II-42)}$$

where $\varphi(r)$ is the wave function, Ω is the volume of the unit cell and $u_l(r)$ is the regular solution of the equation

$$\left\{ -\frac{d^2}{dr^2} + \frac{l(l+1)}{r^2} + V(r) - E_l \right\} r u_l(r) = 0 \qquad \text{(II-43)}$$

C_G and A_{lm} : the development coefficients.

E_l : a parameter.

V : the spherical component of the potential in the sphere.

The radial functions defined by (II.1) are automatically orthogonal to each state of the same Hamiltonian which disappears on the limit of the sphere **[24]** (Andersen 1975). This is translated from the Schrödinger equation :

$$(E_2 - E_1) r u_1 u_2 = u_2 \frac{d^2 r u_1}{dr^2} - u_1 \frac{d^2 r u_2}{dr^2} \qquad \text{(II-44)}$$

where u_1 and u_2 are the radial solutions at different energies E_1 and E_2 . The overlap is achieved by using this relation and integrating by parts; the surface terms disappear if u_1 or u_2 disappear on the limit while the other terms cancel each other out.

In the case of a constant potential, the work of Slater **[25,26]** shows that plane waves are the solutions of the Schrödinger equation . While the radial functions are the solutions in the case of a spherical potential, therefore E_l is equal to the eigenvalue. However, this approximation made on the potential is often

reasonable; indeed the muffin-tin approximation (MT) is widely used in codes (APW). The approximation (MT) gives surprising results for compact structures (fcc and hcp).

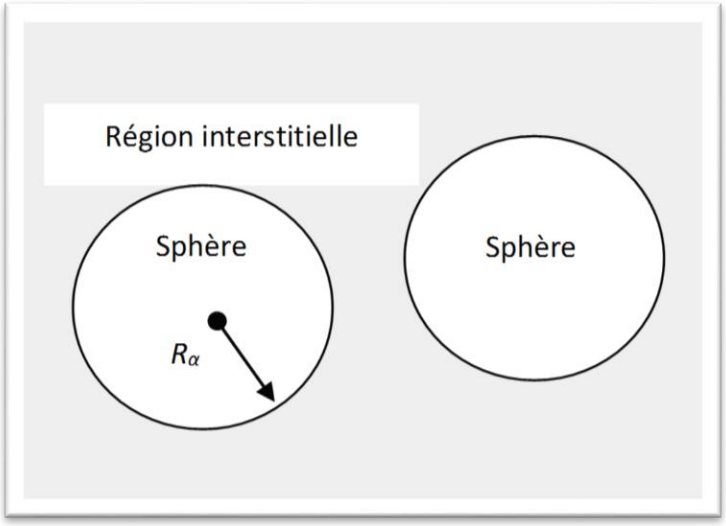

Figure II-2 Construction of the different crystals in the APW method

This method encounters a problem is that the expression (II .1) does not ensure the continuity of the kinetic energy at the limits of the sphere, so it is necessary to eliminate this constraint. In the (APW) method this can be achieved by defining the A_{lm} in terms of C_G through the expansion of the spherical harmonics of the plane waves. The coefficient of each component (lm) is related to the limit of the sphere by :

$$A_{lm} = \frac{4\pi i^l}{OMEGA^{12} u_l(R)} \sum_G C_G J_l(|k+g|R) Y_{lm}(k+G) \qquad \text{(II-45)}$$

where the origin is taken at the center of the sphere.

R : is the radius of the sphere.

The A_{lm} are determined by the coefficients of the plane waves $\boldsymbol{C}_G$ and the energy parameters E_l, which are variational coefficients in the (APW) method. The functions which are undecided by G and which have both forms : in the interstitial region behaves like plane waves and in the region of the sphere are increased by the radial functions are called augmented plane waves or (APWs).

II-8-3 Principle of the LAPW method

In 1975, Anderson **[27]** proposed the linearized augmented plane wave (LAPW) method **[28,29]** . Is an improvement of Slater's APW method, constitutes one of the most precise bases for the calculation of crystalline solids.

In the Linearized Augmented Plane Wave (LAPW) method, the basis functions inside the Muffin-Tin sphere are a linear combination of the radial functions $U_l(r)$ and $Y_{lm}(r)$ their derivatives by With respect to the energy $U_l(r)$ $Y_{lm}(r)$ **[30]**, the functions U_l are determined as in the APW method, and the function $U_l(r)$ $Y_{lm}(r)$ must satisfy the following condition:

$$\left(-\frac{d^2}{dr^2}+\frac{\iota(\iota+1)}{r^2}+v(r)-E_\iota\right)rU_\iota(r)=\ rU_\iota(r) \qquad \text{(II -46)}$$

The radial functions and their derivatives guarantee continuity with the external plane waves on the MT sphere's surface in the non-relativistic scenario. Consequently, the basis functions (LAPW) of the FP-LAPW approach are the augmented wave functions::

$$\Psi^{(r)}=\begin{cases}\frac{1}{\Omega^{\frac{1}{2}}}\Sigma_G C_G e^{i(G+K)r} & r>R_\alpha\\ \Sigma_{\imath m}\left(A_{\imath m}U_\iota(r)+B_{\imath m}\dot{U}_\iota(r)\right)Y_{\iota m}(r) & r<R_\alpha\end{cases} \qquad \text{(II -47)}$$

B_{lm}: are coefficients that correspond to the function $U_l(r)$.

If we want to make a comparison between the two methods APW and LAPW we can mention the following points:

- The energy of the bands at point k in the LAPW method is obtained with a single diagonal while in the APW method it is necessary to calculate the energy for each band.

- In the APW method, the asymptote problem is solved by the addition of the derivative of the radial function which ensures that plane waves do not multiply with the radial functions.

II-8-4 Full potential linearized augmented plane wave (FPLAPW) method

The form of the potential and the charge density are not approximated in the Full Potential Linearized Augmented Plane Waves (FP-LAPW) approach **[31].** They are preferably developed in lattice harmonics inside each atomic sphere, and in Fourrier series in the interstitial regions. Therefore, it guarantees the continuity of the potential on the surface of the MT sphere and develops it in the following form:

$$V(r) = \begin{cases} \Sigma_{lm} V_{lm}(r)\, Y_{lm}(r) & \text{inside the sphere} \\ \Sigma_K V_K e^{ikr} & \text{outside the sphere} \end{cases} \quad \text{(II -48)}$$

Similarly, the charge density can be derived as follows:

$$\rho(r) = \begin{cases} \Sigma_K \rho_K e^{ikr} & r > R_\alpha \\ \Sigma_{lm} \rho_{lm}(r) Y_{lm}(r) & r < R_\alpha \end{cases} \quad \text{(II -49)}$$

With this procedure, the calculations lose precision, compared to the APW method which reproduces. However, a fundamental problem of FP-LAPW is the treatment of intermediate states between valence states and core states, called half-core states. Where There are two ways to solve this problem:

a. The use of multiple energy windows.

b. The use of local orbital development.

II-8-5 Multiple energy windows

The most widely used technique for treating the half-core state problem is that of dividing the energy spectrum into windows, each of which corresponds to an energy E_l **[32]**. This processing procedure is illustrated in Fig. II-3.

In this window processing, a separation is made between the valence state and the half-core state where a set of E_l is chosen for each window to process the corresponding states. This amounts to carrying out two calculations using the LAPW method, independent, but always with the same potential. The FP-LAPW method is based on the fact that the functions $U_l(r)$ and $\dot{U}_l(r)$ are orthogonal to any eigenstate of the core and, in particular, to those located on the surface of the

sphere. However, half-core states often satisfy this condition, unless there are the presence of "fantomes " bands between the half-core and valence states.

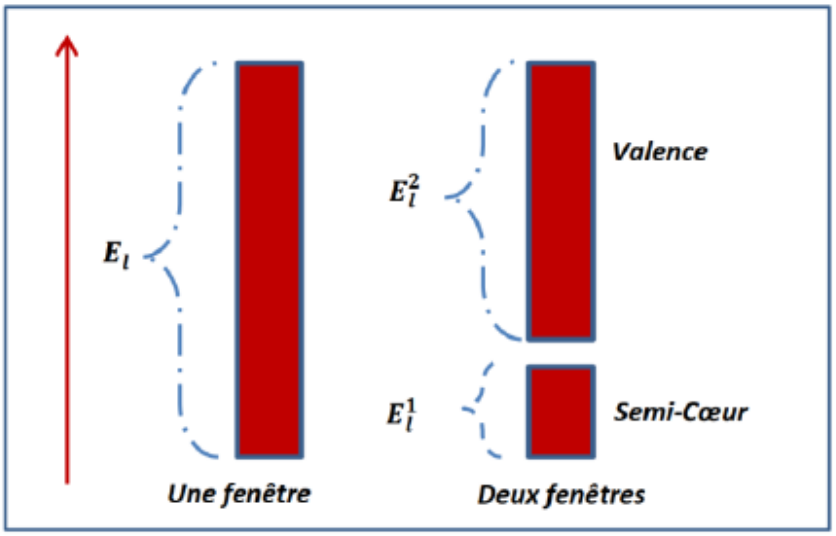

Figure II-3: Example of windows with a half-core state

Using a third category of basis functions, the technique (LAPW) in local orbitals is developed by altering the orbitals of its base to prevent the usage of multiple windows. Singh (1991) **[33]** presented the idea of treating all the bands from a single energy window. These orbitals, designated "LO," were provided as a linear combination of two radial functions that represented two distinct energies, together with the derivative of one of these functions with respect to energy::

$$\varphi = \begin{cases} 0 & r > R_\alpha \\ \left[\left(A_{lm}(r, E_l) + B_{lm}\dot{U}_l(r, E_l)\right) + C_{lm}(r, E_{LO})\right]Y_{lm}(r) & r < R_\alpha \end{cases} \quad \text{(II -50)}$$

This adjustment lowers the inaccuracy in the conduction and valence band calculations when the coefficients are the same type.

II-9 Wien2K code

The Wien2K Code is the implementation of the FP-LAPW method this code allows to calculate the structural, electronic, optical, elastic and magnetic properties it also allows the calculation of the total energy of a periodic crystal using the lattice of Bravais and space group symmetry given .

It is made up of several independent programs which are linked by the C-SHELL SCRIPT. The use of the different programs is illustrated in figure (II-4). Initialization consists of running a series of small programs that interfere with :

NN : A program which checks the non-overlapping spheres.

LSTART : A program that generates atomic densities and determines how different orbitals are treated in calculating band structure, such as core states with or without local orbitals.

SYMMETRY : It produces LM expansion for lattice harmonics, identifies the point group of specific atomic sites, creates space group symmetry operations, and determines local rotation matrices.

KGEN : It generates a k mesh in the Brillouin zone.

DSTART : It generates a starting density for the SCF cycle by the superposition of the atomic densities generated in **LSTART** .

Then a consistent self cycle is initialized and repeated until the convergence criterion is verified.

This cycle is part of the following stages :

LAPW0 : Generates the potential from a density calculated by DSTART.

LAPW1 : Calculates valence bands, eigenvalues and eigenvectors.

LAPW2 : Calculates the valence densities for the eigenvectors.

LCORE : Calculates heart states and densities.

MIX : Mix the densities of inputs and outputs.

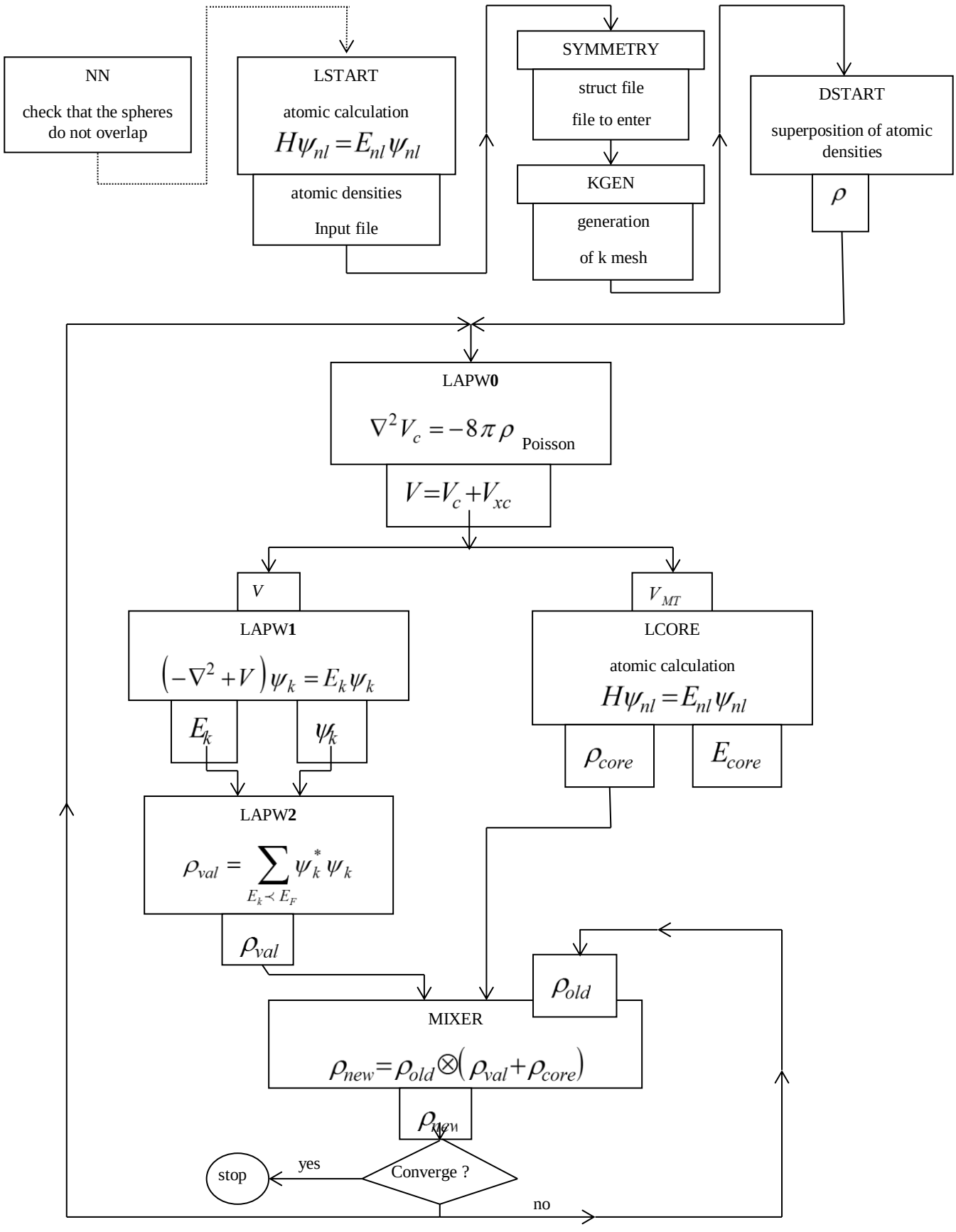

Figure II-4 : le C-SHELL SCRIPT of Wien2k code

II-9-1 Determination of properties

Once the self-consistent calculation of the "SCF cycle" is completed, several properties can be determined, including: structural, magnetic, band structure, density of states, charge density and elastic and thermodynamic properties...etc.

II-9-1-1 Structural properties

The parameters obtained by the study of structural properties are, the lattice parameter obtained by the fit of the Murnaghan equation , the compressibility modulus B and its derivative B' which indicate the mechanical aspect of the material (hardness, resilience, etc ...)

II-9-1-2 Electronic properties

The study of electronic properties can be done on three aspects :

a. Band structure

to through which one can schematize two distinct parts of the test compound, the first is the portion below the Fermi level i.e. the valence band, while the second is the part above the Fermi level i.e. the conduction band .

b. Density of states (DOS)

The DOS plot gives us the state charge density and its contribution to the total density along the energy levels (valence band and conduction band).

c. charge density

Through the charge density plot, we can see the concentration of charges around the atoms as well as the charge transfer between different electronegativity atoms, however, the charge density can give us important indications regarding the nature of the atoms. bonds which govern the atoms constituting the compound to be studied (covalent bonds, ionic, or metallic bonds)

II-9-1-3 Optical properties

The calculation of the imaginary and real part $\boldsymbol{\varepsilon_2(\omega)}$ and $\boldsymbol{\varepsilon_1(\omega)}$ the function of iélectrique allows us to determine the different possible optical transitions for a given compound.

II - 10 Conclusion

In this chapter we have described the different theoretical approaches for solving the Schrödinger equation called ab-initio methods based on DFT. In our study, we were interested in an ab-initio study based on the formalism of density functional theory (DFT) requiring a certain number of approximations such as the generalized gradient approximation (GGA) and that of Becke and Johnson modified (mBJ). We will have access to the physical properties of the system studied, namely the structural, electronic, magnetic, optical and mechanical properties. A detailed theoretical study will be proposed to these properties in the following chapter.

References :

[01] Thomas, Llewellyn H. Vol. 23. No. 5. Cambridge University Press, 1927.

[02] Fermi, Enrico. *Rend. Accad. Naz. Lincei* 6.602-607 (1927): 5.

[03] Kohn, Walter, and Lu Jeu Sham. *Physical review* 140.4A (1965): A1133.

[04] Menzer, Fares, and Bachir Zouchoune. (2013).

[05] Lardjane, S. (2013). (Doctoral dissertation, Belfort-Montbéliard).

[06] M. Born, J. R. Oppenheimer, Ann. Phys. 87, 457 (1927).

[07] D. R. Hartree, Proc. Combridge Philos. Soc. 24, 89 (1928).

[08] V.Fock, Z.Phys.61, 126(1930); 62,795(1930).

[09] P. Hohenberg, W. Kohn. "Inhomogeneous Electron Gas". Phys. Rev., 136, pp B864–B870, 1964.

[10] W. Kohn, L.J. Sham. "Self-consistent Equations Including Exchange and Correlation Effects ". Phys. Rev., 140, pp A1133–A1138, 1965.

[11] J. P. Perdew and Y. Wang, Phys. Rev. B 45, 13244 (1992).

[12] J.P.Perdew, K.Burke and M.Ernzerhof, Phys. Rev. Lett.77,3865(1996).

[13] J.P.Perdew,Y.Wang,in Electronic Strucrure of Solids 91,ed P.Ziesche,H.AcademicVerlag .Berlin,1991.B 11.

[14] A. I. Liechtenstein, V. I. Anisimov and J. Zaanen, Phys. Rev. B 52, 5467–5470, (1995).

[15] V. I. Anisimov and O. Gunnarsson, Phys. Rev. B 43, 7570–7574, (1991).

[16] F. Tran and P. Blaha, Phys. Rev, *102*(22), p. 226401, 2009.

[17] A. D. Becke and E. Johnson, *The Journal of chemical physics*, *124*(22), p. 221101, 2006.

[18] A. Becke and A. Roussel, Phys. Rev *A*, *39*(8), p. 3761, 1989.

[19] T. L. Loucks, The Augmented-Plane-Wave Method (Benjamin, New York(1967).

[20] Im Tsidilkovski, Band structure of semi-conductors, 19, 35 (1982).

[21] D. Singh, Planes waves, pseudopotentiels and the LAPW method (1994)

[22] P. Hohenberg and W. Kohn, Phys. Rev. B **136**, 864 (1964).

[23] J. P. Perdew and Y. Wang, Phys. Rev, B **45**, 13244 (1992).

[24] J. P. Perdew, S. Burke and M. Ernzerhof, Phys. Lett. **77**, 3865 (1996).

[25] J. P. Perdew and A. Zunger, Phys. Rev. B **23**, 5048 (1981).

[26] L. Hedin and B. I. Lundqvist, J. Phys. C**4**, 2064 (1971).

[27] O. Andersen, Phys. Rev *B*, *12*(8), p. 3060, 1975.

[28] G. Kresse, J. Hafner, and R. Needs, J. Phys, *4*(36), p. 7451, 1992.

[29] T. Takeda and J. Kubler, "J. Phys. F: Met. Phys," 1979.

[30] W. BENSTAALI, "etude des proprietes optoelectroniques et magnetiques des composes znx/cdx dopes par des metaux de transition," Thèse de doctorat. Université de Mostaganem-Abdelhamid Ibn Badis, 2014.

[31] D. Hamann, Phys. Rev, *42*(10), p. 662, 1979.

[32] R. Gaspar, *Acta Physica Academiae Scientiarum Hungaricae*, *3*(3), pp. 263-286, 1954.

[33] D. Singh , Phys. Rev *B*, *43*(8), p. 6388, 1991.

Results and Discussions

Chapter III :

The simple perovskite ABO_3 (A=Sr, Ba and B=V, Ru)

III-1 Introduction

The current work's objective is to give as much information as possible while doing a complementary and comparative analysis of the previously conducted experimental work. In this chapter we will study the simple perovskite ABO_3 (A = Sr, Ba and B = V, Ru).

The choice of these perovskite materials was made thanks to their great technological importance, particularly in the optical, electronic and magnetic fields. And on the other hand, There aren't many theoretical research on the physical characteristics of these materials.

We used the generalized gradient approximation (GGA) in the context of (WC: Wu-Cohen) **[2,3]** as exchange and correlation functionals, based on the FP-LAPW approach used in the Wien2k code **[1].** Thus, we computed the band structures and the electronic density of states diagrams using the modified Beck-Johnson exchange potential (mBJ: Modified Beck-Johnson) **[4,5].**

III-2 Calculation details

According to the LAPW approach, the space is separated into interstitial regions and non-overlapping Muffin-Tin spheres. Within the interstitial region, the basis functions, electron concentrations, and potentials are extended in Fourier series, and surrounding the atomic sites, in spherical harmonics with a cutoff radius $lmax$ = 10.

In this interstitial region, the plane wave functions are limited to Rmt . Kmax = 8 where Rmt denotes the smallest radius of the atomic sphere and Kmax is the maximum value of the largest vector K in the plane wave expansion to obtain the convergence of the eigenvalues. For the integration a mesh of (13×13×13) k-points in the first Brillouin zone was used. Self-consistent calculations are considered convergent when the total crystal energy converges to 10^{-6} Ry. Table III-1 groups the valence states and Muffin-Tin radii used in our analysis.

Table III-1: The values of R_{MT} and electronic configuration for each element used during our calculations.

	atom	**ABO_3**	**Electronic configuration**
R_{MT} (a.u)	Sr	2.42	[Kr]$5s^2$
	Ba	2.42	[Xe]$6s^2$
	V	1.8	[Ar] $3d^3 4s^2$
	Ru	1.8	[Kr] $4d^7 5s^1$
	O	1.63	[He]$2s^2 2p^4$

III-3 The simple perovskite ABO_3 (A = Sr, Ba and B = V, Ru)

For many years, transition metal oxides (TMOs) have been the subject of intensive theoretical and experimental investigation. The d-band TMOs are of special interest because of their remarkable catalytic capabilities. These compounds form a large and intricate class that is still not completely understood. Of the many structural variations found in ABO_3 oxides, the perovskite structure is perhaps the most recognized and thoroughly investigated. Perovskites like $SrXO_3$ **[6–8]** and $BaXO_3$ **[9–11]** have attracted considerable interest from physicists and materials scientists because of their distinctive transport, electronic, and magnetic properties. Nevertheless, the electronic structure of these complex systems remains incompletely understood, with efforts to interpret their behavior under different conditions often depending on simplified models.

The ABO_3 (A = Sr, Ba and B = V, Ru) perovskite is a simple cubic and belongs to the space group $Pm\bar{3}m$ (No: 221) Figure III-1. Table III-2 gives the atomic positions of the cubic structure of ABO_3.

Table III-2 : Atomic Positions in a Simple Cubic Oxide Perovskite Crystal of ABO_3.

atom	Wyckoff	x	Y	z
A (Sr, Ba)	(2a)	0	0	0
B (V, Ru)	(2a)	0.5	0.5	0.5
O	(6b)	0.5	0	0.5
		0	0.5	0.5
		0.5	0.5	0

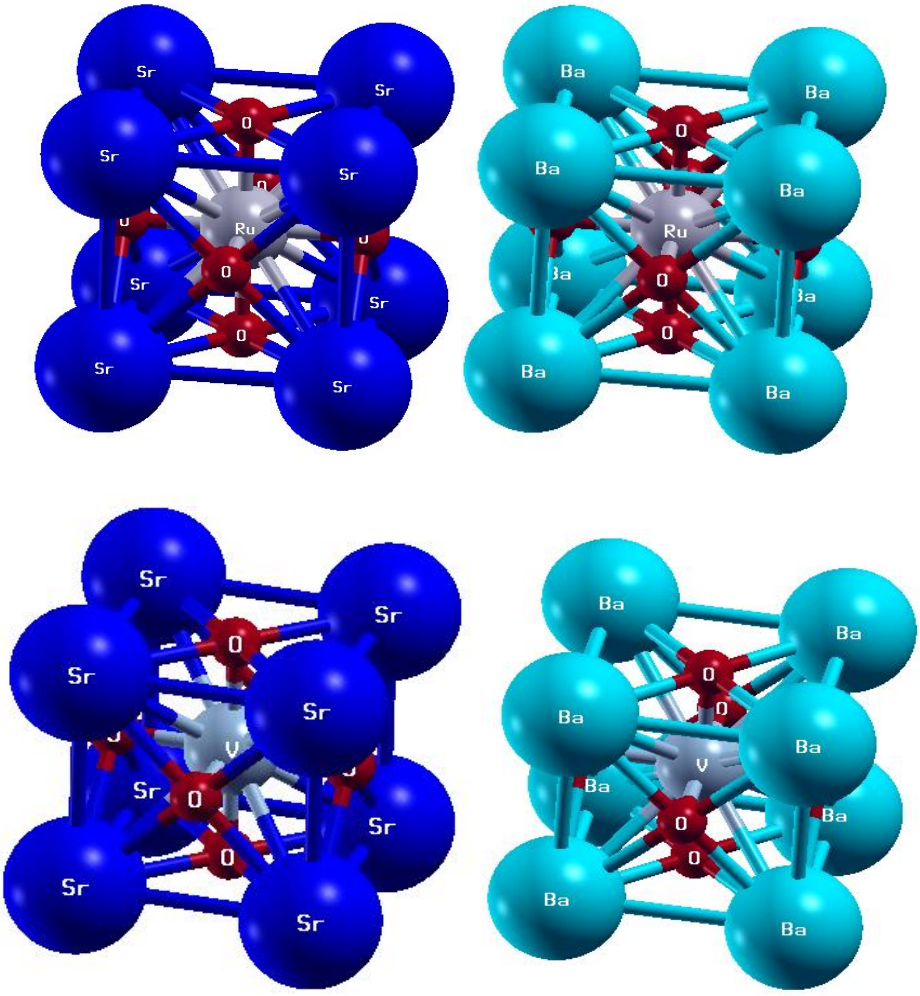

Figure III-1: $SrVO_3$, $SrRuO_3$, $BaVO_3$ and $BaRuO_3$ Perovskite Structures in Cubic Simple Form (Pm3m).

The reciprocal lattice associated with the ideal perovskite structure is simple cubic. Its unit cell which corresponds to the first Brillouin zone is shown in Figure III-2. The

high symmetry points are: G: π/a (0.0.0), X: π/a (1.0.0), M: π/a (1.1.0) and R: π/a (1.1.1) [12].

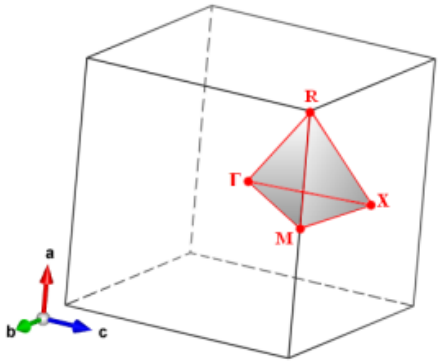

Figure III-2: The first Brillouin zone of a simple cubic lattice.

III-3-1 Structural properties:

An optimized structure corresponds to a minimum energy, with relaxed atoms i.e. to reach this structure, one must calculate the variation of the energy as a function of the volume of the cell. We have performed a structural optimization on ABO_3 alloys (A = Sr, Ba and B = V, Ru) for two states at a time, the non-magnetic state (NM) and the ferrimagnetic state (FM). It is worth noting that the equilibrium lattice parameters are determined by calculating the total energy as a function of volume, using the Murnaghan equation [13] expressed as:

$$E_T(V) = E_0 + \left(\frac{BV}{B\prime}\right)\left[\left(\frac{V_0/V}{B'-1}\right)^{B\prime} + 1\right] \qquad \textbf{(III-1)}$$

Where $V0,0$ are the equilibrium volume and energy respectively.

$$B = V_0 \frac{d^2E}{dV^2}\Big|_{V=V_0'} \qquad \textbf{(III-2)}$$

B is the equilibrium compressibility modulus, and its first derivative $B'$with respect to pressure.

Figure (III-3) presents the total energies for both ferrimagnetic and nonmagnetic orders as a function of volume obtained by the GGA-WC approximation for ABO_3 alloys . It appeared that, for all the compounds studied, The energy of the FM state is lower than that of the NM state. Then, in the ferromagnetic order, the alloys under study are more stable.

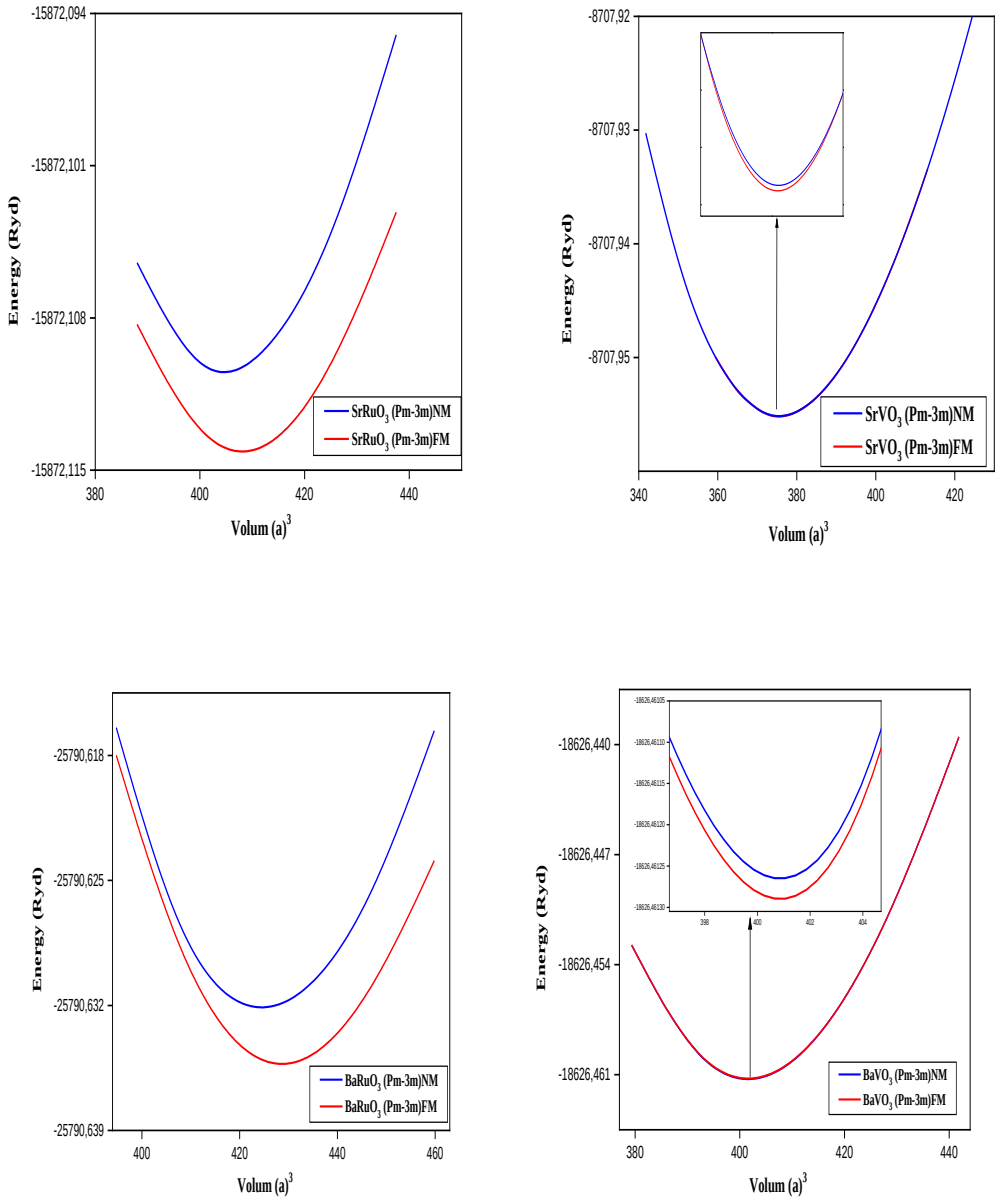

Figure III-3: Representation of total energy as a function of volume for ferrimagnetic (FM) and non-magnetic (NM) states for ABO_3 alloys (A = Sr, Ba and B = V, Ru).

The calculated results are compared with experimentally published data for ABO_3, as detailed in Table III-3. Table 3 makes it clear that the outcomes show a respectable level of agreement with both experimental and theoretical data. Typical for approaches that use the Generalized Gradient Approximation (GGA), the estimated lattice parameter a_0 for ABO_3 differs from experimental values by no more than 0.4–0.5%. The data reveal that the lattice parameter a_0 for the cubic ABO_3 compounds (A = Sr, Ba and B = V, Ru) increases in the following order:

a_0 ($SrVO_3$) < a_0 ($SrRuO_3$) and a_0 ($BaVO_3$) < a_0 ($BaRuO_3$)

This trend can be attributed to the ionic radii (R) of the B atoms, with R values as follows: R(V) = 0.58 Å < R(Ru) = 0.62 Å

as well a_0 ($SrBO_3$) < a_0 ($BaBO_3$) because of the ionic radii of the A atoms (R(Sr) = 1.26 Å < R(Ba) = 1.42 Å)

Additionally, the compound under study appears to be thermodynamically stable and perhaps synthesizable based on its negative formation energy. In table III-2 show that

ΔHf ($SrVO_3$) < ΔHf ($BaVO_3$) < ΔHf ($SrRuO_3$) < ΔHf ($BaRuO_3$). Hence, $SrVO_3$ is the most stable.

The calculated bulk modulus of the studied compounds decreases in the following order : B ($SrVO_3$) > B ($BaVO_3$) > B ($SrRuO_3$) > B ($BaRuO_3$). which indicates that $SrVO_3$ exhibits greater hardness and lower compressibility compared to other compounds.

Two crucial elements for figuring out the structural properties of basic ABO_3 perovskites are the tolerance factor (t) and the octahedral factor (μ). These elements provide important information on the formability and stability of perovskite structures. The following equations [21] are used in this work to define the tolerance and octahedral factors in terms of ionic radii:

$$t = \frac{r_A + r_O}{\sqrt{2}(r_B + r_O)} \quad \textbf{(III-3)}$$

$$\mu = \frac{r_B}{r_X} \quad \textbf{(III-4)}$$

The ionic radii, as referenced from Shannon's table [22], are as follows:

r (Sr^{2+}) = 1.26 Å, r(Ba^{2+}) = 1.42 Å, r (V^{4+}) = 0.58 Å, r (Ru^{4+}) = 0.62 Å and r (O^{2-}) = 1.35 Å.

Table III-2 displays the findings for the octahedral factor (μ) and the tolerance factor (t). For stable perovskite compounds, the tolerance factor (t) usually falls between 0.75 and 1.05 [23, 24], and the octahedral factor (r_B/r_O) must be at least 0.425 [25] in order for perovskite to form. The stability criteria are in agreement with our results for (t) and (μ) in Table III-3.

Table III-3 : presents the calculated equilibrium cell volume V(Bohr^3), lattice parameter a (Å), bulk modulus B (GPa), first derivative of the bulk modulus B′(in GPa), equilibrium energy Etot (Ry), formation enthalpy ΔHf (eV/mol), tolerance factor (t), and octahedral factor (μ) for $SrVO_3$, $BaVO_3$, $BaRuO_3$, $SrRuO_3$.

……	Space groupe	state	aExp (Å)	V(Bohr3)	a (Å)	B'	B (GPa)	Etot	ΔHf	t	μ
$SrVO_3$	**Pm3m (n.221)**	**FM**	3.841 [15]	375.822	3.818	4.616	204.363	-8707.967359	-2.607	0.956	0.429
	Pm3m (n.221)	**NM**		375.813	3.818	4.875	202.407	-8707.967351			
	Other works		-	376.4758 [10]	3.866[15] 3.8662[17] 3.8662[18] 3.8269 [10]	-	181.5[15] 181.53[18] 182.8[18]	-	-	-	-
$SrRuO_3$	**Pm3m (n.221)**	**FM**	3.94 [16]	407.674	3.923	4.724	184.040	-15872.114926	-2.232	0.936	0.459
	Pm3m (n.221)	**NM**		404.519	3.913	4.947	197.436	-15872.110415			
	Other works		-	-	3.923[19] 3.94[16] 3.95[20]	-	-	-	-	-	-
$BaVO_3$	**Pm3m (n.221)**	**FM**	3.9428 [10]	401.2528	3.9031	4.685	201.9131	-18626.462185	-2.580	1.014	0.429
	Pm3m (n.221)	**NM**		401.2754	3.9031	4.978	201.4161	-18626.462164			
	Other works			401.2258 [10]	3.9090[10] 3.967[11]	-	173.210 162.511	-18625.593 [11]	-	0.999 [11]	-
$BaRuO_3$	**Pm3m (n.221)**	**FM**	4.006 [14]	428.1979	3.9886	4.582	174.3950	-25790.636049	-2.228	0.994	0.459
	Pm3m (n.221)	**NM**		424.7848	3.9779	4.849	185.9694	-25790.632154			
	Other works			-	4.0059[9]	-	-	-	-	-	-

III-3-2 Elastic Constants and Mechanical Properties

The properties of materials are profoundly influenced by their stress states and the associated global or local deformations of the crystal lattice, which are inherently interconnected.

Any deformation alters the relative positions of atoms, which in turn influences the overlap between their atomic orbitals

To assess the stability of the compounds under study, their elastic properties were evaluated. The study of elastic properties presents several interests because they relate to the various fundamental properties of the solid state such as: They provide us with information on the rigidity, anisotropy of materials, thermal expansion, Debye temperature, melting point.

In this investigation, we calculated the elastic constants (C_{ij}) of ABO_3 compounds (A = Sr, Ba and B = V, Ru) using Thomas Charpin's theoretical model [26], which was implemented in the WIEN2k code. Therefore, we identify three distinct components in cubic systems: C_{11}, C_{12}, and C_{44}. To calculate the latter, one must understand the energy curve as a function of the elementary mesh's deformation. The values of these constants elastic is obtained by the GGA-WC approximation the calculation results are presented in Table III-4.

By satisfying the following requirements, the material's structure's mechanical stability is verified **[27]:**

$$C_{11} - C_{12} > 0,\ C_{11} > 0, C_{44} > 0, (C_{11} + 2C_{12}) > 0\ and\ C_{12} < B < C_{11} \qquad \textbf{(III-5)}$$

The materials are mechanically stable because, as Table III-4 shows, all five of the requirements listed in Equation (5) are satisfied at the same time. This table illustrates that the results are consistent with the related results of the experiment. It is observed that the unidirectional elastic constant C_{11}, associated with compression along the principal crystallographic axes, is slightly more than three times greater than C_{44}, suggesting that the material offers greater resistance to unidirectional compression than

to shear deformation. And the high value of the elastic constant C_{11} reflects the strong O-B bond along the principal directions <100>.

A linear combination of C_{11} and C_{12} may be used to represent this system's bulk modulus B: **[28, 29]:**

$$B = \frac{C_{11}+2C_{12}}{3} > 0 \quad \textbf{(III-6)}$$

The following formula is used to get the shear modulus G, Voigt shear modulus G_V, and Reuss shear modulus G_R **[28–30]:**

$$G_V = \frac{C_{11}-C_{12}+3C_{44}}{5} \quad \textbf{(III-7)}$$

$$G_R = \frac{5C_{44}(C_{11}-C_{12})}{4C_{44}+3(C_{11}-C_{12})} \quad \textbf{(III-8)}$$

$$G_H = G = \frac{1}{2}(G_V + G_R) \quad \textbf{(III-9)}$$

Young's modulus E, the anisotropic parameter A, the B/G ratio, Poisson's ratio ν, and Vickers hardness H_V are determined using the following relations **[31–33]:**

$$E = \frac{9BG}{3B+G} \quad \textbf{(III-10)}$$

$$v = \frac{1}{2}\left[\frac{3B-2G}{3B+G}\right] \quad \textbf{(III-11)}$$

$$H_V = 2(k^2G)^{0.585} - 3; \left(k = \frac{G}{B}\right) \quad \textbf{(III-12)}$$

$$A = \frac{2C_{44}}{(C_{11}-C_{12})} \quad \textbf{(III-13)}$$

The findings for the bulk modulus B, shear modulus G, Voigt shear modulus G_V, Reuss shear modulus G_R, Young's modulus E, anisotropic parameter A, B/G ratio, Poisson's ratio v, and Vickers hardness H_V for ABO_3 compounds (A = Sr, Ba and B = V, Ru) are shown in Table III-4. The results also include the elastic constants C_{11}, C_{12}, and C_{44}. According to our findings, the bulk modulus (B), which is obtained from the elastic constants (C_{ij}), satisfies the requirement that C_{12} < B < C_{11} for both compounds. Furthermore, the computed bulk modulus, obtained through both the elastic constants

(C_{ij}) and total energy minimization methods, shows a comparable value, as presented in Tables III-3 and III-4. This similarity may serve as an indicator of the validity and accuracy of this theoretical approach to determining the elastic constants.

The bulk modulus of cubic ABO_3 decreases in the following order: B($SrVO_3$) > B($SrRuO_3$) and B($BaVO_3$) > B($BaRuO_3$) , which is the reverse of (a_0 (SrVO3) < a_0 (SrRuO3) and a_0 (BaVO3) < a_0 (BaRuO3)) and aligns with the established relationship between the bulk modulus (B) and lattice constants (cell volume V_0), expressed as $B_0 = kV_0^{-1}$ **[34].** This general trend, where a larger lattice constant corresponds to a smaller bulk modulus, has also been observed in other perovskites (ABO_3) **[35].**

The anisotropy factor (A) is equal to 1.0 for an isotropic material, whereas any number less or above 1.0 denotes anisotropy. Elastic anisotropy is present in this compound as, as Table 4 illustrates, the anisotropy factor (A) for ABO_3 is greater than 1.0.

A common criterion for determining a material's brittleness or ductility is Pugh's B/G ratio. By this criterion, materials are categorized as ductile if their B/G ratio is greater than 1.75 and as brittle if it is less than 1.75. Based on the calculated B/G ratios, the alloys $SrVO_3$ (1.637) and $SrRuO_3$ (1.664), exhibit brittle behavior, as their ratios are below the 1.75 threshold, while $BaVO_3$ (1.731) and $BaRuO_3$ (1.868) show signs of ductility, because it has a ratio greater than 1.75. Moreover, the B/G ratio serves as an indicator of material hardness, where lower values generally reflect higher hardness. Consequently, it can be inferred that the $SrVO_3$ alloy is likely harder than $SrRuO_3$ then $BaVO_3$ then $BaRuO_3$. According to Petitfort **[36],** brittleness is indicated by a negative Cauchy pressure (C_{12}-C_{44}), whereas ductility is indicated by a positive value. While compounds $BaVO_3$ and $BaRuO_3$ correspond to positive Cauchy pressure values, proving the compounds' ductility, compounds $SrVO_3$ and $SrRuO_3$ observed results correspond to a negative Cauchy pressure value (C_{12}-C_{44}), verifying our compound's brittleness.

Stiffness is measured by a material's Young's modulus (E), where higher E values correspond to a greater stiffness. Based on the calculated Young's modulus values for

these materials, the order of stiffness is ($BaVO_3$ > $SrVO_3$ > $SrRuO_3$ > $BaRuO_3$). This demonstrates that the stiffness increases from $BaRuO_3$ to $BaVO_3$.

Poisson's ratio (v) reflects both the compressibility of a material and offers valuable information about the characteristics of its bonding forces **[37].** Materials are more stable against external deterioration and have lower compressibility when their Poisson's ratio is between 0.25 and 0.5 **[38].** Materials outside of this range, on the other hand, are often far more compressible. As shown in Table III, the ABO_3 compounds (A = Sr, Ba and B = V, Ru) demonstrate lower compressibility, as their Poisson's ratios fall within this stable range. Furthermore, Poisson's ratio provides useful details on the bonding forces present in a material. For example, ionic materials often have Poisson's ratios of 0.25, whereas covalent materials typically have ratios of 0.1 **[39].** Based on the Poisson's ratios listed in Table 4 (0.246, 0.249, 0.257 and 0.272), these alloys exhibit ionic character. This observation is further supported by the data presented in Table III-4.

For covalent and ionic materials, the typical relationships between bulk modulus (B) and shear modulus (G) are approximately $G \approx 1.1B$ for covalent materials and $G \approx 0.6B$ for ionic materials **[17].** In our study, the calculated values of G_{VRH}/B_{VRH} are 0.61, 0.60, 0.58 and 0.54 for $SrVO_3$, $SrRuO_3$, $BaVO_3$ and $BaRuO_3$ respectively suggesting that ionic bonding is more prevalent in these materials.

A material's other mechanical characteristics are directly related to its Vickers hardness (HV). The capacity of a material to resist corrosion, perforations, cuts, and scratches is known as its hardness. A material is considered soft if its hardness is less than 10 GPa. Materials are categorized as hard if their hardness values fall between 10 and 40 GPa, and as extremely hard if they surpass 40 GPa. **[40].** Since the Vickers hardness values of the alloys studied in this work are higher than the critical threshold of 10 GPa, they may be categorized as hard materials based on the computed hardness values. $SrVO_3$ is the alloy with the greatest hardness among those examined.

Table III-4: The elastic constants C_{11}, C_{12}, C_{44}, bulk modulus B, the shear modulus (G, G_V and G_R), Young's modulus E (GPa), anisotropic parameter A, B/G ratio, Poison's ratio ν and Vickers hardness H_V for $SrVO_3$, $BaVO_3$, $BaRuO_3$, $SrRuO_3$.

This Work	C_{11}	C_{12}	C_{44}	B	G_V	G_R	G	E	A	B/G	ν	H_v
$SrVO_3$	352.100	111.224	114.681	191.515	116.983	116.916	116.949	291.509	0.952	1.637	0.246	15.204
$SrRuO_3$	360.068	92.983	95.628	182.011	110.793	107.879	109.336	273.286	0.71	1.664	0.249	14.169
$BaVO_3$	324.0123	140.3973	136.4786	201.601	118.610	114.243	116.426	292.895	1,486	1,731	0.257	14,009
$BaRuO_3$	304.9010	107.6903	89.1084	173.426	92.907	92.678	92.792	236.242	0,903	1,868	0.272	10,622

III-3-2-a Isotropic acoustic wave velocities and Debye temperature

One significant factor that affects the thermodynamic characteristics of materials is the Debye temperature θ_D. The solid's atoms progressively vibrate up to this temperature when the temperature rises above absolute zero. The temperature at which vibrations attain their greatest potential modes is represented by this.

As a result of its correlation with several physical constants, including specific heat, thermal expansion, and elastic constants, it may be expressed as [41]:

$$\theta_D = \frac{h}{k}\left[\frac{3n}{4\pi}\left(\frac{N_A\rho}{M}\right)\right]^{1/3} v_m \qquad \textbf{(III-14)}$$

Where *M* is the mass per unit cell, k is Boltzmann's constant, *h* is Planck's constant, N_A is Avogadro's number, n shows the number of atoms per formula unit, and ρstands for density. The following formula makes it easy to calculate the average sound velocity v_m **[41]:**

$$v_m = \left[\frac{1}{3}\left(\frac{2}{v_t^3} + \frac{1}{v_l^3}\right)\right]^{\frac{-1}{3}} \qquad \textbf{(III-15)}$$

In the context of Navier's equation **[42],** where $v_t$denotes the transverse velocity and $v_l$represents the longitudinal velocity, these quantities are derived as follows:

$$v_l = \sqrt{\frac{G}{\rho}} \qquad \textbf{(III-16)}$$

$$v_t = \sqrt{\frac{3B+4G}{3\rho}} \quad \textbf{(III-17)}$$

Where v_t is the transverse velocity and v_l is the longitudinal velocity.
The values of the Debye temperature θ_D and wave velocities for our compounds are shown in Table III-5. To our knowledge, there are no experimental or theoretical data in the literature to compare them with our results. Therefore, our results can be considered as a prediction of the Debye temperatures for these compounds.

Thermal conductivity is often higher in materials having a high Debye temperature. According to Table III-5, $SrVO_3$ possesses the highest Debye temperature, while $BaRuO_3$ has the lowest. Consequently, the thermal conductivity decreases in the following order: B($SrVO_3$) > B($SrRuO_3$) and B($BaVO_3$) > B($BaRuO_3$).

We calculated the melting temperature using the empirical relation **[43]:**

$$T_m(K) = [553 \pm (\frac{5.911 C_{11}}{GPa})]\ (K) \pm 300K \quad \textbf{(III-18)}$$

It is found that the melting point of $SrVO_3$ is higher than other compounds. This conclusion aligns with my interpretation of the results for Young's modulus, indicating that $SrVO_3$ is a harder compound.

Table III-5 : Calculated longitudinal elastic wave velocity (v_l), transverse (v_t), average wave velocity (v_m), melting and Debye temperature (T_m and θ_D) of $SrVO_3$, $BaVO_3$, $BaRuO_3$, $SrRuO_3$.

Compound	v_l(m/s)	v_t(m/s)	v_m(m/s)	T_m(K)	θ_D(K)
$SrVO_3$	8113.98	4673.68	5189.73	2759.0132	692.101
$SrRuO_3$	6695.19	3609.66	4029.41	2484.3679	522.797
$BaVO_3$	7353.86	4200.55	4667.73	2467.9126	608.837
$BaRuO_3$	6296.51	3518.59	3917.01	2354.9649	499.967

III-3-2-b The anisotropy of the Young's modulus

we calculate the elastic compliance matrix S_{ij} which is the inverse of the elastic matrix C_{ij} ($S_{ij} = C_{ij}^{-1}$). From this matrix, we can calculate the elastic moduli. We are interested in the Young's modulus E which represents the deformation of the material along the direction of application of a uniaxial mechanical stress. Thus, the greater the value of the Young's modulus, the more difficult it is to deform the material in this direction. The expression of the surface in the 3D representation of the Young's modulus, for cubic systems is given by [44]:

$$\frac{1}{E} = s_{11} - 2(s_{11} - s_{12} - \frac{1}{2}s_{44})(l_1^2 l_2^2 + l_2^2 l_3^2 + l_3^2 l_1^2) \qquad \textbf{(III-19)}$$

l_i represents the direction cosines. If the value of $\left(s_{11} - s_{12} - \frac{1}{2}s_{44}\right)$ is positive, the Young's modulus is maximal in the <111> direction and minimal in the <100> direction. This confirms that <111> are the stiffest directions.

Young's modulus, linear compressibility, shear modulus, and Poisson's ratio for $SrVO_3$, $BaVO_3$, $BaRuO_3$, $SrRuO_3$ perovskite alloys are presented in both 2D and 3D formats in Figures III-4, and III-5, respectively. The deviations from the spherical shape in these figures illustrate the extent of anisotropy in the physical properties. In Figures III-4, and III-5, the blue curves indicate the maximum values, while the green curves represent the minimum values for the parameters. The maximum, minimum values and anisotropy for all parameters of the two alloys are also presented in Table III-6. The 3D representations of the linear compressibility for these alloys, as illustrated in Figures III-4, and III-5, exhibit an almost spherical structure. This suggests that the linear compressibility of each alloy exhibits minimal anisotropy.

For cubic $SrRuO_3$ alloys, which have an A value of less than unity (0.71), and for $BaVO_3$ alloys, which have values greater than one (1.486), the three-dimensional representations of Young's modulus, shear modulus, and Poisson's ratio reveal significant deviations from spherical symmetry, indicating a high degree of anisotropy in different crystallographic directions. In contrast, cubic $SrVO_3$ and $BaRuO_3$ alloys, with an A value closer to unity (0.952) and (0.903) respectively, exhibit only minor deviations from spherical symmetry. The observed directional dependence of these elastic properties suggests that the degree of elastic anisotropy follows the order :

$BaVO_3$ >$SrRuO_3$ > $SrVO_3$ > $BaRuO_3$.

Table III-6 : The maximum and minimum values of Young's modulus (E, in GPa), linear compressibility (B, in TPa^{-1}), shear modulus (G, in GPa) and Poisson's ratio (v) of $SrXO_3$ (X = V, Ru) pérovskite alloys.

Material		Young's modulus		Linear compressibility		Shear modulus		Poisson's ratio	
		E_{min}	E_{max}	β_{min}	β_{max}	G_{min}	G_{max}	ν_{min}	ν_{max}
$SrVO_3$	Value	286.8	298.7	1.7405	1.7405	114.68	120.44	0.23281	0.263
	Anisotropy	1.042		1.0000		1.05		1.1297	
$SrRuO_3$	Value	244.13	321.9	1.8314	1.8314	95.628	133.54	0.16566	0.35851
	Anisotropy	1.319		1.0000		1.396		2.1641	
$BaVO_3$	Value	239.12	334.05	1.6534	1.6534	91.808	136.48	0.11334	0.3842
	Anisotropy	1.397		1.000		1.487		3.3898	
$BaRuO_3$	Value	228.24	248.68	1.922	1.922	89.108	98.605	0.24457	0.30754
	Anisotropy	1.09		1.000		1.107		1.2575	

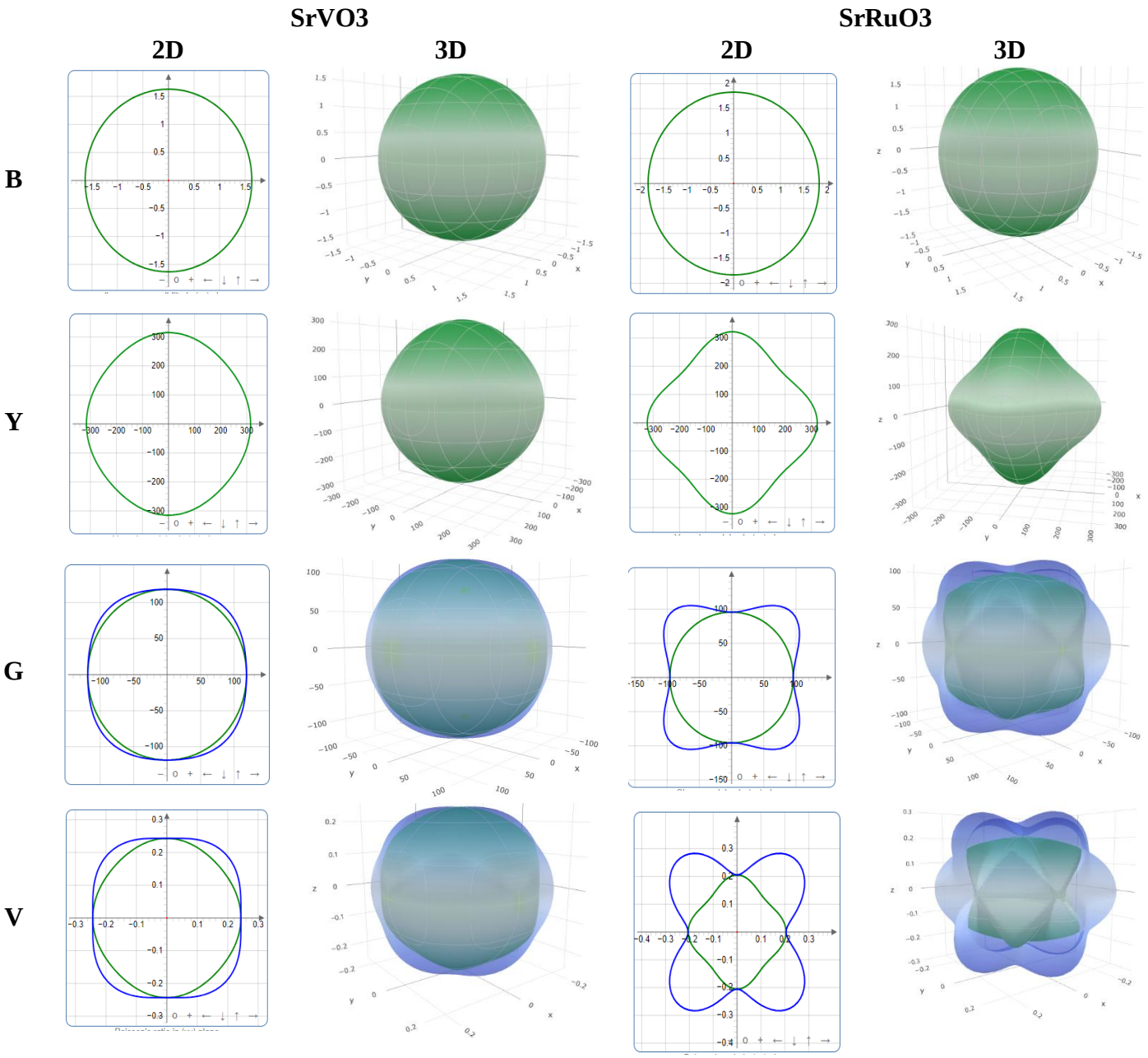

Figure III-4: The compressive modulus B, Young's modulus E, shear modulus G and Poisson's ratio v in 2 dimensions (2D) and in 3 dimensions (3D) for $SrVO_3$ and $SrRuO_3$ compounds.

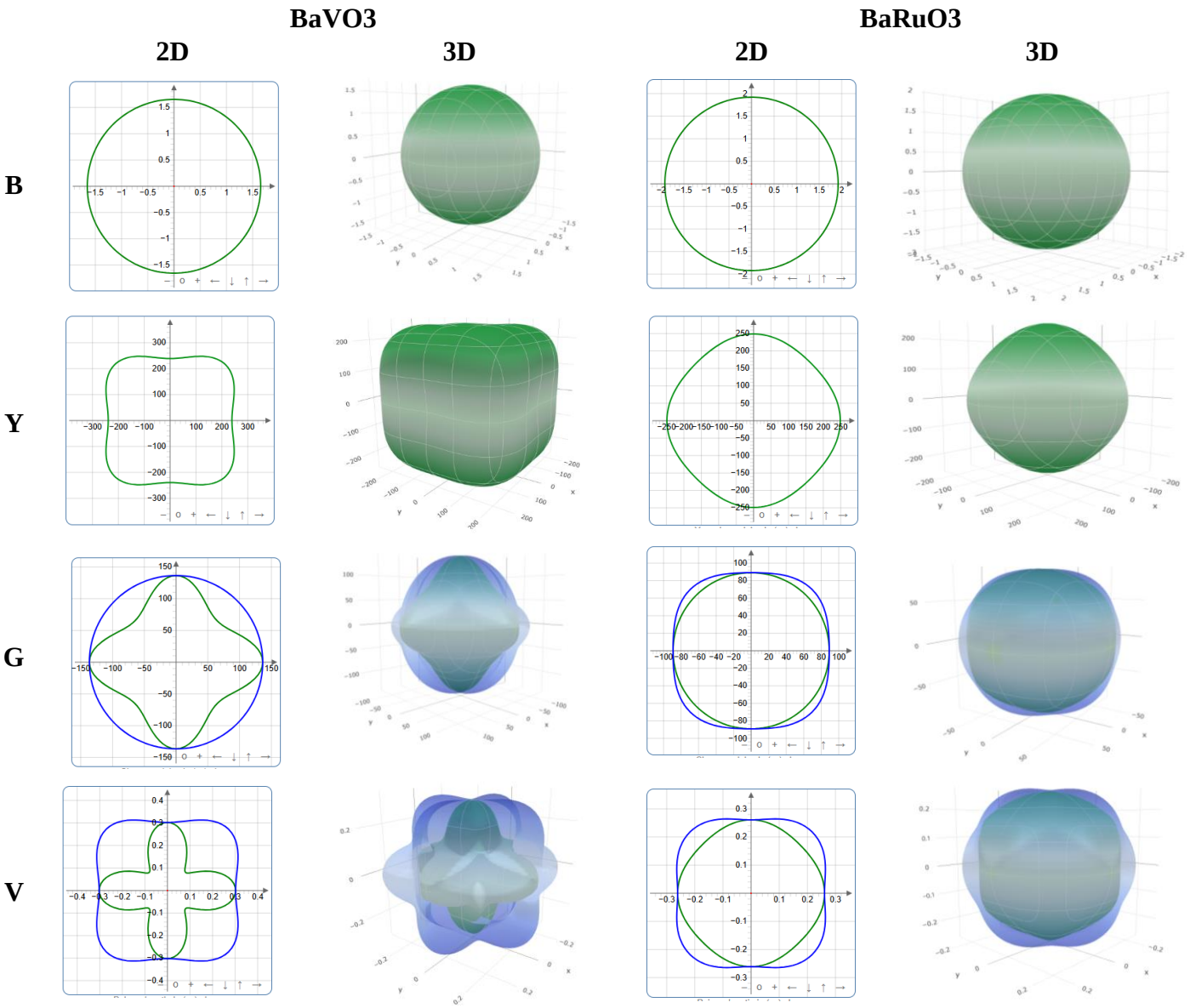

Figure III-5: The compressive modulus B, Young's modulus E, shear modulus G and Poisson's ratio v in 2 dimensions (2D) and in 3 dimensions (3D) for $BaVO_3$ and $BaRuO_3$ compounds.

III –3-3 Electronic Properties

The importance of the electronic properties of a material lies in the fact that they allow us to analyze and understand the nature of the bonds that form between the different elements of the material as well as to specify its character (insulator, conductor or semiconductor). These properties include band structures, charge densities and densities of states.

III –3-3-a Band structure

The energy band theory of solids is an approach that allows the study of the electronic properties of periodic structures which leads to classifying them according to the degree of filling of the energy bands in their ground state.

The occupation of the different energy states by electrons follows the Fermi Dirac distribution. There is a characteristic energy, the Fermi level, which sets, when the material is at a temperature of zero Kelvin, the energy level up to which electrons are found, that is to say the energy level of the highest occupied level. The Fermi level represents the chemical potential of the system. Its position in the energy band diagram is related to the way in which the bands are occupied.

In conductors, the Fermi level is in a permitted band which is in this case the conduction band. Electrons can then move in the electronic system, and therefore circulate from atom to atom.

In insulators and semiconductors, the Fermi level is located in the forbidden band which separates the valence and conduction bands. The energy gap is defined as the difference between the maximum of the valence band and the minimum of the conduction band. There are two types of gap:

Direct gap: the minimum of the conduction band has the same vector k as the maximum of the valence band.

Indirect gap: the minimum of the conduction band and the maximum of the valence band are at different points in the reciprocal space.

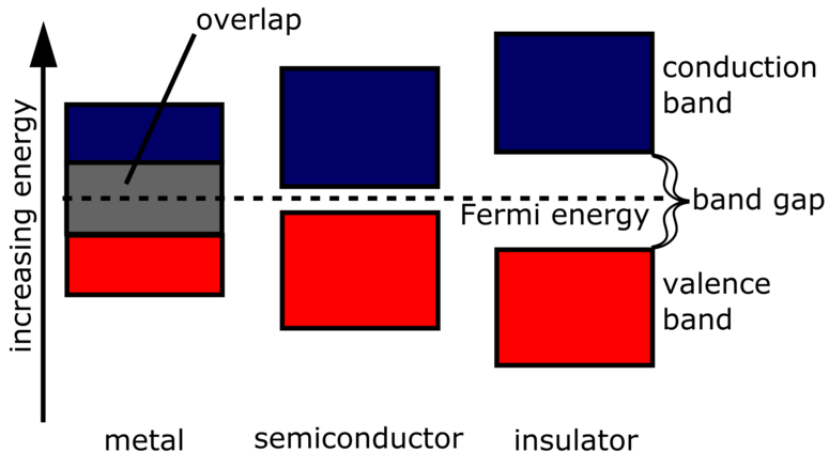

Figure III-3-6: Position of energy bands for a metal, a semiconductor and an insulator.

In Figure III-6, we have plotted the band structure along the high symmetry points in the first Brillouin zone using the GGA-WC and mBJ approximations in the context of Tran and Blaha (TB) [45] for both spin states, Dn and Up. In these plots, the Fermi level is depicted by a horizontal dashed line and is set to 0 eV, serving as the energy reference point. The vertical axis, ranging $[-8.0 \text{ to } +8.0\,]$eV, represents the energy E (eV) of the states relative to the Fermi energy.

The data presented in Fig. III-7 clearly demonstrate that the up spin (↑) channel and the down spin (↓) channel exhibits metallic properties for the both componds due to overlaps bands (the valence band and the conduction band). Consequently, the interaction between these two channels results in the metallic ferromagnetic (HMF) behavior observed in the studied compounds with WC-GGA approximations.

The results of the electronic band structure calculations employing the mBJ-GGA approximation are presented in Fig. III-8. In these calculations, the Modified Becke-Johnson (mBJ) exchange potential is utilized to enhance the band gap and improve the electronic properties of the materials under investigation.

we can see, for the spin up channel of $SrVO_3$ and $BaVO_3$, a metallic character due to the intersection of the valence bands with the Fermi level. On the other hand, for the spin-down channel, the compound exhibits a semiconductor character. In this channel (spin-DN), we can see :

- For $SrVO_3$, in the spin-down configuration, the valence band maximum is positioned at the R point with an energy of −2.33 eV, while the conduction

band minimum is located at the Γ point with an energy of 0.41 eV. This results in a indirect band gap of 2.74 eV.

- The spin-down configuration of BaVO3 shows that the conduction band minimum is at the Γ point with an energy of (0.52 eV), while the valence band maximum is at the R point with an energy of (−2.18 eV). The indirect band gap as a result is 2.70 eV.

Conversely, for $SrRuO_3$ and $BaRuO_3$, we observe the opposite behavior: it demonstrates metallic behavior in the minority spin channel , while the majority spin channel exhibits semiconducting behavior. we can see in this channel (spin-UP) :

- For $SrRuO_3$, in the spin-up configuration, the indirect band gap is located between the minimum of the conduction band at Γ (0.0 eV) and the maximum of the valence band at R (−0.65 eV), resulting in an energy difference of 0.65 eV
- The indirect band gap for BaRuO3 in the spin-up configuration is situated between the valence band's maximum at R (-0.42 eV) and the conduction band's lowest at Γ (0.0 eV), creating an energy differential of 0.42 eV.

Consequently, ABO_3 compounds (A = Sr, Ba and B = V, Ru) can be classified as a half metallic perovskite.

Semiconductors are characterized by a band gap (energy gap), which separates states located on a higher band in the valence band (VB) and states located on a lower band in the conduction band (CB). Thus we calculated the half-metallic gap E_{HM} which is an important parameter to consider for potential applications in spintronic devices; it is defined as the energy difference between the conduction band minima and the Fermi level (E_F).

As for the values of the energy gaps (E_g) and (E_{HM}), relative to all compounds made by the approach (TB-mBJ), they are presented in table III-7.

The spin polarization (P) at the Fermi level E_F (in relation to the electronic densities of states DOS), of a material is defined by the following equation:

$$P = \frac{\rho\uparrow(E_F) - \rho\downarrow(E_F)}{\rho\uparrow(E_F) + \rho\downarrow(E_F)} \qquad \textbf{(III-19)}$$

Where $\rho\uparrow(E_F)$ and $\rho\downarrow(E_F)$ are the density of states of the spins at the Fermi level (E_F). The ↑ and ↓ indicate the majority and minority spin, respectively. The electrons at the

Fermi level E_F are fully spin polarized (P = 100%) when $\rho\uparrow(E_F)$ or $p\downarrow(E_F)$ is equal to zero. Our results are presented in Table III–7.

Table III-7 : The half-metallic band gap E_{HM} (eV), minority spin band gap E_g (eV) and spin polarization P (%) at the Fermi level (E_F) of $SrVO_3$, $BaVO_3$, $BaRuO_3$, $SrRuO_3$. obtained using TB-mBJ.

	E_{HM}	E_g	$\rho\uparrow(E_F)$	$\rho\downarrow(E_F)$	P(%)
$SrVO_3$	0.99	2.74	1.40	0	100
$SrRuO_3$	0	0.65	0	-1.3	100
$BaVO_3$	1.05	2.70	1.50	0	100
$BaRuO_3$	0	0.42	0	-1.06	100

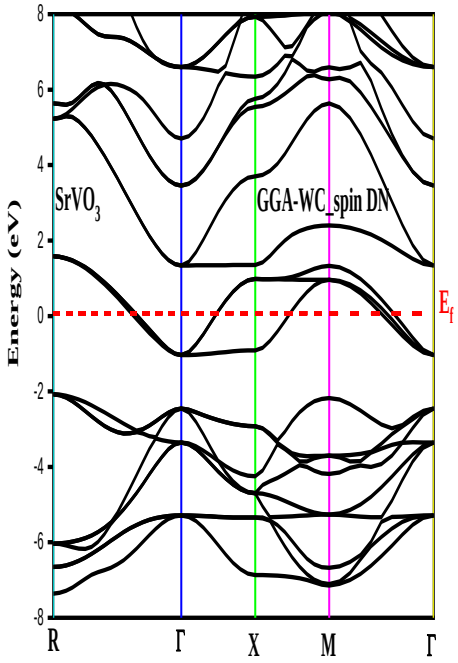
SrVO3
GGA-WC_spin DN
Energy (eV)
Ef
R
Γ
X
M
Γ

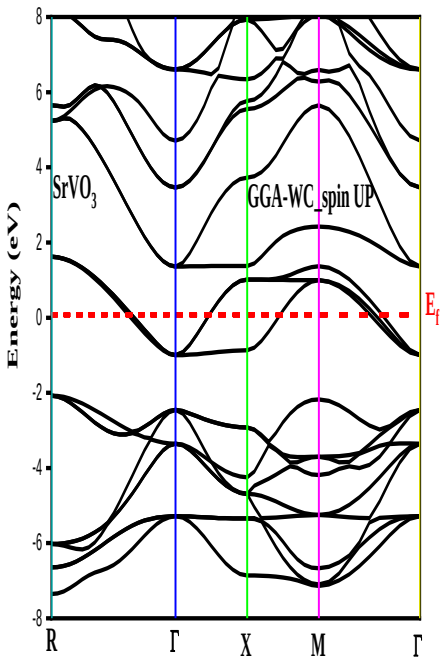
SrVO3
GGA-WC_spin UP
Energy (eV)
Ef
R
Γ
X
M
Γ

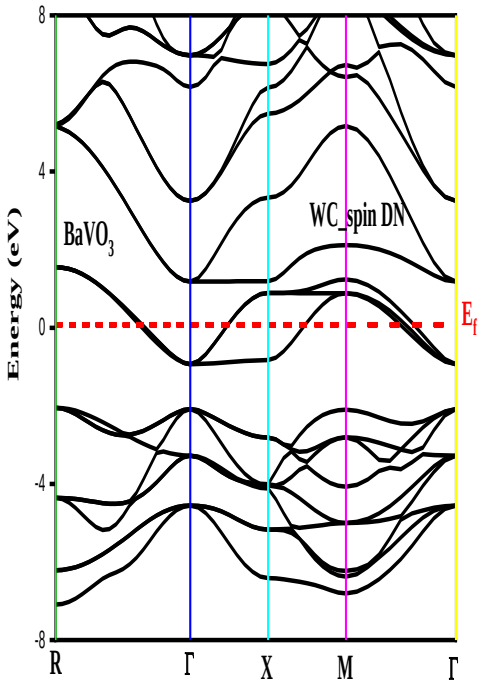
BaVO3
WC_spin DN
Energy (eV)
Ef
R
Γ
X
M
Γ

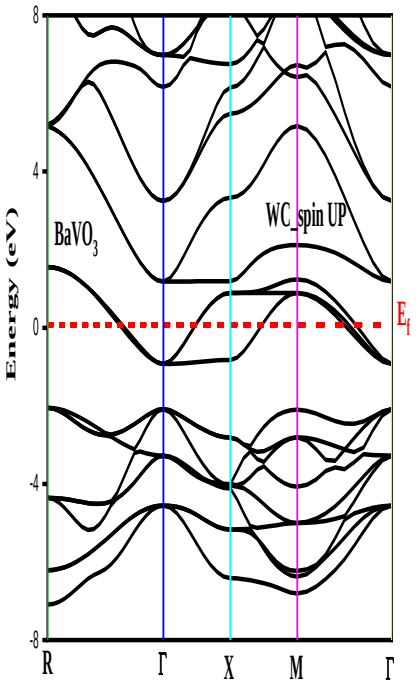
BaVO3
WC_spin UP
Energy (eV)
Ef
R
Γ
X
M
Γ

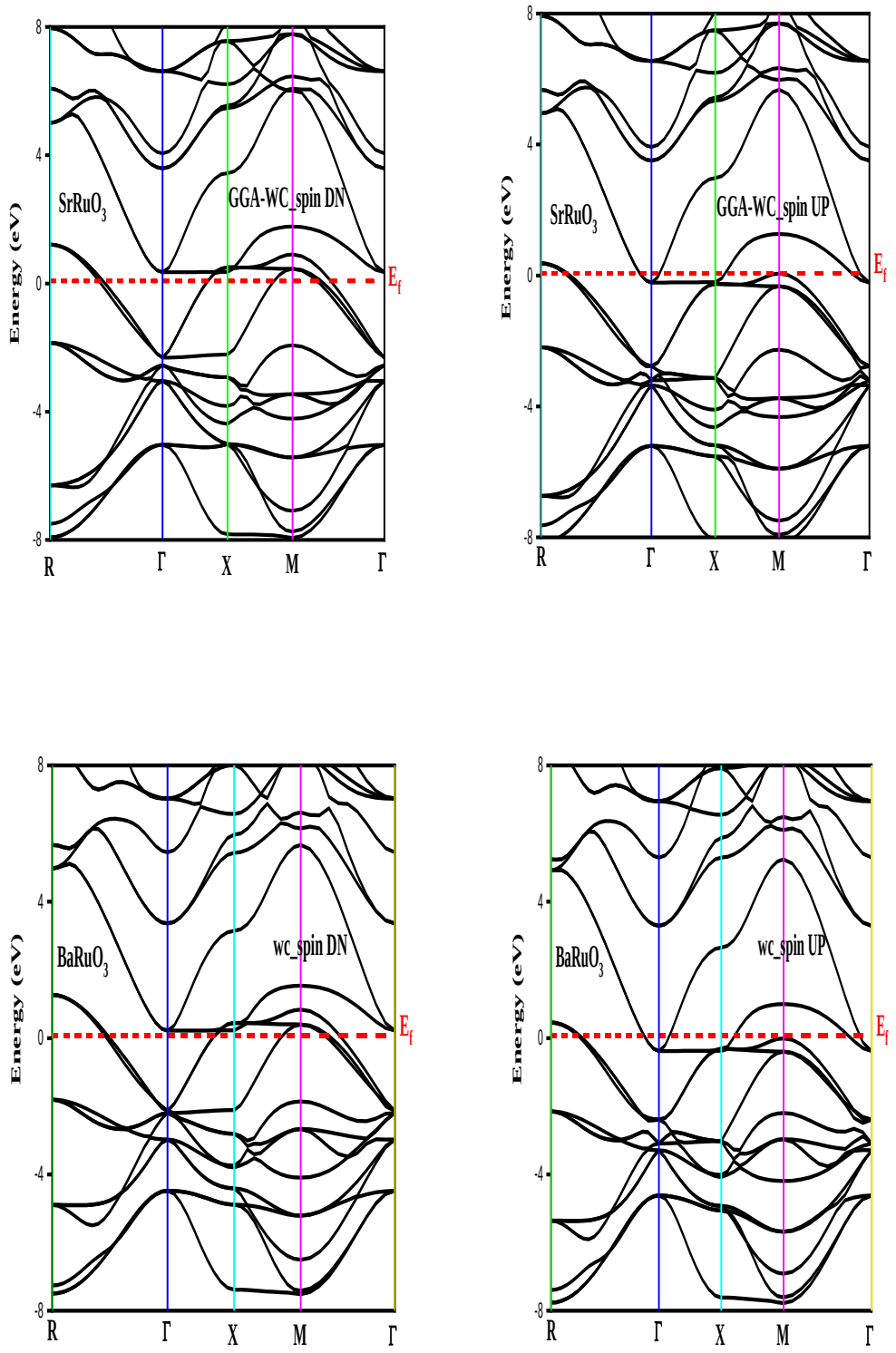

Figure III-7: The band structure of $SrVO_3$ and $SrRuO_3$ along lines of high symmetry of the Brillouin zone with WC-GGA approximations.

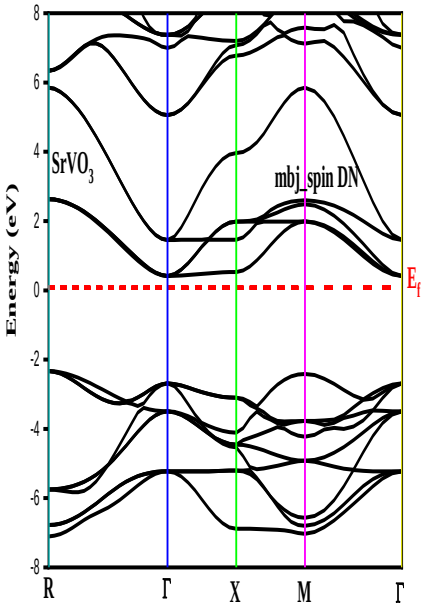
SrVO3
mbj_spin DN
Ef
Energy (eV)
R
Γ
X
M
Γ

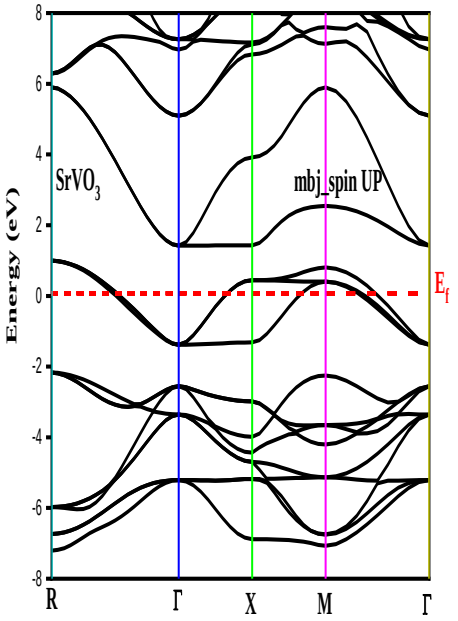
SrVO3
mbj_spin UP
Ef
Energy (eV)
R
Γ
X
M
Γ

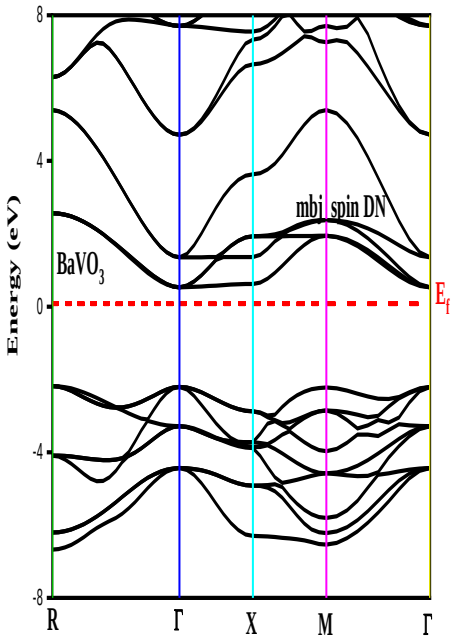
BaVO3
mbj_spin DN
Ef
Energy (eV)
R
Γ
X
M
Γ

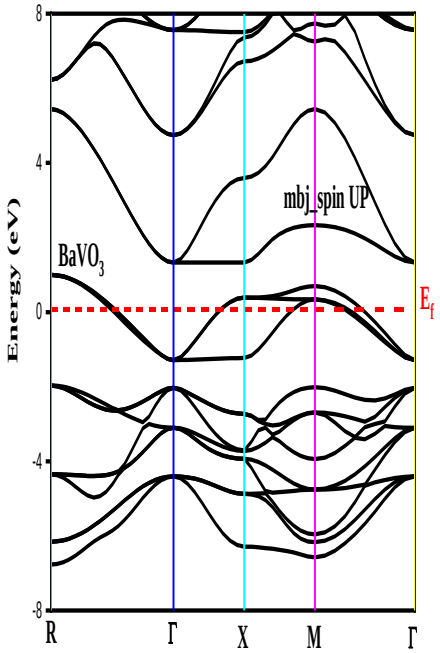
BaVO3
mbj_spin UP
Ef
Energy (eV)
R
Γ
X
M
Γ

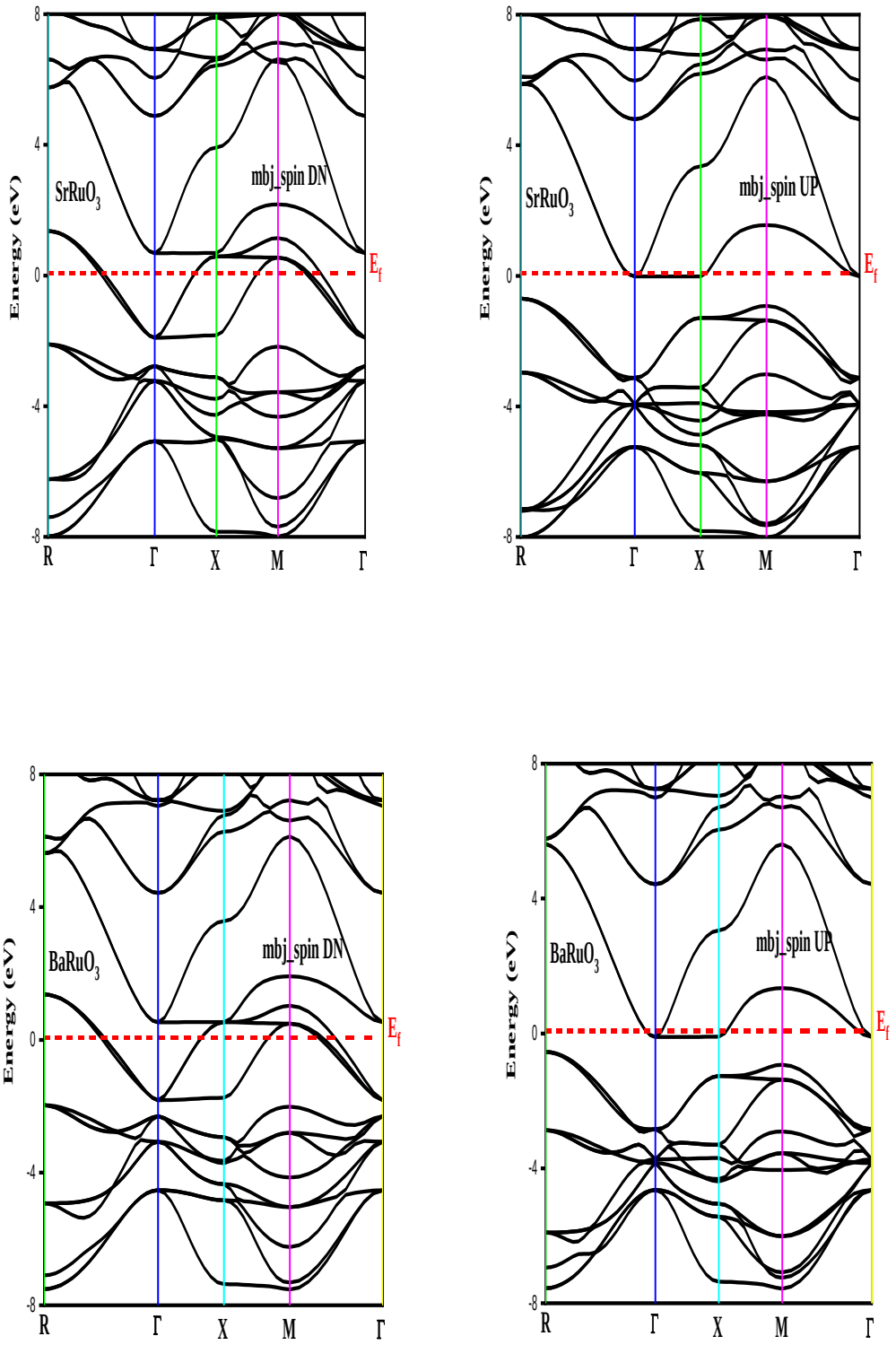

Figure III-8: The band structure of SrVO3 and SrRuO3 along lines of high symmetry of the Brillouin zone with TB-mBJ approximations.

III -3-3-b Density of states

The electronic density of states (DOS) is one of the most important electronic properties. It can be considered as a means of deciphering. Determining the total and partial density of states spectra allows us to:

- Better understand the band structure.
- Know the nature and states responsible for the bonds.
- Know the type of hybridization.
- Determine the predominant character for each region.

We calculated the total and partial densities of states (DOS) in the stable magnetic phase of ABO_3 compounds (A = Sr, Ba and B = V, Ru) using the optimized lattice parameter in the structural property calculations and using the TB_mBJ approximation. The total (DOS) and partial (PDOS) densities of states of ABO_3 , as a function of energy in eV, are shown in Figs. (III-9, III-10). The Fermi level EF is taken at an energy of 0 eV.

The total density of states projected onto each element's atomic orbitals (s, p, and d states) yields the PDOS. The energy scale's reference point is the Fermi energy level. Both the GGA and mBJ-GGA approximations were used to obtain these results, taking into account spin-up and spin-down polarizations. While the mBJ-GGA approximation successfully corrected earlier property estimations, confirming that SrVO3 and SrRuO3 are half-metal perovskites, the TDOS confirms our previous observations about the nature of the materials. The magnetic nature of each compound is emphasized by the DOS plots, which also show variations in electronic density between the spin-up and spin-down states.

Table III-8 show localization of energy bands and state contributions for $SrVO_3$, $BaVO_3$, $BaRuO_3$, $SrRuO_3$.

Table III-8: Localization of energy bands and state contributions for $SrVO_3$, $BaVO_3$, $BaRuO_3$, $SrRuO_3$ using TB_mBJ approximation.

	Interval and contribution of states			
	UP		DN	
$SrVO_3$	[-7 ; -2.5]	p_O , d_V	[-7 ; -2.5]	p_O , d_V
	[-2.5 ; 5]	d_V , p_O	[0.5 ; 5]	d_V , p_O
	[5 ; 8]	d_Sr , p_O	[5 ; 8]	d_Sr , p_O
$SrRuO_3$	[-8 ; -0.7]	p_O , d_Ru	[-8 ; -2]	p_O , d_Ru
	[1.14 ; 5]	p_O , d_Ru	[-1.5 ; 1.5]	p_O , d_Ru
	[5 ; 8]	d_Sr , p_O	[5 ; 8]	d_Sr , p_O
$BaVO_3$	[-6.5 ; -2]	p_O , d_V, p_Ba	[-8 ; -6]	d_Ba
	[-1.5 ; 5]	d_V, p_O	[-6 ; -0.6]	d_V, p_O
	[5 ; 8]	d_Ba	[2 ; 6.5]	p_O , d_V, p_Ba
$BaRuO_3$	[-8 ; -0.5]	p_O , d_Ru , p_Ba	[-8 ; -4.5]	d_Ba
	[0.17 ; 5.5]	d_Ru	[-4.5 ; 1.5]	p_O , d_Ru
	[5.5 ; 8]	d_Ba , p_O	[1.5 ; 8]	p_O , d_Ru, p_Ba

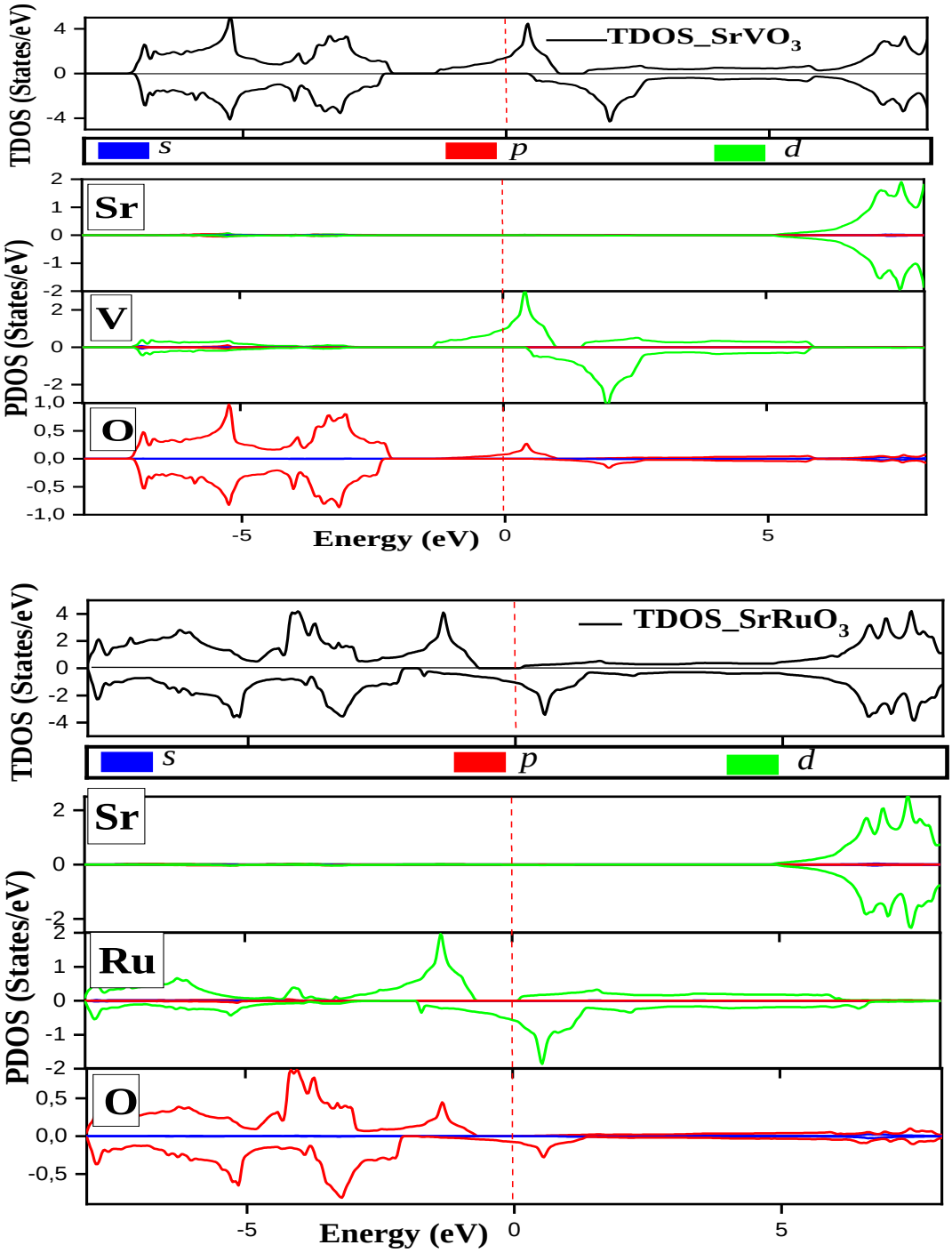

Figure III-9: Total and Partiel density of states for SrVO3 and SrRuO3 using the mBJ–GGA approximations.

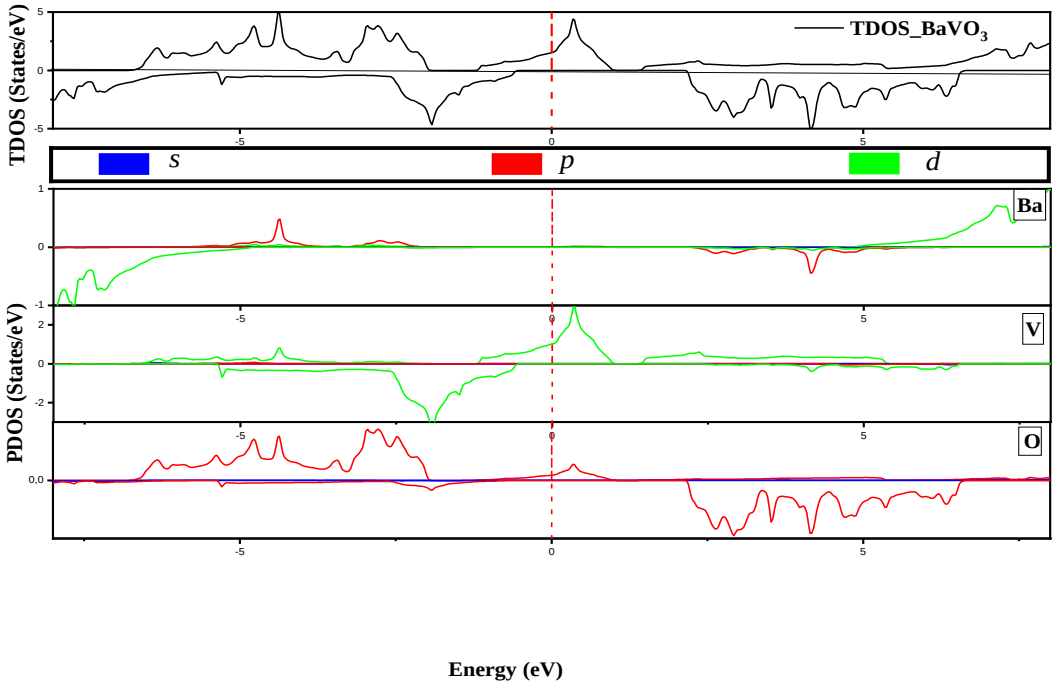

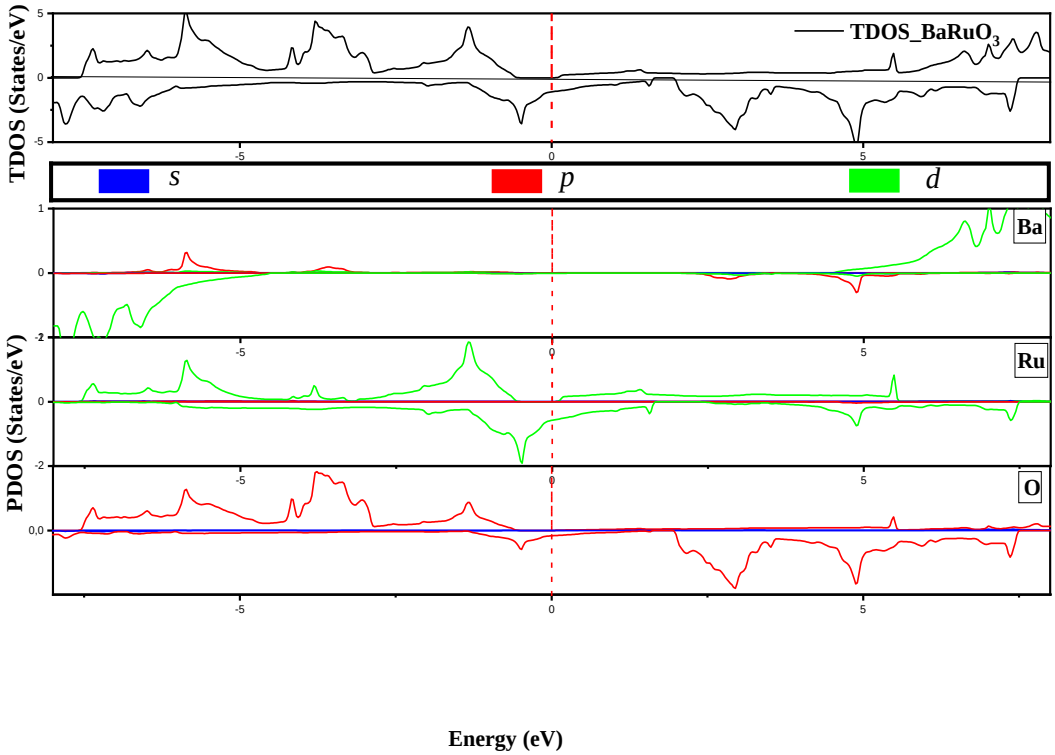

Figure III-10:Total and Partiel density of states for BaVO3 and BaRuO3 using the mBJ–GGA approximations

III -3-3-c Charge density

Charge density is another way that we can analyze the nature of bonds in materials. So it tells us whether they are ionic, covalent or mixed.

We calculated the total charge density as an isoenergetic contour located in the (110) plane using the mBJ approximation. Because of similarities between the results obtained for spins up and spins down, we plotted the results for spins up. The figure III-11 shows the distribution of charges (charge maps or counters) using the XCrysden program for the FM phase.

For the charge densities of ABO_3 compounds (A = Sr, Ba and B = V, Ru), the following observations are emphasized:

- Around the (V, Ru) and O atoms, the contours are significantly distorted (in both structures), indicating a covalent character for the Ru-O and V-O bonds.
- The symmetry around the (Sr, Ba) atom is nearly spherical, with a very slight deviation towards the oxygen atom, suggesting that the Sr-O and Ba-O bonds is ionic.

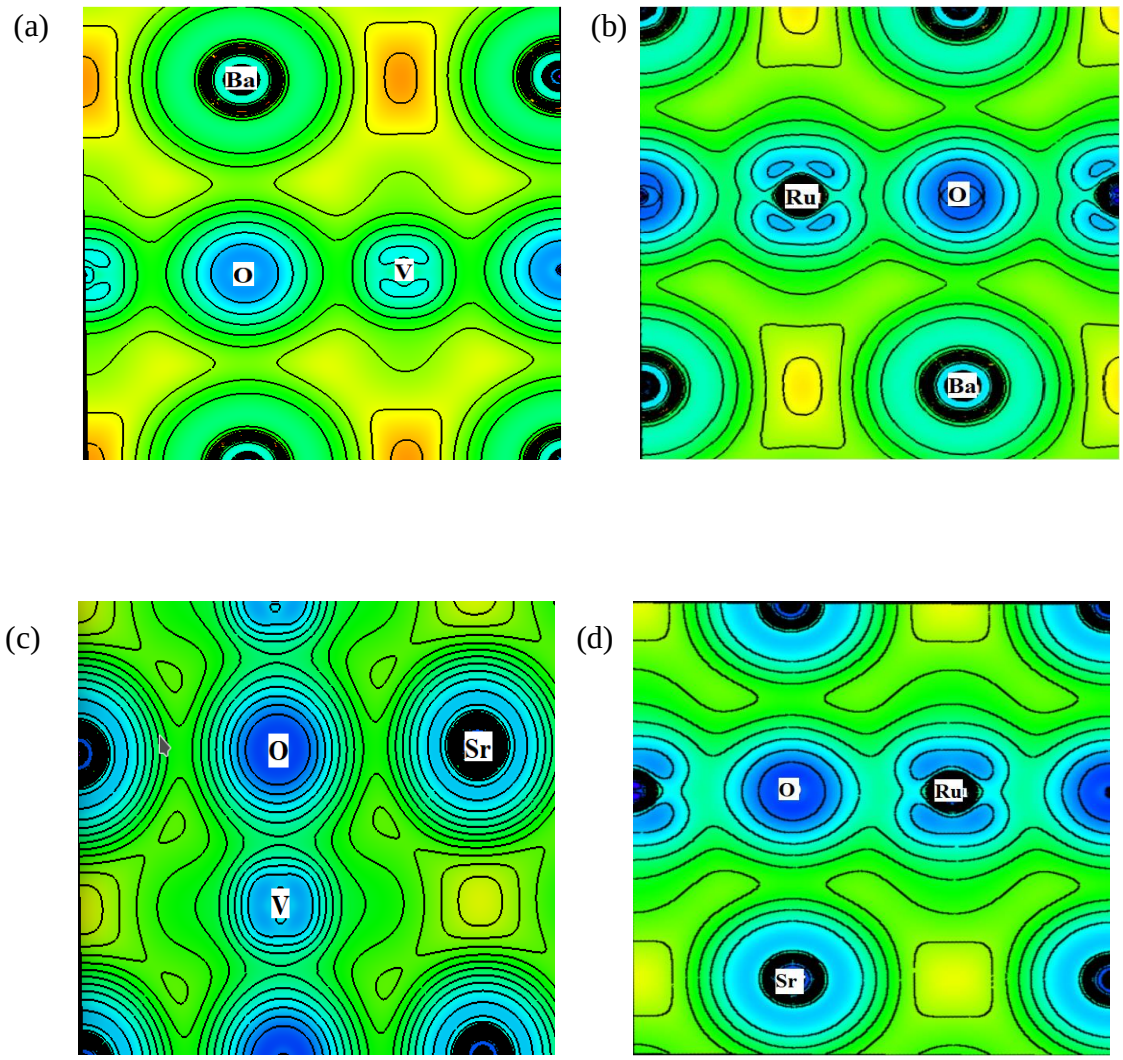

figure III-11 : The electronic charge density of $BaVO_3$ (a), $BaRuO_3$ (b), $SrVO_3$ (c) and $SrRuO_3$ (d) compounds obtained using the mBJ approach.

III – 3-4 Magnetic properties

The calculated total, local and interstitial magnetic moments (in Bohr magneton μB), for ABO_3 compounds (A = Sr, Ba and B = V, Ru) are listed in Table III-9, using the mBJ approximation.

From the above table, we notice that:

- The magnetic moment is located mainly at the level of the B atom (V and Ru) while the contributions of the O atoms are very weak.
- The negative values of the magnetic moment of the A (Sr and Ba) and O atoms in ABO_3 compounds reduce the total magnetic moment.
- The ABO_3 compounds stabilize in the ferromagnetic phase. The integer value of the total magnetic moments per unit cell is 1μB for ($SrVO_3$ and $BaVO_3$) and

2μB for ($SrRuO_3$ and $BaRuO_3$), which affirms the semi-metallic character of the materials and their exploitability in the field of spintronics.

Table III-3-9: Calculated total spin magnetic moments $M_T(\mu_B)$, partial spin magnetic moment and interstitial magnetic moments (in μB) for $SrVO_3$, $BaVO_3$, $BaRuO_3$ and $SrRuO_3$ with TB-mBJ approximation.

Compound		M_{tot} (μB)	$M_{Sr/Ba}$ (μB)	$M_{V/Ru}$ (μB)	M_O (μB)	M_{int} (μB)
$SrVO_3$	This work	1.000	0.00197	0.89296	-0.03184	0.20058
	exp	-	-	-	-	-
$SrRuO_3$	This work	2.002	-0.00112	1.28780	0.15298	0.25640
	exp	1.6 [46]	-	-	-	-
BaVO3	This work	1.000	-0.00083	0.92713	-0.04652	0.21334
	exp					
BaRuO3	This work	2.000	-0.00202	1.22478	0.21289	0.13860
	exp					

III-3-5 Optical properties

Optical properties are defined from radiation-matter interactions, it is an important means for the study of energy levels, excitation states, and crystal defects. Optics involves several phenomena such as refraction, absorption, transmission, and reflectivity when light interacts with matter in solid state physics.

In this part the study of optical properties has been studied using only TB-mBJ, because of its success in determining gap energy with appreciable accuracy [47], and since optical properties are always related to the electronic band structure.

III-3-5-a The complex dielectric function (ε)

The radiation-matter interaction causes electronic transitions. The dielectric function of which will be determined by the electronic transitions between the valence bands and the conduction bands, according to the perturbation theory [48], which is expressed by the following relation:

$$\varepsilon(\omega) = \varepsilon_1(\omega) + \varepsilon_2(\omega) \quad \textbf{(III-20)}$$

Where $\varepsilon_1(\omega)$ and $\varepsilon_2(\omega)$ are the real part and the imaginary part of dielectric function respectively, are given by using the Kramers–Kronig relations [49, 50]:

$$\varepsilon_1(\omega) = 1 + \frac{2}{\pi} P \int_0^{\infty} \frac{\omega' \varepsilon 2(\omega')}{\left(\omega'^2 - \omega^2\right)} d\omega' \qquad \textbf{(III-21)}$$

$$\varepsilon_2(\omega) = -\frac{2\omega}{\pi} P \int_0^{\infty} \frac{\varepsilon_1(\omega') - 1}{\left(\omega'^2 - \omega^2\right)} d\omega' \qquad \textbf{(III-22)}$$

where ω is the frequency and P implies the principal value of integral of Cauchy defined by :

$$P = \lim_{\alpha \to 0} \int_{-\infty}^{\omega - \alpha} \frac{\varepsilon(\omega') d\omega'}{(\omega' - \omega)} + \lim_{\alpha \to 0} \int_{\omega + \alpha}^{+\infty} \frac{\varepsilon(\omega') d\omega'}{(\omega' - \omega)} \qquad \textbf{(III-23)}$$

The materials studied in this work crystallize in the cubic system, the principal components of $\varepsilon 2(\omega)$ are isotropic, $\varepsilon_2 xx = \varepsilon_2 yy = \varepsilon_2 zz$.

Figure (III -12) illustrate the dispersions of the real and imaginary parts, ε1(ω) and ε2(ω), respectively. The peaks in the variation curve of ε2(ω) Figure (III-12) correspond to interband electronic transitions, i.e., between the valence band and the conduction band. It is observed that the threshold energy, which corresponds to the first critical point, is approximately 2.70, 2.74, 0.65 and 0.42 eV, this corresponds to the band gap energy of $BaVO_3$, $SrVO_3$, $SrRuO_3$ and $BaRuO_3$. Below this threshold, the material is transparent, while beyond it, a rapid increase in the dielectric function is observed, accompanied by a succession of peaks.

The real part of the dielectric function for our compounds starts from zero frequency and increases to its maximum value at 8.40 eV, 7.74 ev, 7.95 ev and 8.85 eV, for $SrRuO_3$, $SrVO_3$, $BaRuO_3$ and $BaVO_3$, respectively, then decreases with the increase in photon energy. It becomes negative in the energy ranges (23.9 to 27 eV) for $SrRuO_3$, (24.1 to 27 eV) and (21.83 to 23.92 eV) for $SrVO_3$, (12.45 to 14.2 eV) and (19.74 to 27 eV) for $BaRuO_3$, and (12.95 to 13.68 eV) and (19.23 to 27 eV) for $BaVO_3$. This phenomenon can be explained by the fact that all incident electromagnetic waves are reflected. Consequently, the material exhibits metallic behavior within these energy ranges [52].

Moreover, the presence of intensity peaks within the energy range of 3 to 5 eV (UV) indicates that the maximum absorbance of ABO_3 compounds makes them promising candidates for specific applications in optoelectronic devices (UV).

Position of the peaks in the imaginary part of the dielectric function and the corresponding optical transitions of the $SrVO_3$, $SrRuO_3$, $BaVO_3$ and $BaRuO_3$ compounds, grouped in the table III-10.

Table III-10: Position of the peaks in the imaginary part of the dielectric function and the corresponding optical transitions of $SrVO_3$, $SrRuO_3$, $BaVO_3$ and $BaRuO_3$ compounds.

Compound	Peaks	Energy Peaks (eV)	Type of Transition
$SrVO_3$	a_1	3.27	P_O→d_V
	a_2	4.94	P_O→d_V
	a_3	6.22	d_V→p_O
$SrRuO_3$	b_1	3.5	P_O→d_Ru
	b_2	6	d_Ru→d_V, d_Ru→p_O
$BaVO_3$	c_1	3.03	P_O→d_V
	c_2	4.68	P_O→d_V
	c_3	6.37	d_V→p_O
$BaRuO_3$	d_1	3.22	P_O→d_Ru
	d_2	5.11	d_Ru→p_O

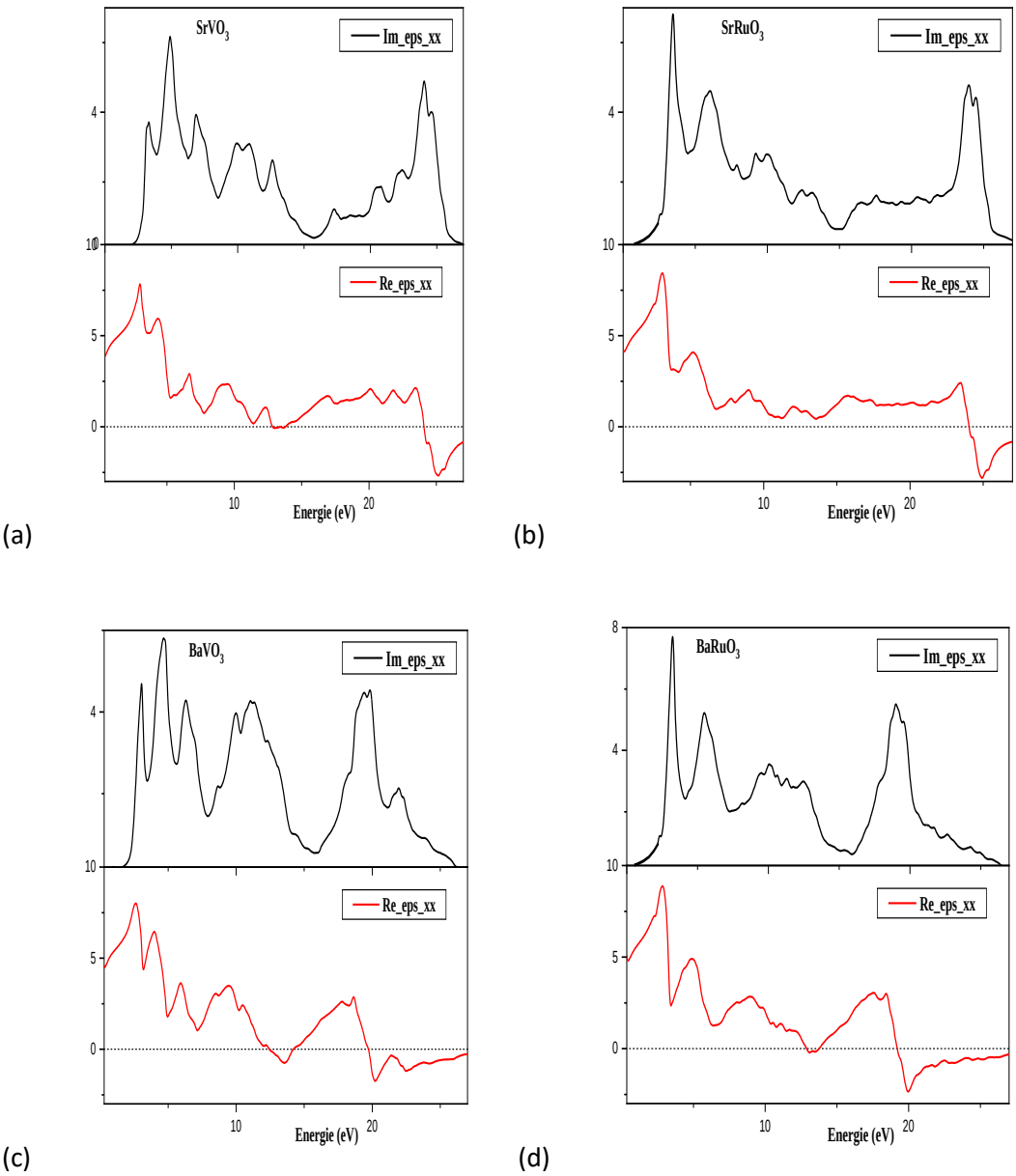

Figures III-12 : the real part $\varepsilon_1(\omega)$ and the imaginary part $\varepsilon_2(\omega)$ of dielectric function for $SrVO_3$ (a), $SrRuO_3$ (b), $BaVO_3$ (c) and $BaRuO_3$ (d) compounds obtained using the mBJ approach.

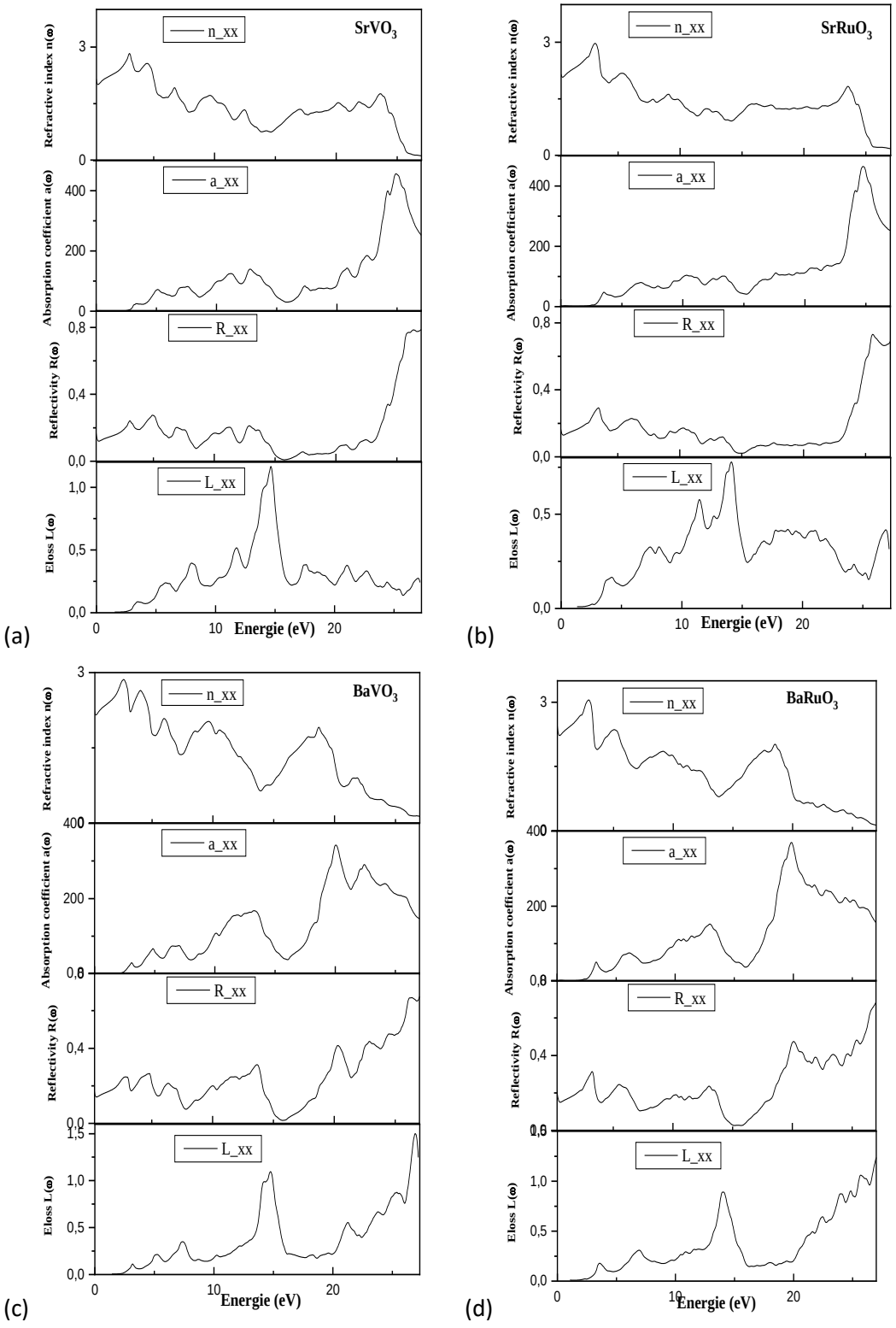

Figures III-13 : Optical properties calculated as a function of the incident photon energy (eV): refractive index n, absorption coefficient α, reflectivity R and energy loss L, of $SrVO_3$ (a), $SrRuO_3$ (b), $BaVO_3$ (c) and $BaRuO_3$ (d) compounds obtained using the mBJ approach.

III-3-5-b The Absorption Coefficient

The absorption coefficient is estimated using the formula below;

$$\alpha(\omega) = \sqrt{2\omega}\left[\sqrt{\varepsilon_1^2(\omega) + \varepsilon_1^2(\omega)} - \varepsilon_1(\omega)\right] \quad \textbf{(III-24)}$$

Figure III -13 illustrates the variation of the absorption coefficient as a function of energy. The first critical point appears at 2.70, 2.74, 0.65 and 0.42 eV, which is associated with the band gap (Eg) of $BaVO_3$, $BaRuO_3$, $SrVO_3$ and $SrRuO_3$, respectively. It is evident that a wide absorption range is observed, with intense absorption peaks at high energies. Therefore, our material could be a promising candidate for optoelectronic applications in the ultraviolet domain.

The absorption coefficient α reaches its maximum value of 454.54 × 10^{-4} cm^{-1} at 24.92 eV for $SrVO_3$, 463.03 × 10^{-4} cm^{-1} at 24.83 eV for $SrRuO_3$, 339.39 × 10^{-4} cm^{-1} at 20.04 eV for $BaVO_3$ and 370.42 × 10^{-4} cm^{-1} at 19.86 eV for $BaRuO_3$. It was also observed that the material is completely transparent in the range of 0 to 2.7 eV, meaning it cannot absorb light below the energy band gap values. However, beyond this threshold, its absorption increases rapidly. It can be concluded that our material exhibits high absorption in the ultraviolet (UV) range and can be utilized in detectors such as ultraviolet spectrophotometers, particularly in space technology applications.

III-3-5-c The refractive index and reflectivity

Knowing the real and imaginary parts of the dielectric function allows us to calculate other optical constants such as the refractive index n(ω), the reflectivity R(ω) using the following relations:

$$n(\omega) = \left[\frac{\varepsilon_1(\omega)}{2} + \frac{\sqrt{\varepsilon_1^2(\omega) + \varepsilon_2^2(\omega)}}{2}\right]^{1/2} \quad \textbf{(III-25)}$$

$$R(\omega) = \frac{(n-1)^2 + k^2}{(n+1)^2 + k^2} \quad \textbf{(III-26)}$$

Where: n is the refractive index, k is the extinction coefficient. The refractive index n(ω), characterizes the propagation speed of monochromatic radiation in a material and it is directly related to the value of the dielectric function of this material. While R(ω),

is an important parameter that characterizes the part of energy reflected at the interface of the solid.

From Figure III-13, we can read that the static refractive index $n(0)$ reaches a value of 2.04, 2.05, 2.14 and 2.19 for $SrVO_3$, $SrRuO_3$, $BaVO_3$ and $BaRuO_3$, respectively. Based on the real part of the dielectric function, the static refractive index can also be obtained using the following relation :

$$n = \sqrt{\varepsilon(0)} \qquad \textbf{(III-27)}$$

The value of $n(\omega)$ at low frequencies can be estimated as the square root of the dielectric function at zero energy level. Therefore, we can deduce that:

$$n_{SrVO3} = \sqrt{4.16} = 2.04, n_{SrRuO3} = \sqrt{4.21} = 2.05,$$

$$n_{BaVO3} = \sqrt{4.58} = 2.14, n_{BaRuO3} = \sqrt{4.80} = 2.19.$$

which gives us the same value obtained from Figure III-13.

The evolution spectra of reflectivity as a function of energy for the ABO_3 compounds are illustrated in Figure III-13. The reflectivity value at zero frequency is 12.98%, 14.50%, 14.93% and 15.61% for $SrVO_3$, $SrRuO_3$, $BaVO_3$ and $BaRuO_3$, respectively. The maximum reflectivity value is recorded at 22.97 eV, corresponding to 77.45%, 71.23%, 66.81% and 46.73%.

The reflectivity resulting from inter-band transitions exhibits several broad peaks in the UV region, a potential candidate for the fabrication of materials designed for UV radiation protection.

III-3-5-d The Energy-Loss Function

The energy loss function $L(\omega)$, is expressed by the relation:

$$L(\omega) = \frac{\varepsilon_2(\omega)}{\varepsilon(\omega)_1^2+\varepsilon(\omega)_2^2} \qquad \textbf{(III-28)}$$

It is associated with the energy loss of fast electrons crossing the compound from the valence band to the conduction band, usually it is higher than the plasmon energy [51]. The remarkable peak of $L(\omega)$ is joined to the plasmon oscillation resonance. It indicates the excitations of the electronic charge density in the material and is observed at 14.68

eV, 14.05 eV, 14.86 eV and 14.07 eV for $SrVO_3$, $SrRuO_3$, $BaVO_3$ and $BaRuO_3$, respectively. It should also be noted that these peaks correspond to the abrupt reduction in reflectivity R(ω).

III-4 Conclusion

The study of the structural, electronic, magnetic, optical, and mechanical properties of the $SrVO_3$, $SrRuO_3$, $BaVO_3$ and $BaRuO_3$ compounds in the cubic phase has allowed us to draw the following conclusions:

- The structural properties of the studied ABO_3 compounds (A = Sr, Ba and B = V, Ru) have shown that they are stable in the ferromagnetic (FM) phase.
- The electronic properties represented by the density of states and band structures have enabled us to obtain compounds with a wide bandgap semiconductor character. The TB-mBJ approximation has significantly improved the bandgap value.
- The chemical bonding in these materials exhibits a mixed character: covalent and ionic.
- The optical properties of ABO_3 compounds (A = Sr, Ba and B = V, Ru) have been determined. The results obtained indicate that these materials can be used in UV-based optoelectronic devices.
- The ABO_3 compounds (A = Sr, Ba and B = V, Ru) are mechanically stable, elastically anisotropic, and ductile.

reference

[1] P.Blaha, et al, Wien2k, T.U. Wien, Editor. Vienna, (2001).

[2] Z.Wu and R. E. Cohen, More Accurate generalized gradient approximation for solids, Physical Review B, 73 (23) 235116, (2006).

[3] J. P. Perdew, K. Burke and M. Ernzerhof, Phys. Rev. Lett. 77-3865, (1996).

[4] F.Tran , P. Blah, Phy. Rev. lett, 124 (2009).

[5] A.D. Becke and E.R. Johnson, J. Chem. Phys. 124, 221101, (2006).

[6] TAKENO, S., OHARA, R., SANO, K., et al. Surface and Interface Analysis: An International Journal devoted to the development and application of techniques for the analysis of surfaces, interfaces and thin films. 35, 1, 29-35, (2003).

[7] SHAULA, A. L., KHARTON, V. V., VYSHATKO, N. P., et al. Journal of the European Ceramic Society. 25, 4, 489-499, (2005).

[8] YAREMCHENKO, A. A., PATRAKEEV, M. V., KHARTON, V. V., et al. Solid state sciences. 6, 4, 357-366, (2004).

[9] C. Q. Jin and al. *Proceedings of the National Academy of Sciences* 105.20, 7115-7119, (2008):

[10] K. M. Hossain and al. arXiv preprint arXiv:1905.01437 (2019).

[11] M. Rashid and al. Journal of Superconductivity and Novel Magnetism 30, 3129-3136, (2017).

[12] S. Wahyu and S. Curtarolo. Computational materials science. 49, 2 , 299-312, (2010).

[13] F. D. Murnaghan, Proc. Natl. Acad. Sci. USA 30, 244(1944).

[14] S. Kanungo, et al. *Journal of Physics: Condensed Matter* 25.50. 505503. (2013).

[15] LIU, Z. T. Y., PODRAZA, N. J., KHARE, S. V., *et al. Computational Materials Science*, vol. 144, p. 139-146 (2018).

[16] DAGA, Avinash, SHARMA, Smita, et SHARMA, K. S. *Journal of Modern Physics*, vol. 2011 (2011).

[17] SHEIN, I. R., KOZHEVNIKOV, Victor L., et IVANOVSKII, Alexander L. *Solid State Sciences*, 2008, vol. 10, no 2, p. 217-225.

[18] SHEIN, I. R., KOZHEVNIKOV, V. L., et IVANOVSKII, A. L. *arXiv preprint cond-mat/ 0504286*, (2005).

[19] SINGH, David J.*Journal of applied physics*, vol. 79, no 8, p. 4818-4820 (1996).

[20] METE, E., SHALTAF, R., et ELLIALTIOĞLU, Ş. *Physical Review B*, vol. 68, no 3, p. 035119 (2003).

[21] ZHOU, J.-S. et GOODENOUGH, J. B. *Physical review letters*, vol. 94, no 6, p. 065501 (2005).

[22] SHANNON, Robert D. *Foundations of Crystallography*, 1976, vol. 32, no 5, p. 751-767.

[23] JIN, C.-Q., ZHOU, J.-S., GOODENOUGH, J. B., *et al. Proceedings of the National Academy of Sciences*, vol. 105, no 20, p. 7115-7119 (2008).

[24] ZHAO, Jianfa, GAO, Jiacheng, LI, Wenmin, *et al*. *Nature communications*, vol. 12, no 1, p. 747 (2021).

[25] LI, Chonghe, SOH, Kitty Chi Kwan, et WU, Ping. *Journal of alloys and compounds*, vol. 372, no 1-2, p. 40-48. (2004)

[26] T. Charpin, A package for calculating elastic tensors of cubic phases using Wien laboratory of geometrics', F-75252, Paris, France (2001)

[27] J. Wang, S. Yip, S. R. Phillpot and D. Wolf, Phys. Rev. Lett. 71 (1993) 4182

[28] W. Voigt and Ann, Phys. 38 (1889) 573.

[29] A. Reuss and Z. Angew, Math. Phys. 9, (1929) 49.

[30] R. Hill, Proc. Phys. Soc., London 65 (1952) 349.

[31] M.W. Barsoum, T. El-Raghi, W.D. Porter, H. Wang, S. Chakraborty, J. Appl. Phys. 88 (2000) 6313.

[32] Z. Sun, S. Li, R. Ahuja, J.M. Schneider, Solid State Comm. 129(2004) 589-592

[33] X-Q. Chen, H. Niu, D. Li, Y. Li, Intermetallics 19 (2011) 1275-1281.

[34] COHEN, Marvin L. *Physical Review B*, 1985, vol. 32, no 12, p. 7988.

[35] KING-SMITH, R. D. et VANDERBILT, David. *Physical Review B*, 1994, vol. 49, no 9, p. 5828.

[36] D.G. Pettifor, Mater. Sci. Technol. 8 (1992) 345.

[37] X.H. Kang and J. M. Zhang, J. Phys. Chem. Solid. 119, 71 (2018).

[38] H. Fu, D. Li, F. Peng, T.Gao, and X. Cheng, Comput. Mater. Sci. 44, 774 (2008).

[39] G. Surucu, Mater. Chem. Phys. 203, 106 (2018).

[40] SURUCU, Gokhan, KADEROGLU, Cagil, DELIGOZ, Engin, *et al. Materials Chemistry and Physics*, 2017, vol. 189, p. 90-95.

[41] O. L. Anderson J. Phys. Chem. Solids 24, (1996) 909.

[42] E. Schreiber, O. L. Anderson and N. Soga N, (New York: McGraw-Hill) (1973).

[43] C. Nianyi, L. Chonghe, Y. Shuwen, W. Xueye, J. Alloy. Comp. 234 (1996) 130.

[44] R.E. Newnham, Properties of Materials; Anisotropy, Symmetry, Structure, Oxford University Press, New York (2005).

[45] F.Tran , P. Blah, Phy. Rev. lett, 124 (2009)

[46] ZAYAK, A. T., HUANG, X., NEATON, J. B., *and al. Physical Review B—Condensed Matter and Materials Physics*, 2006, vol. 74, no 9, p. 094104.

[47] Y.-S. Kim, M. Marsman, G. Kresse, F. Tran, and P. Blaha , Physical Review B, 82(20), 205212, (2010).

[48] M. Fox, Optical Properties of Solids, Oxford University Press, Oxford, (2002).

[49] C.A. Draxl, J.O. Sofo, Comput. Phys. Commun. 175 (2006) 1–14.

[50] G. Harbeke, F. Abelès (Ed.), In Optical Properties of Solids, North-Holland, Amsterdam, (1972).

[51] P. Nozieres and D. Pines, Physical Review, 113(5), 1254, (1959).

[52] B. Xu, and al. The European Physical Journal B 66 (2008): 483-487.

Chapter IV :

The double perovskite $Ba_{2-x}Sr_xVRuO_6$

IV-1 Introduction

The structural, electronic and magnetic properties of double perovskite oxides have become a very important subject in the last two decades, as thanks to their physical properties, they have applications in renewable energy and also in the field of spin electronics (spintronics). The double perovskites Sr_2VRuO_6 and Ba_2VRuO_6 present a potential candidate in this field, there is little study on these materials, through our theoretical study, we will understand more the experimental results obtained on these classes of materials. Hence in this work we studied the structural, electronic, optical, and mechanical properties of double perovskite compound of the form $A_{2-x}B_xCDO_6$ where (A=Ba, B=Sr, C=V and D=Ru). The obtained compounds are grouped in the table IV-1

Table IV-1: Compounds obtained in function of x

X (rate of Sr)	compound
0	Ba_2VRuO_6
1	$BaSrVRuO_6$
2	Sr_2VRuO_6

IV-2 Crystallographic structure

The material $Ba_{2-x}Sr_xVRuO_6$ (x=0,1,2) crystallizes under ambient conditions in the cubic structure . With the space group Fm-3m (ranked 225 in the international table of crystallography). Table IV-2 gives the atomic positions of the cubic structure of our compounds. We used experimental lattice constants namely a = 7.835 Å [1] and a =7.933 Å[2] for Sr_2VRuO_6 and Ba_2VRuO_6 compounds, respectively. And For $BaSrVRuO_6$, we predict the lattice parameter and determine that a=7.72 Å

a-Prediction of the Lattice Parameter of Perovskite

A detailed understanding of the correlations between various intrinsic fundamental properties (such as atomic and ionic radii) within the perovskite structure is key to comprehending its behavior. Predicting the cubic or pseudo-cubic lattice parameter of perovskite materials is crucial, not only for their theoretical use in investigating the

physical properties of these compounds but also for proposing them for various technological applications. Moreover, such predictions pave the way for studying perovskite materials that have not yet been synthesized. Several empirical models have been developed to estimate the lattice constant of perovskites based on the atomic properties of their constituent elements.

We have found that the predictive formula for the lattice parameter of cubic and pseudo-cubic perovskites can be expressed as follows [3]:

$$2(r_b + r_x) + 2\sqrt{2}\, r_x \qquad \textbf{(IV-1)}$$

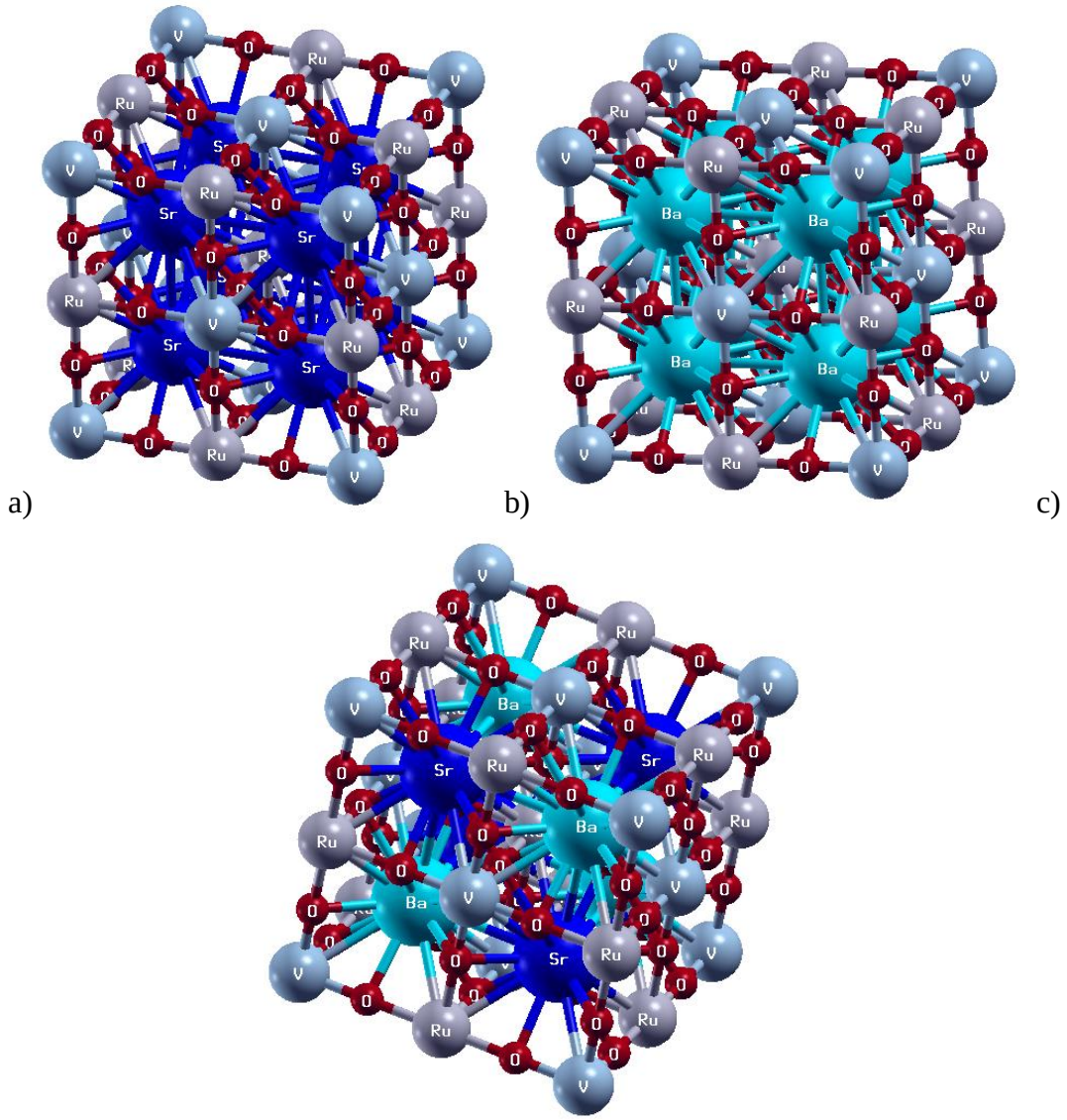

Figure IV-1 : Crystal structure in cubic phase of for a)Sr_2VRuO_6, b)Ba_2VRuO_6 and c)$BaSrVRuO_6$.

Table IV-2 :Atomic Positions in a double Cubic Oxide Perovskite Crystal of $Ba_{2-x}Sr_xVRuO_6$

atom	Wyckoff	**Sr_2VRuO_6**			**Ba_2VRuO_6**			**$BaSrVRuO_6$**		
		X	Y	Z	X	Y	Z	X	Y	Z
Ba	(8c)	-	-	-	0.25	0.25	0.25	0.25	0.25	0.25
Sr	(8c)	0.25	0.25	0.25	-	-	-	0.25	0.25	0.75
V	(4a)	0	0	0	0	0	0	0	0	0
Ru	(4b)	0.5	0.5	0.5	0.5	0.5	0.5	0.5	0	0
O	(24e)	0.256	0	0	0.252	0	0	0.239	0	0

IV-3 Calculation Details

For this material $Ba_{2-x}Sr_xVRuO_6$ (x=0,1,2), the calculations were performed using the same method as previously chapter. To study the various structural, elastic, electronic, magnetic, and optical properties in the cubic phase, we employed the Wu-Cohen Generalized Gradient Approximation (WC-GGA) and compared it with the modified Becke–Johnson exchange potential (TB-mBJ).

The value of RMT * Kmax was set to 8.0, and the number of k-points in the first Brillouin zone (BZ) was taken as 84 k-points, arranged in a 13 × 13 × 13 mesh for the cubic phase. The electronic configuration of the elements in the $Ba_{2-x}Sr_xVRuO_6$ compound and the muffin-tin radii are presented in Table **IV-3.**

Table IV-3: The values of R_{MT} and electronic configuration for each element used during our calculations

	atom	**Sr_2VRuO_6**	**Ba_2VRuO_6**	**$BaSrVRuO_6$**	**Electronic configuration**
R_{MT} (a.u)	Sr	2.47	/	2.38	[Kr]$5s^2$
	Ba	/	2.5	2.38	[Xe]$6s^2$
	V	1.88	1.87	1.67	[Ar] $3d^3 4s^2$
	Ru	1.83	1.89	1.88	[Kr] $4d^7 5s^1$
	O	1.58	1.62	1.51	[He]$2s^2 2p^4$

IV-4 Results and Discussion

IV-4-1 Structural Properties

Figure IV-2 illustrates the variations in total energy for the three compounds as a function of volume using the WC-GGA approximation.

Based on the results summarized in Table III-4-3, we can conclude that $Ba_{2-x}Sr_xVRuO_6$ (x=0,1,2) stabilizes in the ferromagnetic (FM) phase with a low energy value (E_o =-44417.089985, E_o = -34498.595017 and E_o =-24580.036 for Ba_2VRuO_6, $BaSrVRuO_6$ and Sr_2VRuO_6, respectively. Consequently, in the following sections, we will determine the different properties of the complex in the FM phase.

As shown in Table IV-4, the calculated lattice parameters for perovskite Ba_2VRuO_6 and Sr_2VRuO_6 in cubic structure are in good agreement with experimental.

Moreover, the negative formation energy of the investigated compound indicates its thermodynamic stability and potential for synthesis. As shown in Table IV-4, the formation enthalpies follow the order: ΔHf ($BaSrVRuO_6$) < ΔHf (Ba_2VRuO_6) < ΔHf (Sr_2VRuO_6). suggesting that $BaSrVRuO_6$ is the most stable among them.

Additionally, the computed bulk modulus values decrease in the following sequence:

B ($BaSrVRuO_6$) > B (Ba_2VRuO_6) > B (Sr_2VRuO_6). indicating that $BaSrVRuO_6$ possesses the highest hardness and the lowest compressibility compared to the other studied compounds.

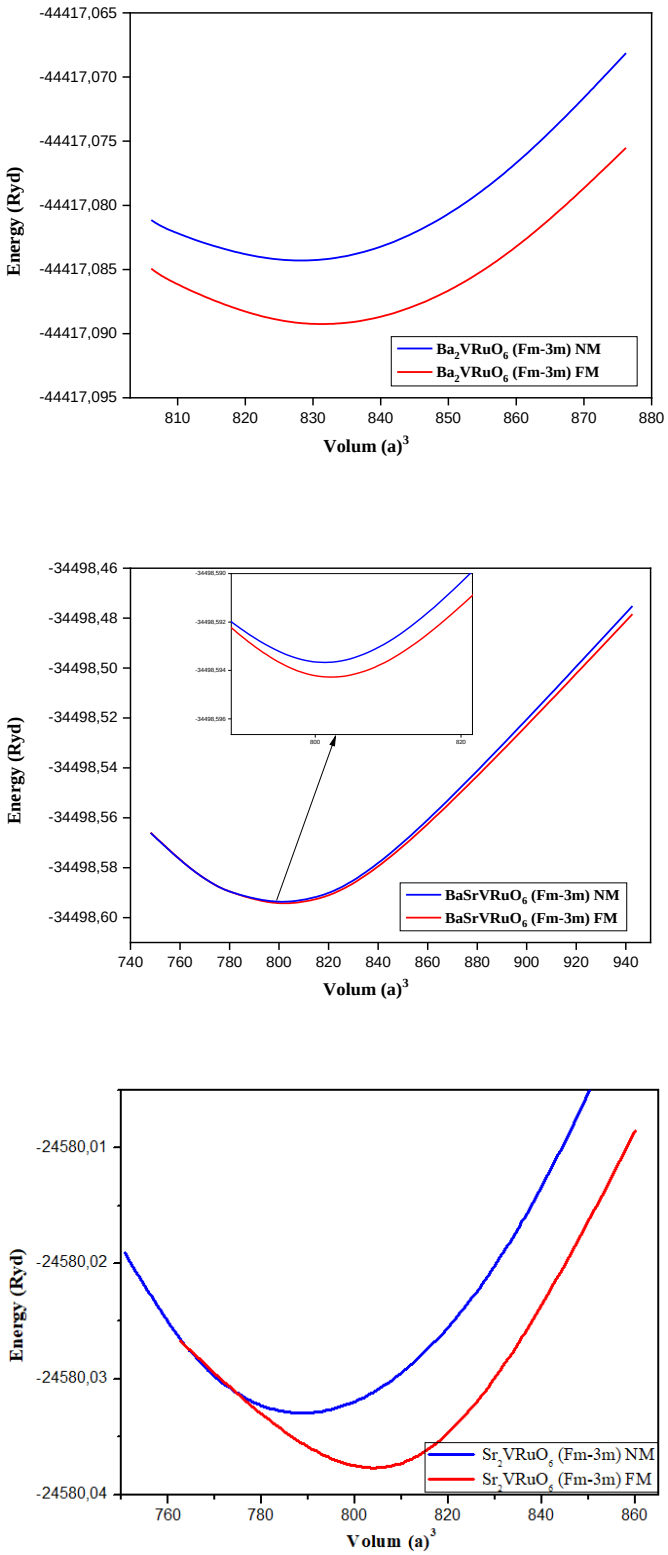

Figure IV-2: Representation of total energy as a function of volume for ferrimagnetic (FM) and non-magnetic (NM) states for for Ba_2VRuO_6, $BaSrVRuO_6$ and Sr_2VRuO_6.

Table IV-4: the calculated equilibrium cell volume V(Bohr^3), lattice parameter a (Å), bulk modulus B (GPa), first derivative of the bulk modulus B′(in GPa), equilibrium energy Etot (Ry) and formation enthalpy ΔHf (eV/mol), for Ba_2VRuO_6, $BaSrVRuO_6$ and Sr_2VRuO_6.

….	Space groupe	state	a_{Exp} (Å)	V(Bohr^3)	a (Å)	B'	B (GPa)	E_{tot}	ΔHf
Ba_2VRuO_6	Fm3m (n.221)	FM	7.933[2,4]	830.9823	7.8974	4.277	189.418	-44417.089985	-4.804
	Fm3m (n.221)	NM		827.787	7.887	4.238	193.753	-44417.085063	
$BaSrVRuO_6$	Fm3m (n.221)	FM	-	804.306	7.812	4.488	190.830	-34498.595017	-4.831
	Fm3m (n.221)	NM		802.985	7.8077	4.724	193.947	-34498.594452	
Sr_2VRuO_6	Fm-3m (n.225)	FM	7.835[1]	795.822	7.784	2.316	169.505	-24580.036	−4.794
	Fm-3m (n.225)	NM		789.249	7.762	4.704	197.681	-24580.032	

IV-4-2 Elastic Constants and Mechanical Properties

The calculation of mechanical properties was conducted following the same approach as in previou chapter, using the WIEN2k code. The obtained values of the elastic coefficients are presented in Table **IV-5**. It is observed that the mechanical stability conditions are satisfied for both systems. At this stage, various mechanical properties can now be determined.

Table IV-5: The elastic constants C_{11}, C_{12}, C_{44}, bulk modulus B, the shear modulus (G, G_V and G_R), Young's modulus E (GPa), anisotropic parameter A, B/G ratio, Poison's ratio ν and Vickers hardness H_V for Ba_2VRuO_6, $BaSrVRuO_6$ and Sr_2VRuO_6.

This Work	C_{11}	C_{12}	C_{44}	B	G_V	G_R	G	E	A	B/G	ν	H_v
Ba2vruo6	510.3101	39.7282	49.5280	196.588	123.832	72.388	98.110	252.350	0.21	2.003	0.286	9.97
Basrvruo6	323.9701	128.5064	108.9673	193.661	107.472	104.176	104.324	265.328	1.11	1.85	0.271	11.76
Sr_2VRuO_6	274.09	149.54	89.39	191.06	78.54	76.13	77.33	165.15	1.43	2.47	0.32	8.83

The high value of C11 compared to C12 and C44 indicates that this material exhibits greater resistance to unidirectional compression than to shear deformation.

The other mechanical properties are also calculated using the three approximations of Voigt [5], Reuss [6], and Hill [7]. Table IV-5 summarizes the results obtained for bulk modulus, the shear modulus, Young's modulus, anisotropic parameter, B/G ratio, Poison's ratio and Vickers hardness for $Ba_{2-x}Sr_xVRuO_6$ (x=0,1,2).

From these results, we derive the following observations:

- The anisotropic factor (A) for Ba_2VRuO_6, $BaSrVRuO_6$ and Sr_2VRuO_6 deviates from 1.0, suggesting that this compound exhibits elastic anisotropic.
- It is observed that the B/G value is greater than 1.75, indicating that the compounds are ductile. Furthermore, the B/G ratio is a measure of material hardness; higher hardness is often indicated by lower ratios. It follows that the $BaSrVRuO_6$ alloy is probably harder than Ba_2VRuO_6 and then Sr_2VRuO_6.
- The stiffness of the materials, indicated by Young's modulus (E), follows the order: $BaSrVRuO_6$ > Ba_2VRuO_6 > Sr_2VRuO_6, showing an increase from Sr_2VRuO_6 to $BaSrVRuO_6$.
- the Poisson's ratio falls within the range of 0.25 to 0.5, so the compounds exhibit greater stability under external degradation and reduced compressibility.
  The values we obtained for the Poisson's ratio are 0.28, 0.27 and 0.32, which indicates that our compounds exhibits an ionic character.

- In our study, the calculated values of G_{VRH}/B_{VRH} are 0.49, 0.54 and 0.40 for Ba_2VRuO_6, $BaSrVRuO_6$ and Sr_2VRuO_6 respectively suggesting that ionic bonding is more prevalent in these materials.
- Based on the calculated hardness values, Ba_2VRuO_6 and Sr_2VRuO_6, as examined in this study, can be classified as soft materials, while $BaSrVRuO_6$ is classified as a hard material.

Figure IV-3 represents the Young's modulus E, shear modulus G, and Poisson's ratio ν in 2 dimensions (2D) and 3 dimensions (3D) for our compounds. The 3D surface should exhibit a spherical shape for a perfectly isotropic compound. It is seen in Figure IV-3 that the 3D surface of G, E, and ν of all ompounds has an almost spherical shape. This result clearly indicates that Ba_2VRuO_6, $BaSrVRuO_6$ and Sr_2VRuO_6 are anisotropic compound.

Based on the Table IV-6, it can be observed that the Ba_2VRuO_6 compound exhibits greater variation compared to the Sr_2VRuO_6 compound, with the $BaSrVRuO_6$ compound showing the least variation.

Table IV-6 : The maximum and minimum values of Young's modulus (E, in GPa), linear compressibility (B, in TPa^{-1}), shear modulus (G, in GPa) and Poisson's ratio (ν) of that Ba_2VRuO_6, $BaSrVRuO_6$ and Sr_2VRuO_6 compounds.

Material		**Young's modulus**		**Shear modulus**		**Poisson's ratio**	
		E_{min}	E_{max}	G_{min}	G_{max}	ν_{min}	ν_{max}
Ba_2VRuO_6	Value	137.07	504.57	49.528	235.29	0.02399	0.69185
	Anisotropy	3.681		4.751		28.8394	
$BaSrVRuO_6$	Value	250.98	275.27	97.732	108.97	0.23325	0.30414
	Anisotropy	1.097		1.115		1.3039	
Sr_2VRuO_6	Value	168.52	231.99	62.275	89.39	0.18595	0.44414
	Anisotropy	1.377		1.435		2.3885	

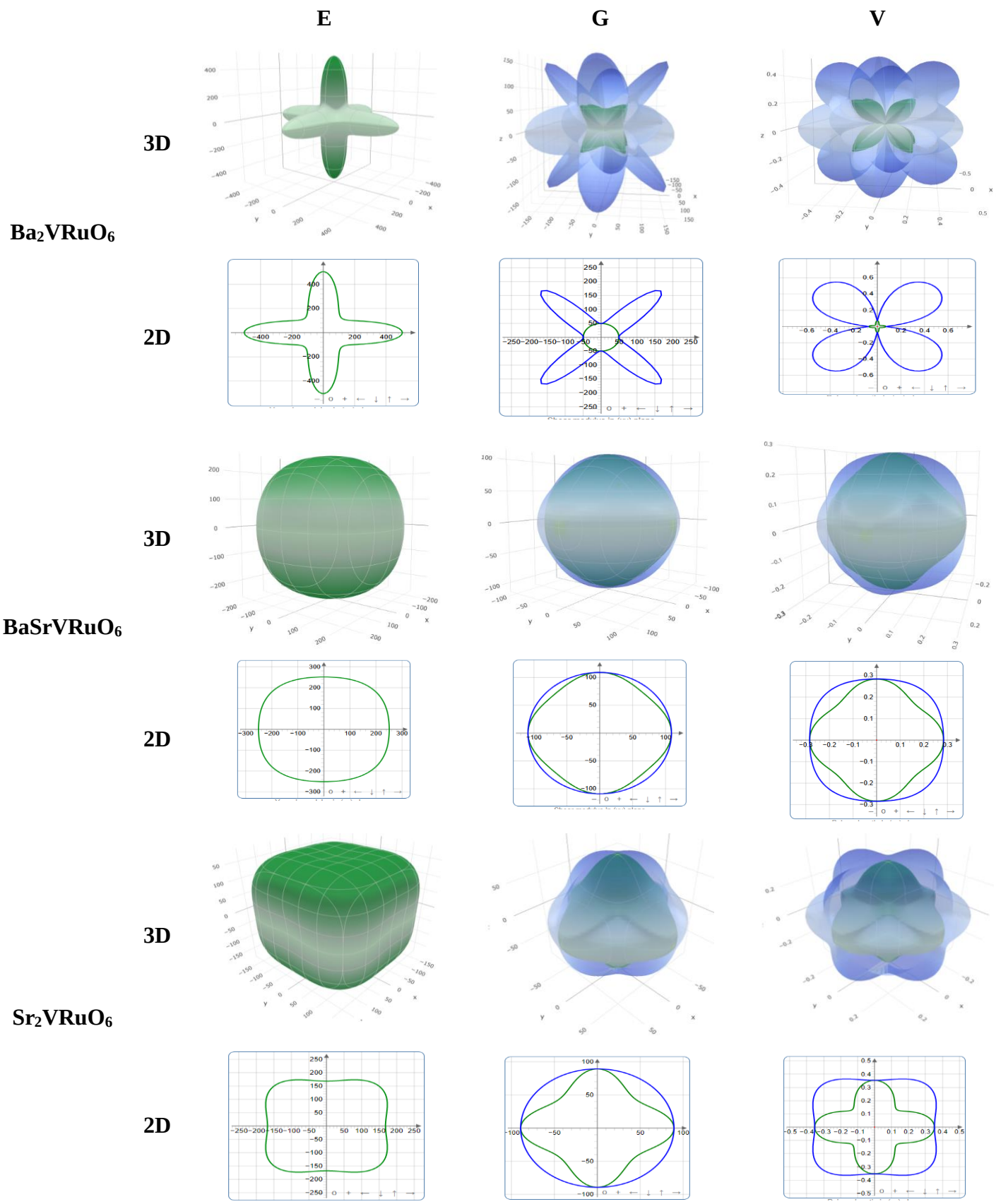

Figure IV-3: The Young's modulus E, shear modulus G and Poisson's ratio v in (2D) and (3D) for Ba_2VRuO_6, $BaSrVRuO_6$ and Sr_2VRuO_6 compounds.

IV-4-2-a Isotropic acoustic wave velocities and Debye temperature

The values of the Debye temperature (θD), melting temperature, and wave velocities of $Ba_{2-x}Sr_xVRuO_6$ (x=0,1,2) compounds are summarized in Table Table IV-7.

According to the results, it is observed that the Debye temperatures are high, indicating that these materials may exhibit significant thermal conductivities. The value of (θD) decreases as follows: $BaSrVRuO_6$> Ba_2VRuO_6 > Sr_2VRuO_6. Therefore, it can be predicted that $BaSrVRuO_6$ conducts heat more efficiently than Ba_2VRuO_6, and Ba_2VRuO_6 conducts heat better than Sr_2VRuO_6.

Table IV-7: Calculated longitudinal elastic wave velocity (vl), transverse (vt), average wave velocity (vm), melting and Debye temperature (Tm and θD) of $Ba_{2-x}Sr_xVRuO_6$.

Compound	v_l(m/s)	v_t(m/s)	v_m(m/s)	T_m(K)	θ_D(K)
Ba_2VRuO_6	6815.53	3730.92	4160.07	3568.9326	536.35
$BaSrVRuO_6$	7106.23	3978.93	4428.78	2467.6632	577.238
Sr_2VRuO_6	7025.66	3602.28	4034.9	2172.871	527.763

IV-4-3 Electronic Properties of $Ba_{2-x}Sr_xVRuO_6$

The electronic properties, including charge density, partial and total density of states, and band structure, were calculated as in the previous section using the Wien2k code.

IV-4-3-a Band structure

We calculated the band structures of perovskite $Ba_{2-x}Sr_xVRuO_6$ (x=0,1,2) along the high-symmetry axes in the first Brillouin zone using the GGA-WC and TB-mBJ approaches in the FM phase. The obtained results are illustrated in the figures (IV-4, IV-5, IV-6), we can observe that :

- For Ba_2VRuO_6

- We observe a metallic character in the spin (up + down) channel when using the GGA-WC approximation.
- when using the TB-mBJ approximation we see a metallic character for the spin dn channel and a semiconductor character for spin up channel, the valence band maximum is positioned at the x point with an energy of −1.11 eV, while the

conduction band minimum is located at the Γ point with an energy of 0.99 eV. This results in a indirect band gap of 2.1 eV, its value is close to other theoretical calculations (2.02ev) [8].

- For $BaSrVRuO_6$

- Under the GGA-WC approximation, we observe a metallic character in the spin dn , and for spin up we see a semiconductor character with indirect band gap equal to 0.65 eV, is situated between the valence band's maximum at x (0.0 eV) and the conduction band's lowest at Γ (0.65 eV).
- The spin-down channel behaves metallically under the TB-mBJ approximation, but the spin-up channel has a semiconductor nature with an indirect band gap of 1.53 eV. The conduction band's minimal is found at Γ (0.73 eV), whereas the valence band's maximum is found at X (0.80 eV).

- For Sr_2VRuO_6

- It is observed that the spin dn channel exhibits a metallic nature with both approximation GGA-WC and TB-mBJ.
- With GGA-WC approximation the indirect band gap in the spin-up configuration is situated between the valence band's maximum at X (-0.08 eV) and the conduction band's lowest at L (0.88 eV), creating an energy differential of 0.96 eV, and with TB-mBJ approximation the conduction band minimum is at the Γ (1.37 eV), while the valence band maximum is at the R (−0.97 eV), the indirect band gap as a result is 2.34 eV.

We observe that the TB-mBJ has evaluated the gaps more accurately than GGA. Consequently, $Ba_{2-x}Sr_xVRuO_6$ (x=0,1,2) compounds can be classified as a half metallic perovskite.

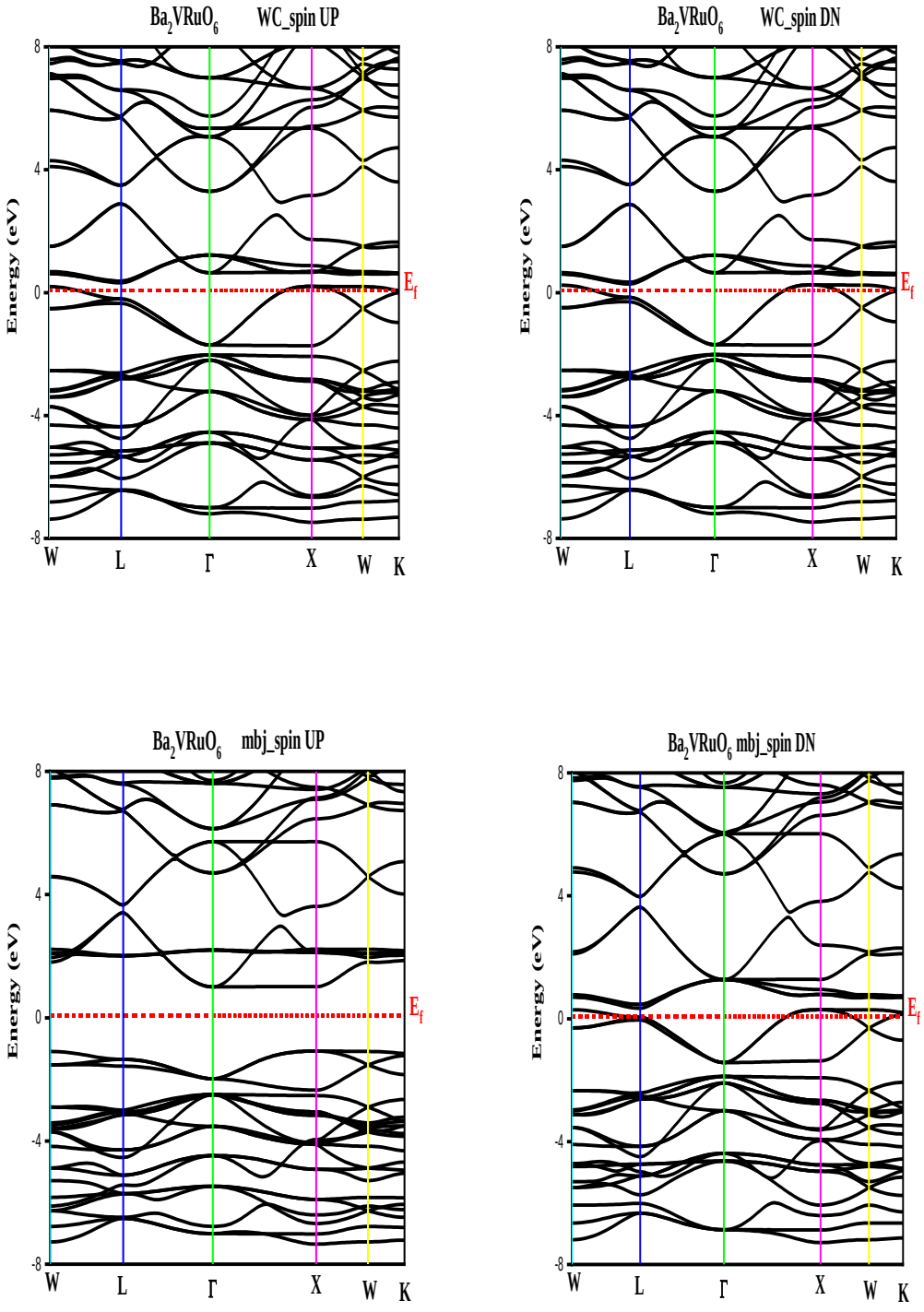

Figure IV-4 :. The band structure of Ba2VRuO6 along lines of high symmetry of the Brillouin zone with TB-mBJ approximations and WC-GGA.

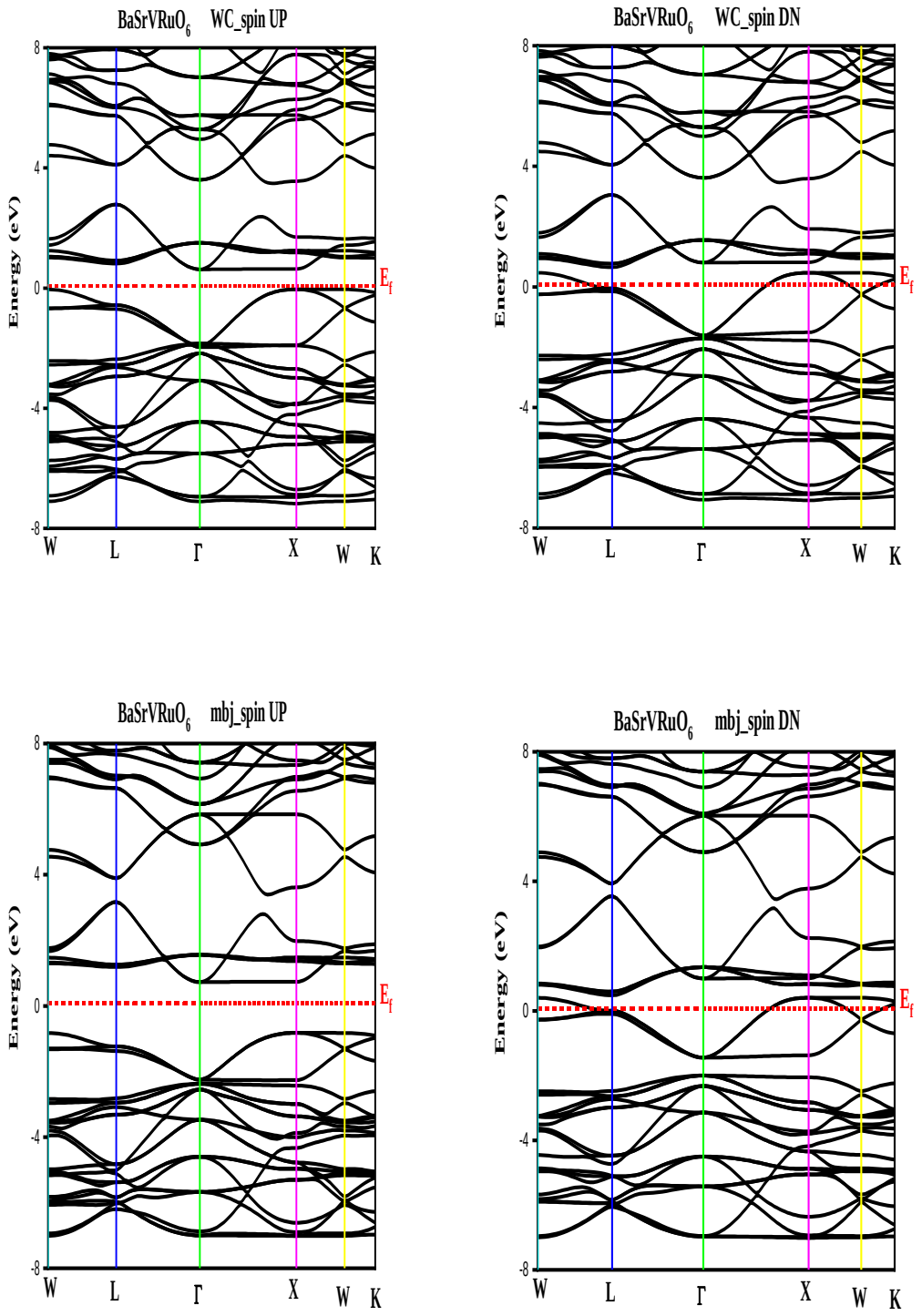

Figure IV-5 : The band structure of BaSrVRuO6 along lines of high symmetry of the Brillouin zone with TB-mBJ approximations and WC-GGA.

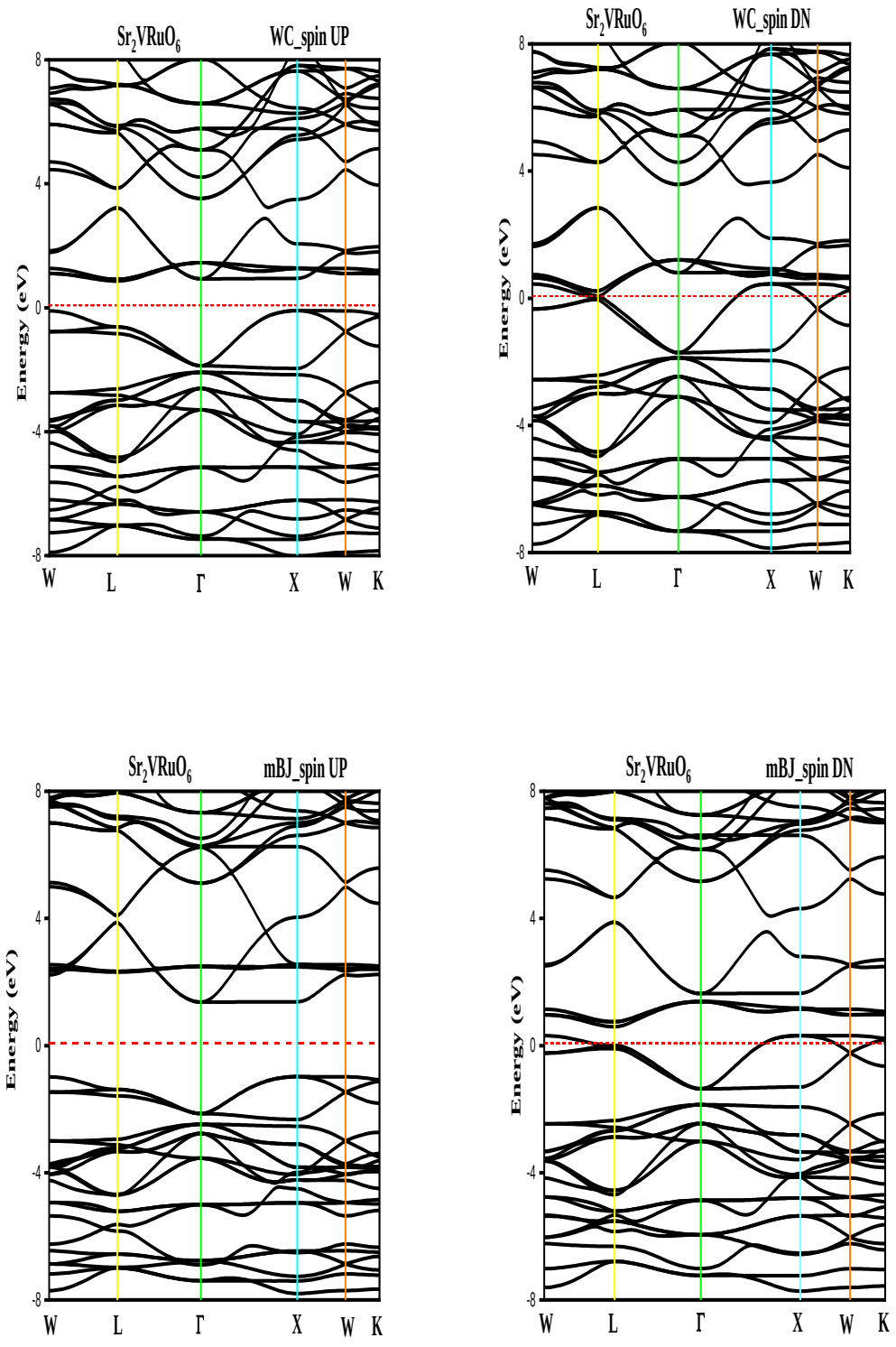

Figure IV-6 : The band structure of Sr_2VRuO_6 along lines of high symmetry of the Brillouin zone with TB-mBJ approximations and WC-GGA.

IV-4-3-b Density of States (DOS)

Figures (IV-7, IV-8 and IV-9) illustrate the total and partial density of states of perovskite oxide $Ba_{2-x}Sr_xVRuO_6$ (x=0,1,2) obtained using TB-mBJ.

We observe that the dominant contribution to the density of states (DOS) arises from the d orbitals of the Ba, Sr, V, and Ru atoms, with a minor contribution from the p orbitals of the oxygen atoms.

From Figures We can observe that DOS is similar in the three compounds. Based on this, we obtained the following table, in which we have grouped the state contributions.

Table IV-8: Localization of energy bands and state contributions for the three compounds Ba_2VRuO_6, $BaSrVRuO_6$ and Sr_2VRuO_6 using TB_mBJ approximation.

	UP			**DN**		
Interval	[-8 ; -2.5]	[-2.5 ; 1]	[1 ; 8]	[-8 ; -2.5]	[-2.5 ; 1]	[1 ; 8]
significant contribution	d_ Ru p_O	d_Ru	d_Ba d_Sr d_V	d_Ba d_Sr	d_V d_Ru	p_O
minor contribution	p_Ba p_Sr	p_O	d_Ru p_O		p_O	p_Ba p_Sr d_V d_Ru

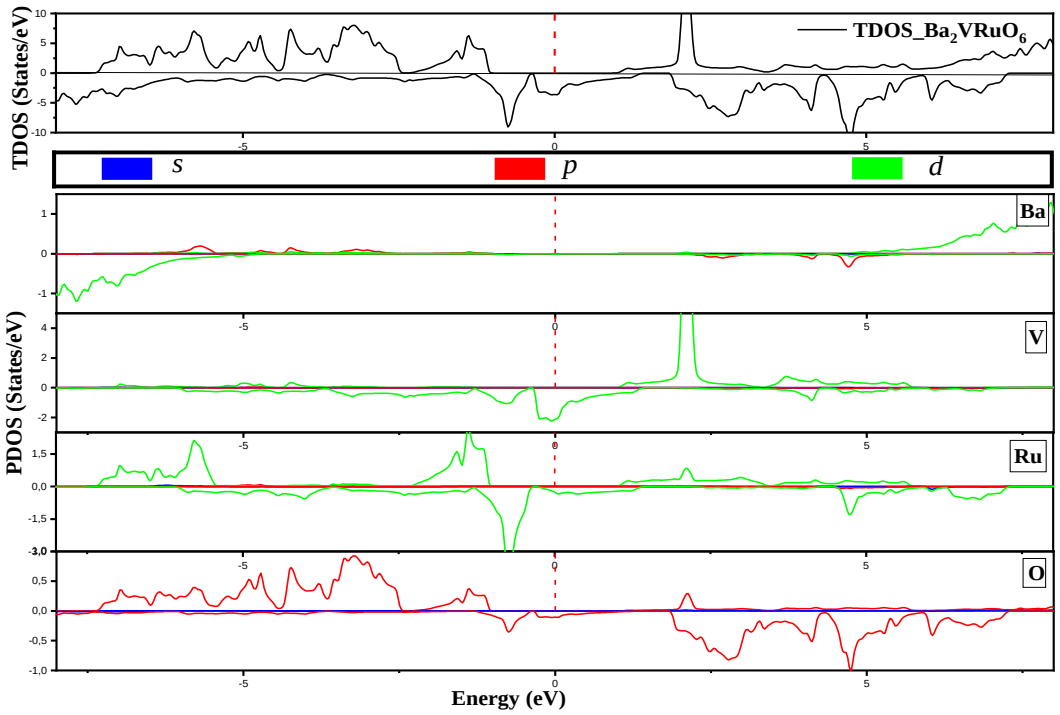

Figure IV-7: Total and Partiel density of states for Ba_2VRuO_6 using the mBJ–GGA approximations

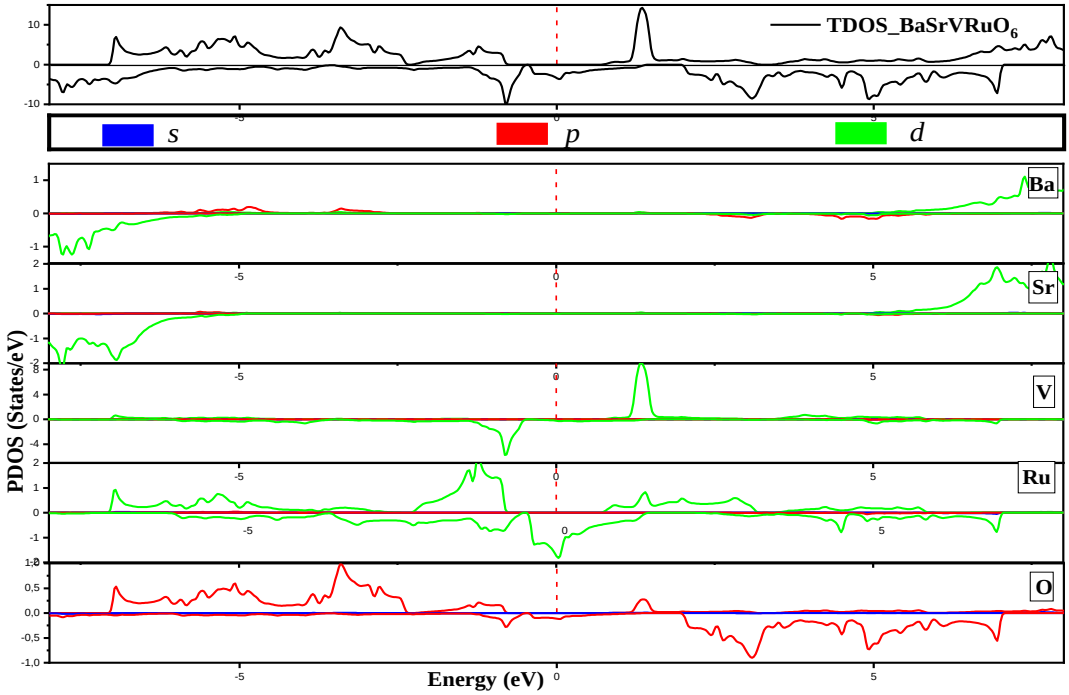

Figure IV-8: Total and Partiel density of states for $BaSrVRuO_6$ using the mBJ–GGA approximations

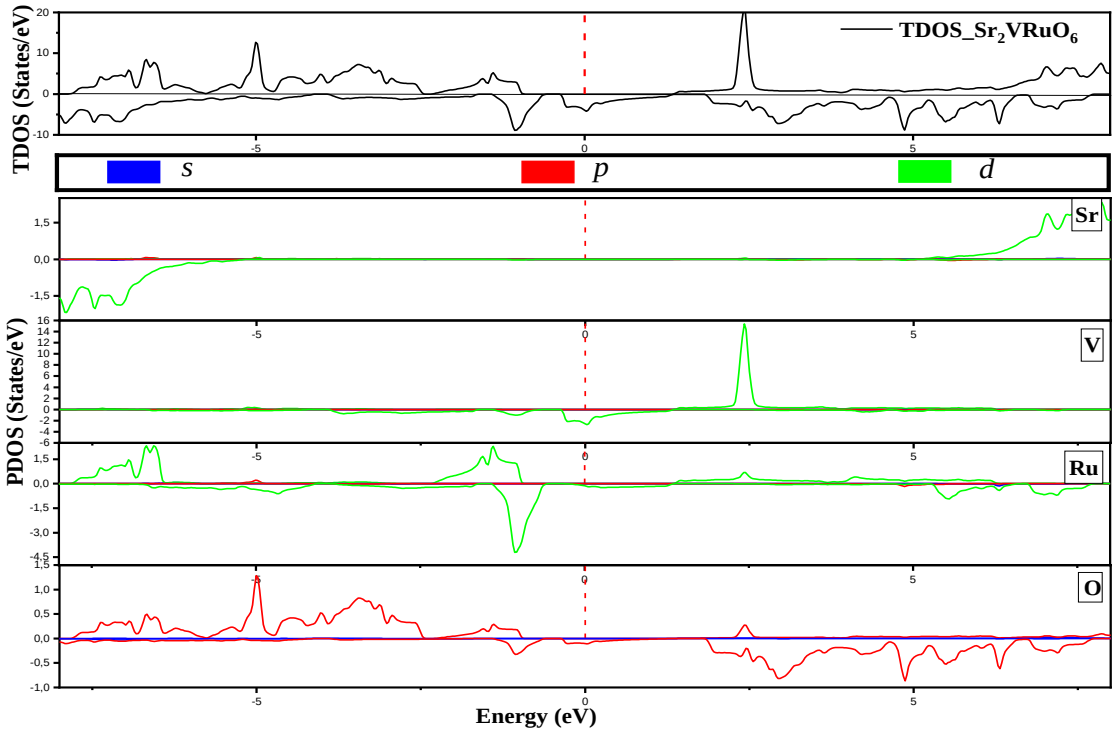

Figure IV-9: Total and Partiel density of states for Sr_2VRuO_6 using the mBJ–GGA approximations

IV-4-3-c Charge density

We calculated the charge density distribution of the ferromagnetic compounds $Ba_{2-x}Sr_xVRuO_6$ (x=0,1,2) (Figure IV-10) using the TB-mBJ approximation, in order to visualize the nature of the chemical bonds connecting the atoms.

Figure IV-10 shows that the Sr-O and Ba-O bond is ionic in nature because there are no electrons in common between these atoms. V-O and Ru-O bond is a covalent character as it is overlapping electron distributions between them.

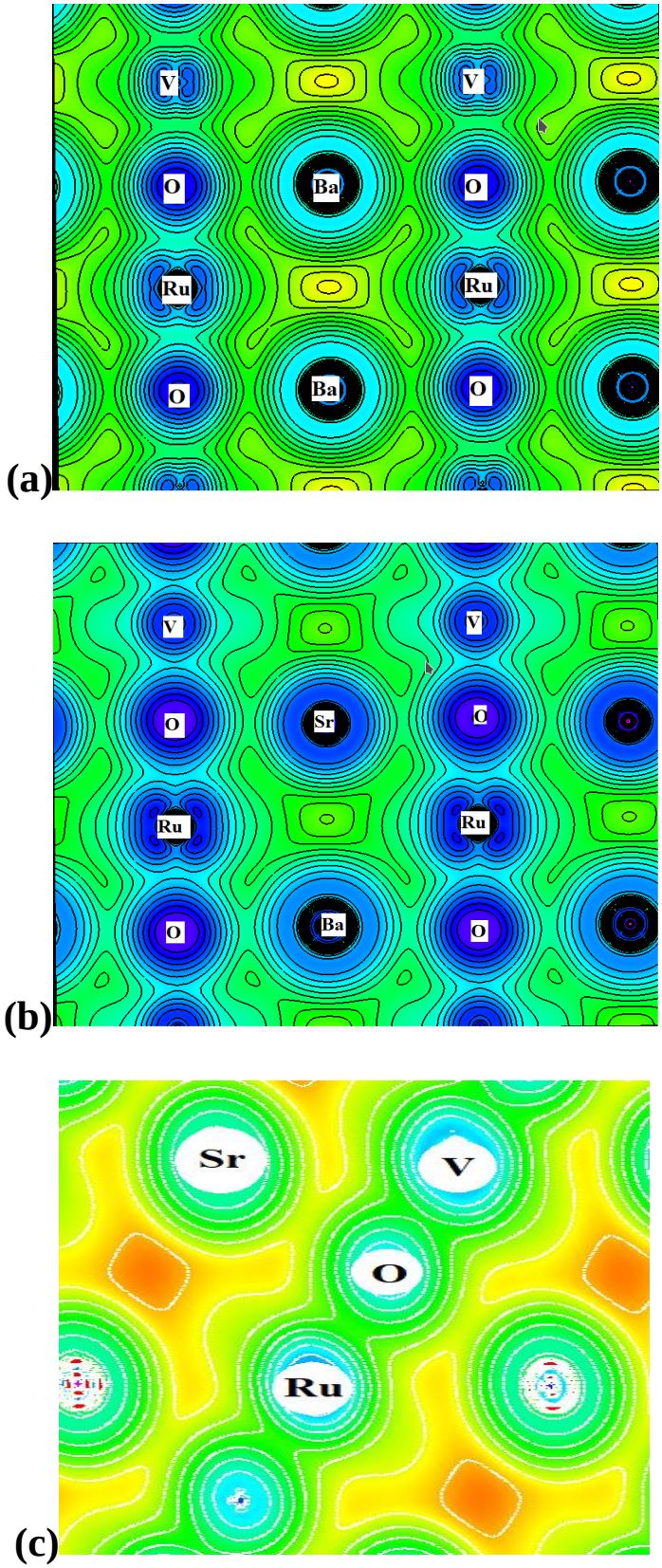

Figure IV-10: The electronic charge density of Ba_2VRuO_6 (a), $BaSrVRuO_6$ (b) and Sr_2VRuO_6 (c) compounds obtained using the TB-mBJ approach.

III -4-4 Magnetic properties

Table IV-9 summarizes our results for $Ba_{2-x}Sr_xVRuO_6$ (x=0,1,2) using TB-mBJ approximation about the total spin magnetic moments MT(μB), partial spin magnetic moment, and interstitial magnetic moments (in μB). It also includes the results of the earlier ab initio calculations. Further supporting the previously noted DOSs is the observation that for Sr2VRuO6, the Ru atom contributes more to the total magnetic moment. The negative values of the magnetic moment of the Sr, Ba and V atoms in $Ba_{2-x}Sr_xVRuO_6$ (x=0,1,2) compounds reduce the total magnetic moment. The compounds stabilize in the ferromagnetic phase. The integer value of the total magnetic moments per unit cell is 1μB which affirms the semi-metallic character of the materials and their exploitability in the field of spintronics.

Table IV-9: Calculated total spin magnetic moments $M_T(\mu_B)$, partial spin magnetic moment and interstitial magnetic moments (in μB) for Ba_2VRuO_6 , $BaSrVRuO_6$ and Sr_2VRuO_6. with TB-mBJ approximation.

Compound		approx	M_{tot} (μB)	M_{Ba} (μB)	M_{Sr} (μB)	M_V (μB)	M_{Ru} (μB)	M_O (μB)	M_{int} (μB)
$BaSrVRuO_6$	This work	TB-mBJ	0.99996	-0.00206	-0.00410	-0.38640	0.91372	0.08312	-0.01995
	Other work		-	-	-	-	-	-	-
Ba_2VRuO_6	This work	TB-mBJ	1.00003	-0.00038	-	-1.21802	1.45024	0.14138	-0.07972
	Other work [9]		1.00	0.039	-	-1.832	1.917	0.876	-
Sr_2VRuO_6	This work	TB-mBJ	1.82	-	-0.006	-0.058	1.178	0.114	0.035
	Other work[1]		1.000 0.985	-	-	-1.122 -1.118	1.350 1.340	0.105	-

III-4-5 Optical properties

The calculations we performed to determine the optical properties of the Ba_2VRuO_6, $BaSrVRuO_6$ and Sr_2VRuO_6 compounds in the cubic phase are based on density functional theory (DFT), using the full-potential linearized augmented plane wave (FP-LAPW) method.

The imaginary part $\varepsilon_2(\omega)$ is represented in Figure IV-11, with the dielectric function energy threshold at 2. 1 eV, 1.53 eV and 2.34 eV for Ba_2VRuO_6, $BaSrVRuO_6$ and Sr_2VRuO_6, respectively. This value exactly matches the band structure gap calculated using TB-mBJ. According to this figure, strong absorption peaks are observed in the energy range of 3–10.5 eV. These peaks correspond to specific transitions between different orbitals. It can be identified that the peaks around 3.6–5.36 eV mainly result from transitions from valence bands (d-Ru, p-O) to conduction bands (d-Ru, d-V).

The real part of the dielectric function for our compounds starts from zero frequency and increases to its maximum value at 2.7 eV, 2.3ev and 1.27 ev for Ba_2VRuO_6, $BaSrVRuO_6$ and Sr_2VRuO_6, respectively, then decreases with the increase in photon energy. It becomes negative in the energy ranges (13.17 to 14.04 eV) and (19.36 to 27 eV) for Ba_2VRuO_6, (12.74 to 14.08 eV), (19.87 to21.04 eV) and (23.64 to 27eV) for $BaSrVRuO_6$, and (24.04 to 27 eV) for Sr_2VRuO_6. Consequently, our material exhibits metallic behavior and can be used for radiation protection purposes within this energy range.

The absorption coefficient of $Ba_{2-x}Sr_xVRuO_6$ is presented in Figure V-12. The first critical point appears at 2.7 eV, 2.3ev and 1.27 ev for Ba_2VRuO_6 , $BaSrVRuO_6$ and Sr_2VRuO_6, respectively, which is associated with the bandgap (Eg). The maximum absorption of Ba_2VRuO_6 occurs at a value of 461.38×10^4 cm^{-1} at 24.83 eV. For $BaSrVRuO_6$,the absorption coefficient reaches its maximum values at 353.54×10^4 cm^{-1} at 24.74 eV and For Sr_2VRuO_6,the absorption coefficient reaches its maximum values at $363.36.54\times 10^4$ cm^{-1} at 19.95 eV.

These compounds exhibit maximum absorbance in the ultraviolet region and, consequently, serve as highly effective devices for use as sensors.

It was also observed that our material is completely transparent in the range [0 to 2.7 eV], [0 to 2.3 eV] and [0 to 1.27 eV] for Ba_2VRuO_6 , $BaSrVRuO_6$ and Sr_2VRuO_6, respectively, indicating that it cannot absorb light below the energy band gap values. However, beyond this threshold, its absorption increases rapidly.

In Figure V-12, the values of the static refractive index n(0) can be observed. The static refractive index reaches a value of 2.12 eV for Ba_2VRuO_6,3.17 eV for $BaSrVRuO_6$ and for Sr_2VRuO_6 the values obtained are 2.31 eV

From the real part of the dielectric function, the static refractive index can also be determined using the appropriate relation.

The energy loss function L(ω) is shown in Figure V-12. In the energy range of 10–15 eV, the energy loss is at its maximum, with peaks at 14.43 eV, 14.25 eV and 13.81 eV for Ba_2VRuO_6, $BaSrVRuO_6$ and Sr_2VRuO_6, respectively. These peaks in the energy loss spectrum correspond to plasma resonance.

In the same figure, we have plotted the reflectivity. The reflectivity value at zero frequency is 33.45%, 33.33% and 17.27% for for Ba_2VRuO_6, $BaSrVRuO_6$ and Sr_2VRuO_6, respectively. The highest reflectivity is recorded at 45.09% at an energy of eV for Ba_2VRuO_6, at 60.96% at an energy of 20.15 eV for $BaSrVRuO_6$ and 71.63% at an energy of 26.35 eV for Sr_2VRuO_6.

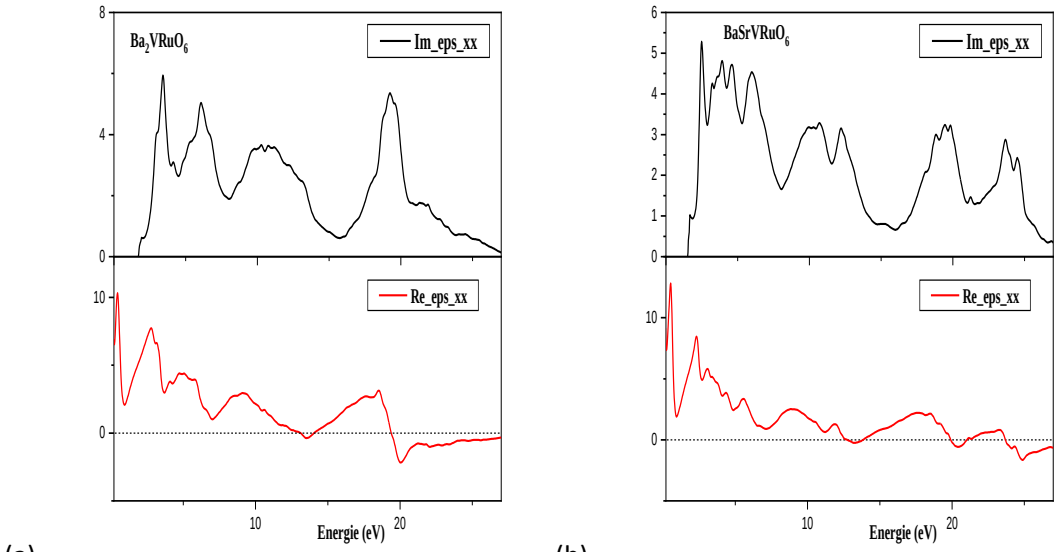

(a) (b)

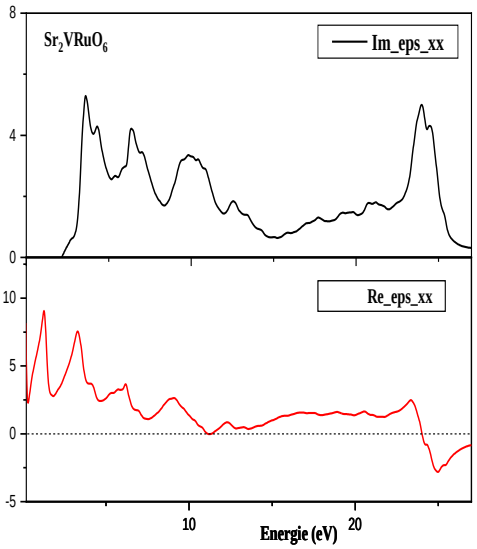

(c)

Figures IV-11: : the real part $\varepsilon_1(\omega)$ and the imaginary part $\varepsilon_2(\omega)$ of dielectric function for Ba_2VRuO_6 (a), $BaSrVRuO_6$ (b) and Sr_2VRuO_6 (c) compounds obtained using the mBJ approach.

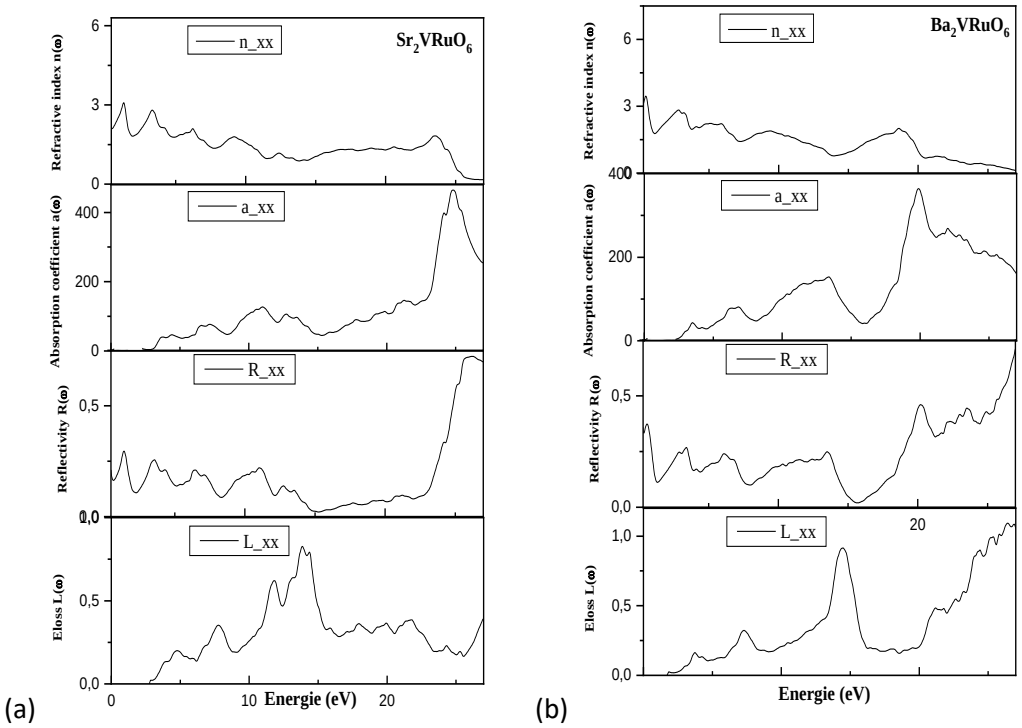

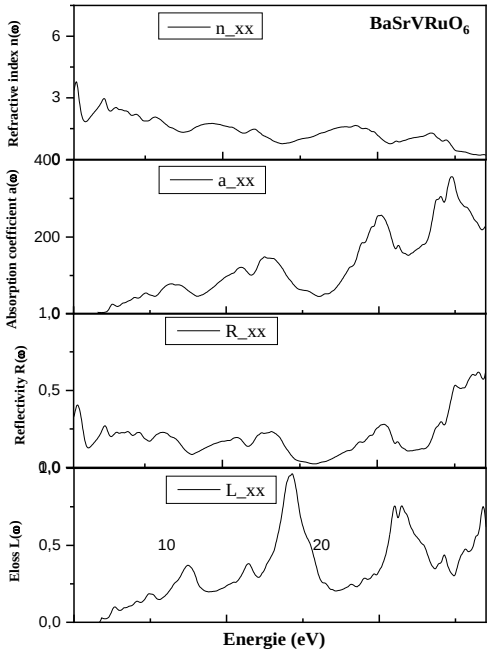

Figures IV-12: Optical properties calculated as a function of the incident photon energy (eV): refractive index n, absorption coefficient α, reflectivity R and energy loss L, of for Ba_2VRuO_6 (a), $_6$ Sr_2VRuO_6 (b) and BaSrVRuO (c) compounds obtained using the mBJ approach.

III-4 Conclusion

This chapter presented an ab-initio study of the structural, electronic, magnetic, optical, and mechanical properties of $Ba_{2-x}Sr_xVRuO_6$ (x=0,1,2) in the cubic phase.

Based on this study, the following conclusions can be drawn:

The computational results indicate that the most stable phase is ferromagnetic (FM). Electronically, $Ba_{2-x}Sr_xVRuO_6$ (x=0,1,2) exhibits an indirect band gap of 2. 1 eV, 1.53 eV and 2.34 eV for Ba_2VRuO_6, $BaSrVRuO_6$ and Sr_2VRuO_6, respectively, as calculated using the TB-mBJ method. These compounds are predicted to be semiconductor materials with a mixed ionic-covalent nature of chemical bonding.

The calculated elastic constants indicate that this material is mechanically stable. The computed B/G ratioa for the three compounds is greater than the critical value (1.75), suggesting that their mechanical properties correspond to those of a ductile material.

The calculated elastic anisotropy factors (A) indicate that these three materials exhibit slight elastic anisotropy.

reference

[1] A. Halder, G. Aishwaryo, and S. D. Tanusri. Physical Review Materials 3.8 (2019): 084418.

[2] M. M. Hasab-Elkhalig. Indian Journal of Pure & Applied Physics (IJPAP) 58.2 (2020): 120-126.

[3] W. Rahim, and al. Chemistry of Materials 32.22 (2020): 9573-9583.

[4] N. N. Kiselyova, and al. Inorganic Materials: Applied Research 13.2 (2022): 277-293.

[5] W. Voigt. Leipzig und Berlin 962 (1928): 252.

[6] A. J. Z. A. M. M. Reuss. Math. Phys 9 (1929): 49-58.

[7] R. Hill. Proceedings of the Physical Society. Section A 65.5 (1952): 349.

[8] H. E. M. Saad, and S. S. Althoyaib. Materials Chemistry and Physics 190 (2017): 230-240.

[9] H. E. M. Saad, and S. S. Althoyaib. Materials Chemistry and Physics 190 (2017): 230-240.

General conclusion

General conclusion

In this thesis, we present an ab-initio study of the structural, electronic, magnetic, and optical properties of the oxides $SrVO_3$, $SrRuO_3$, $BaVO_3$, $BaRuO_3$, Ba_2VRuO_6, $BaSrVRuO_6$ and Sr_2VRuO_6 in the cubic crystalline phase, based on density functional theory (DFT) and the full-potential linearized augmented plane wave (FP-LAPW) method, as implemented in the Wien2k code. The various studied properties were calculated using two approximations: the GGA-WC approximation and the Tran and Blaha (TB-mBJ) approach.

Based on this study, the following conclusions can be drawn:

- Firstly, according to the structural study, our calculated results for the lattice parameters, bulk modulus, and its derivative for the perovskite oxides ABO_3 (A = Sr, Ba and B = V, Ru) and $Ba_{2-x}Sr_xVRuO_6$ (x=0,1,2) are in very good agreement with experimental data.
- We have examined the magnetic stability of the two types of perovskite. By calculating the total energy, we found that the most stable state is the ferromagnetic (FM) state.
- The magnetic properties of these perovskites indicate that magnetism originates from the transition metals Ru and V.

Subsequently, we determined the electronic properties, including the band structure, the density of states (DOS), and the charge densities.

- Our electronic band structure calculations for the seven compounds reveal that compounds exhibit half-metallic (HM) behavior at equilibrium, with spin polarization reaching 100% at the Fermi level.
- The charge density calculated using TB-mBJ approach revealed the presence of two dominant types of chemical bonds in the ABO_3 and $Ba_{2-x}Sr_xVRuO_6$ across both crystalline phases: the ionic Sr-O and Ba-O bonds and the covalent Ru-O and V-O bonds.
- The optical properties of these compounds, such as the real and imaginary parts of the dielectric functions, refractive indices, reflectivity, and absorption coefficients, are also calculated. The high absorption of these compounds in the

ultraviolet energy range enables these perovskites to be used in optical and optoelectronic devices operating within this spectral range.

- The elastic constants and other related quantities, such as Young's modulus, shear modulus, Poisson's ratio, anisotropy factor, sound velocities, and Debye temperature, have been calculated and estimated in the present work.

  The study of elastic properties allowed us to conclude that all compounds exhibit slight anisotropy. Furthermore, the values of the single-crystal elastic constants satisfy Born's mechanical stability conditions, thereby indicating the mechanical stability of these compounds.
- The bulk modulus calculated from the single-crystal elastic constants C_{ij} is in perfect agreement with the one estimated through the Equation of State fitting. This result demonstrates the reliability of our calculations.
- By calculating the B/G ratios and based on Pugh's criterion, we have shown that these materials are classified as ductile.
- The obtained values of Poisson's ratio indicate the presence of ionic bonding, which is consistent with the results derived from the electronic structure analysis of these systems.
- The three-dimensional representation of Young's modulus exhibits strong anisotropy. Based on the Young's modulus values, the studied compounds demonstrate significant rigidity